COHERENT SCATTER COMPUTED TOMOGRAPHY (CSCT) – A MONTE CARLO SIMULATION STUDY

By

KENNETH GERALD LEWIS II

Dissertation

Submitted to the Faculty of the

Graduate School of Vanderbilt University

in partial fulfillment of the requirements

for the degree of

DOCTOR OF PHILOSOPHY

in

Physics

August, 2013

Nashville, Tennessee

Approved:

Professor Ronald R. Price

Professor Edwin F. Donnelly

Professor David R. Pickens

Professor M. Todd E. Peterson

Professor M. Shane Hutson

Professor David J. Ernst

DEDICATION

To my mother, for demonstrating to me that hard work pays off.

To my mentors, for their guidance and advice.

To my friends and family, for encouraging me every step of the way.

What you get by achieving your goals is not as important
as what you become by achieving your goals.
–Henry David Thoreau

ACKNOWLEDGEMENTS

There are numerous people to whom I am indebted for assisting me in my academic and personal endeavors over the past few years. So, I would like to take this opportunity to thank and recognize several of the most influential individuals who offered me advice, inspiration, and encouragement. This is by no means a comprehensive list, but is a merely a sampling of the many individuals who have positively influenced me.

Firstly, I would like to thank Dr. Ronald Price, my advisor, along with the Vanderbilt University Medical Center Department of Radiology and Radiological Sciences, for providing me with the opportunity and environment in which to grow intellectually. Dr. Price was unwavering in his support and guidance and always very patient. Thank you.

I would also like to recognize and thank my committee members: Drs. Edwin Donnelly and David Pickens, for their weekly advice and software / laboratory hardware assistance; Dr. Peterson for offering a simple programing suggestion that significantly reduced the time to perform a majority of the simulations in this work; Dr. Shane Hutson for being an excellent instructor and correcting my statistical errors; and Dr. David Ernst for graciously participating on my committee.

Dr. Charles Coffey, I am forever grateful that you decided to offer me an opportunity to interview for the Medical Physics program even though the application period had closed. You opened the door to a wealth of other opportunities for me.

David Burkett, I am truly appreciative of the training and employment opportunity you furnished me. Without your efforts, I would not have achieved board certification as a Diagnostic Medical Physicist while as a graduate student.

Dr. Matthew Deeley, I am fortunate to have such a close friend. The countless discussions we had about continuing our education and the mutual moral support we both offered each other was indispensible. Also, thanks to Christina for all the meals.

Diana Carver and Arden, I love you both dearly and appreciate you opening hearts and sharing your life with me. Thank you for always being a positive and uplifting influence. I look forward to our future together.

Dr. Ross Schmidtlein, you were a role model when I was an undergraduate: you inspired me to become a strong runner – mainly because I didnt want someone older outrunning me. Thanks for the graduate school and career advice.

Dr. Ken Neirmann, thanks for the many stress relieving runs through Percy and Edwin Warner Parks. I have never seen anyone run with fewer clothes on in the wintertime than you.

Thank you to following for their encouragement and support: Jo Ann Fields, Dr. Mary Ann Emmons, Judy Bourgoin, Sheila Warf, Don Pickert, Dr. Jim Patton, Dr. Bill Riddle, Dr. Michael Stabin, Susan Kost, Jeff Hammonds, Chris Muraski, Dr. Jessica Clark, LT Nick Nickles, LCDR Joe Dablow, CDR Thomas Fouts, Mr. Ronald Overman, Andy Miller, Dr. Gary Smith, Dr. Ronald Walker, the Smallings, the Hardings, and many, many others.

And lastly, thank you to my parents, especially my mother, for being an influential and positive role model in my life.

TABLE OF CONTENTS

Page

DEDICATION iii

ACKNOWLEDGEMENTS iv

LIST OF TABLES ix

LIST OF FIGURES xii

LIST OF ABBREVIATIONS xvi

Chapter

I. INTRODUCTION 1

Coherent Scatter Computed Tomography (CSCT) 1
Coherent Scatter Modeling 3
Coherent scatter theory in CSCT 5

II. VERIFICATION OF COHERENT SCATTER MODELING IN EGS5 10

Introduction 10
Method: Pencil-beam geometry 11
Laboratory setup 11
Simulation setup 13
Measurement processing 15
Laboratory Data 15
Simulated Data 16
Distribution Comparison 18
Results & Discussion 20
Lab/sim comparison: poly-energetic beam 20
Fat 20
Muscle 22
Water 24
Conclusion 26

III. EGS5 CSCT SIMULATIONS: PART I 27

Introduction 27
Method 28
Heterogeneous Phantom #1 30

Segmented Fan Beam Geometry . . . 32
Processing Details . . . 35
Image Reconstruction . . . 35
Results . . . 36
Homogeneous phantoms: Scatter Profiles . . . 36
Heterogeneous phantom: CSCT Image Contrast . . . 37
Discussion . . . 39
Conclusion . . . 43

IV. EGS5 CSCT SIMULATIONS: PART II . . . 44

Introduction . . . 44
Method . . . 45
Heterogeneous Phantom #2 . . . 46
Image Metrics: Contast, CNR, and SNR . . . 46
Monoenergetic Beams . . . 47
Polyenergetic Beams . . . 48
W 80, W 120, W 140 kVp . . . 48
Mo 32 kVp . . . 51
$CTDI_{100}$ . . . 51
Dose . . . 52
Results . . . 53
30, 50, 70, 90 keV; 65 Views; x1, x10 . . . 53
Contrast . . . 54
CNR . . . 59
SNR . . . 62
45, 60, 75, 85 keV; 128 Views; x1 . . . 62
Contrast . . . 65
CNR . . . 69
SNR . . . 69
W 80, W 120, W 140 kVp; 128 Views; x1, x10, x100 . . . 70
Contrast . . . 70
CNR . . . 70
SNR . . . 75
Mo 32 kVp; 128 Views; x1, x10 . . . 75
Contrast . . . 75
CNR . . . 79
SNR . . . 81
Dose . . . 81
All Monoenergetic Beams . . . 82
W 80, W 120, W 140 kVp . . . 85
Mo 32 kVp . . . 86
$CTDI_{100}$ . . . 88
Tungsten Polyenergetic Beams . . . 88
Discussion . . . 90
CTDI . . . 91

Conclusion 93

V. SINGLE SHOT COHERENT SCATTER COMPUTED TOMOGRAPHY (SSCSCT) 94

Introduction 94
Method 94
Results 96
Discussion 102
Conclusion 103

VI. SUMMARY OF RESULTS 105

Appendicies

A. HISTORICAL CONTRIBUTIONS TO CSCT RESEARCH 107

B. PHYSICAL PRINCIPLES OF COHERENT SCATTER 112

Thompson Scatter - classical scattering from a single free electron 112
Rayleigh Scatter and Form Factors - coherent scatter from multiple electrons 114
Compton Scatter - incoherent scatter 116

C. $CTDI_{100}$ 118

REFERENCES 121

LIST OF TABLES

Table Page

II.1. Statistical comparison between laboratory and simulated angular scatter distributions. 20

III.1. EGS5 material composition. Tissue mixture compositions match ICRU 46 Appendix A table A.1 elemental composition for adult tissues. Beef Kidney material is used in Chapter IV. 31

III.2. Muscle-to-fat contrast 41

IV.1. Polyenergetic spectra characteristics for the simulations. 50

IV.2. Contrast between insert materials and water background for phantom #2 - 30, 50,70, 90 keV, 65 view angles. θ = scatter angle. $\times 10$ = ten times more photons than the $\times 1$ data set. 58

IV.3. CNR of insert materials referenced to water background for phantom #2 - 30, 50,70, 90 keV, 65 view angles. θ = scatter angle. $\times 10$ = ten times more photons than the $\times 1$ data set. 60

IV.4. SNR for phantom #2 - 30, 50,70, 90 keV, 65 view angles. θ = scatter angle. $\times 10$ = ten times more photons than $\times 1$ data set. 64

IV.5. Contrast between insert materials and water background for phantom #2 - 45, 60,75, 85 keV, 128 view angles, 2.6×10^{11} photons total. θ = scatter angle. 67

IV.6. CNR of insert materials referenced to water background for phantom #2 - 45, 60,75, 85 keV, 128 view angles, 2.6×10^{11} photons total. θ = scatter angle. 67

IV.7. SNR for phantom #2 - 45, 60,75, 85 keV, 128 view angles, 2.6×10^{11} photons total. θ = scatter angle. 68

IV.8. Contrast between insert materials and water background for phantom #2 - tungsten spectra: 80, 120, 140 kVp; 128 view angles. θ = scatter angle. $\times 10$ = ten times more photons than the $\times 1$ data set; $\times 100$ = 100 times more photons than the $\times 1$ data set. 74

IV.9. CNR of insert materials referenced to water background for phantom #2 - tungsten spectra: 80, 120, 140 kVp; 128 view angles. θ = scatter angle. $\times 10$ = ten times more photons than the $\times 1$ data set; $\times 100$ = 100 times more photons than the $\times 1$ data set. 76

IV.10. SNR for phantom #2 - tungsten spectra: 80, 120, 140 kVp; 128 view angles. θ = scatter angle. $\times 10$ = ten times more photons than the $\times 1$ data set; $\times 100$ = 100 times more photons than the $\times 1$ data set. . 77

IV.11. Contrast between insert materials and water background for phantom #2 - Mo 32 kVp, 128 view angles. θ = scatter angle. $\times 10$ = ten times more photons than the $\times 1$ data set. 79

IV.12. CNR of insert materials referenced to water background for phantom #2 - Mo 32 kVp, 128 view angles. θ = scatter angle. $\times 10$ = ten times more photons than the $\times 1$ data set. 81

IV.13. SNR for phantom #2 - 32 kVp, 128 view angles. θ = scatter angle. $\times 10$ = ten times more photons than the $\times 1$ data set. 82

IV.14. Dose to phantom #2 segments; 65 view angles; 1.3×10^{11} source photons reaching the phantom. These simulation measurements are from the 30, 50 70, 90 keV, $\times 10$ flux data set. 83

IV.15. Dose to phantom #2 segments; 128 view angles; 2.6×10^{11} source photons reaching the phantom. 83

IV.16. Slice thickness 3.4 mm; estimated dose per 1×10^{10} photons to phantom #2 material regions. Data is plotted in figure IV.16. 83

IV.17. Tungsten (W) spectra: dose to phantom #2 segments; 128 view angles; $\times 100$ source photon flux. 85

IV.18. Molybdenum (Mo) spectra: dose to phantom #2 segments; 128 view angles; $\times 1$ and $\times 10$ source photon flux. [1]The simulated Mo 32 kVp beam had an inherent filtration of 0.5 mm of Be and no additional filtration. The results in table IV.18 indicated a high energy deposition at the surface of the phantom due to low photon attenuation, as evident in figure IV.18. 87

IV.19. Philips Brilliance 16: $CTDI_{100}$ to 10 cm diameter acrylic phantom for 7.5 mm slice thickness. 89

IV.20. Polyenergetic simulation: $CTDI_{100}$ to 10 cm diameter acrylic phantom and the equivalent mAs technique interpolated from the measurements in table IV.19. 89

IV.21. Composite image metrics of resultant image in figure IV.19 compared with 80 kVp ×100 simulation metrics in table IV.8, IV.9, IV.10. . . . 91

V.1. SSCSCT Contrast for phantom #2 - tungsten spectra: 80, 120, 140 kVp; 128 view angles; ×100 data set. θ = scatter angle. The 0° image is the FBP attenuation based image. 100

V.2. SSCSCT CNR for phantom #2 - tungsten spectra: 80, 120, 140 kVp; 128 view angles; ×100 data set. θ = scatter angle. The 0° image is the FBP attenuation based image. 100

V.3. SSCSCT SNR for phantom #2 - tungsten spectra: 80, 120, 140 kVp; 128 view angles; ×100 data set. θ = scatter angle. The 0° image is the FBP attenuation based image. 101

V.4. Ratio of SNR simulation measurements between SSCSCT to FBP CSCT ×100 data of Chapter IV table IV.10. 101

LIST OF FIGURES

Figure Page

I.1. Detected scatter pattern produced from photon scatter off of a rectangular 2 cm thick paraffin wax sample in a pencil-beam geometry. This particular sample appears to have been cooled quickly after being formed, which created small crystalline structures that contributed to the generation of point intensities in the image. 3

I.2. Pencil-beam geometry illustrating forward azimuthal isotropic photon scattering from an amorphous object. 6

II.1. Pencil-beam geometry illustrating forward azimuthal isotropic photon scattering from an amorphous object. L = distance from center of the object to the detector plane, D = distance from source to the center of the object, θ is the photon scattering angle, R = is the distance a scattered photon traveled from the scattering volume to the detector. A lead disk was positioned on detector in order to block un-attenuated primary beam photons from being recorded by the detector, hence the absence of signal in the middle of the detector plane. 12

II.2. Source characteristics. 14

II.3. Raw laboratory signal profiles. The zero signal region at low angles is due to the lead beam stop on the detector attenuating incoming x-rays. 15

II.4. Scatter data profiles. 17

II.5. (a) Comparison of laboratory and EGS5 simulated photon scatter distribution from 1cm of beef fat. Laboratory data plotted as dots with error bars representing one standard deviation of the measured data. Simulated data plotted as a continuous stair step. (b) Quantile - Quantile plot. (c) Scatter plot. 21

II.6. (a) Comparison of laboratory and EGS5 simulated photon scatter distribution from 1cm of beef muscle. Laboratory data plotted as dots with error bars representing one standard deviation of the measured data. Simulated data plotted as a continuous stair step. (b) Quantile - Quantile plot. (c) Scatter plot. 23

II.7. (a) Comparison of laboratory and EGS5 simulated photon scatter distribution from 1cm of water. Laboratory data plotted as dots with error bars representing one standard deviation of the measured data. Simulated data plotted as a continuous stair step. (b) Quantile - Quantile plot. (c) Scatter plot. 25

III.1. Pencil and fan-beam scatter patterns 28

III.2. Multi-element detector configuration 29

III.3. Phantom #1; 10 cm outer diameter. 30

III.4. Fan-beam geometry 33

III.5. Oblique view of simulation geometry (not to scale); source is coplanar with 577 central detection elements. The photon transport space is defined as a rectangular space with dimensions 1 mm wide x 175 mm high x 700 mm long. This corresponds to dimensions of a single detection column and the distance from the source to the detector elements plus 10 cm. 34

III.6. EGS5 simulated scatter patterns produced by four separate monoenergetic x-ray beams incident upon two different homogeneous cylindrical phantoms for the geometry illustrated in figures III.4 and III.5. Top row: 10 cm diameter of simulated adipose tissue; bottom: 5 cm diameter of simulated muscle tissue. (a) 30 keV, (b) 50 keV, (c) 70 keV, and (d) 90 keV. Primary photons within the source plane have been removed to reduce the display dynamic range in order to visually enhance the scatter out of the source plane 37

III.7. Simulated scatter profiles produced from a homogeneous (a) 10 cm diameter cylindrical phantom of fat and (b) a 5 cm diameter cylinder phantom of muscle obtained in the fan-beam geometry at 30 keV, 50 keV, 70 keV, and 90 keV. 38

III.8. Comparison of simulated scatter profiles of photon scatter from separate homogeneous fat and muscle cylindrical phantoms at 30 keV, 50 keV, 70 keV, and 90 keV. 38

III.9. FBP reconstruction of object from simulated scatter data for 30keV, 50keV, 70 keV, and 90 keV x-ray beams. Column (a) is attenuation only data (traditional CT), remaining columns are CSCT images produced from coherent scatter at angles: (b) 2.3°, (c) 5.0°, and (d) 9.8°. Sinograms used for each reconstruction are positioned directly above each tomogram. See figure III.3 for phantom diagram. 40

III.10. Sampling scatter windows relative position to scatter profiles. 41

IV.1. Phantom #2 46

IV.2. Simulated energy spectra. 49

IV.3. Simulated energy spectrum (32 kVp Mo). Same as figure II.2(a). . . 51

IV.4. 10 cm diameter CIRS model 007A phantom with Exradian A101 pencil ionization chamber. 52

IV.5. CSCT reconstructions for monoenergetic beams (30, 50, 70, 90 keV); 65 view angles; ×1 number of source photons. 55

IV.6. CSCT reconstructions for monoenergetic beams (30, 50, 70, 90 keV); 65 view angles; ×10 number of source photons. 56

IV.7. Absolute difference in contrast between ×1 and ×10 measurements. . 57

IV.8. % increase in CNR for beef fat between images in figure IV.5 and IV.6. 61

IV.9. % increase in SNR from ×1 to ×10 the number source photons. . . . 63

IV.10. CSCT reconstructions for monoenergetic beams (45, 60, 75, 85 keV); 128 view angles. 66

IV.11. 128 view angles; CSCT reconstructions for tungsten spectra with ×1 number of source photons. 71

IV.12. 128 view angles; CSCT reconstructions for tungsten spectra with ×10 the number of source photons used in figure IV.11. 72

IV.13. 128 view angles; CSCT reconstructions for tungsten spectra with ×100 the number of source photons used in figure IV.11. 73

IV.14. % increase in SNR from ×1 to ×10 & from ×1 to ×100 the number of source photons. 78

IV.15. 128 view angles; CSCT reconstructions for Molybdenum spectra at 32 kVp; right column used ×10 more photons than the left column. . 80

IV.16. Monoenergetic beams: dose per 1×10^{10} photons to phantom #2 material regions. 84

IV.17. Polyenergetic beams: dose per 1×10^{10} photons to phantom #2 material regions. 86

IV.18. Horizontal line profiles across selected attenuation based images. The image produced from the Mo 32 kVp has a cupping artifact due to the attenuation of the lower keV photons at the surface of the phantom. A ratio of the boundary to center pixel values is ∼1.6. 87

IV.19. Composite image fat enhancement for 80 kVp. R is the ratio of the average water pixel values of the 3° image to average water pixel values in the 7.4° image. 91

V.1. Example of back trajectory reconstruction for a single view angle (1 of 128) for 120 kVp at a scatter angle of 2.3°. 95

V.2. Example of ACF applied to data for 120 kVp and scatter angle 1.7°. 97

V.3. SSCSCT reconstructed images from a polyenergetic source. 99

B.1. Plot of the Thomson differential cross section per unit solid angle $(d\sigma/d\Omega)_T$ and the differential cross section per unit angle $(d\sigma/d\theta)_T$, as a function of photon scatter angle. Units are in milli-barns per sr and rad, respectively. 113

B.2. Plot of the coherent form factors for water provided EGS5 and from reference [42]. 115

B.3. Result of simulated scatter detections in EGS5 with coherent scatter modeling activated and de-activated. 117

C.1. Z-axis dose profile for multiple axial scans. N×T = beam width dimension. The rectangular area (MSAD×NT) is equal to the integrated dose under a single dose profile. 118

LIST OF ABBREVIATIONS

$\Delta\Omega$	Solid angle subtended by detector element
λ	Wavelength
$\left(\frac{d\sigma}{d\Omega}\right)_{coh,a}$	Atomic coherent differential scattering cross section per unit angle
$\left(\frac{d\sigma}{d\Omega}\right)_{coh,mol}$	Molecular coherent differential scattering cross section per unit angle
$\left(\frac{d\sigma}{d\Omega}\right)_{coh}$	Coherent differential scattering cross section per unit solid angle
$\left(\frac{d\sigma}{d\Omega}\right)_{inc}$	Incoherent differential scattering cross section per unit solid angle
$\left(\frac{d\sigma}{d\Omega}\right)_{KN}$	Klein-Nishina form factor
$\left(\frac{d\sigma}{d\Omega}\right)_{tot}$	Combined coherent and incoherent differential cross section
$\left(\frac{d\sigma}{d\Omega}\right)_{T}$	Thomson differential scattering cross section per unit solid angle per free electron
$\left(\frac{d\sigma}{d\theta}\right)_{T}$	Thomson differential scattering cross section per unit scattering angle rad^{-1}per free electron
μ	Linear attenuation coefficient
σ_{coh}	Coherent scatter cross section
θ	Scattering angle
b	barns $= 10^{-28}m^2$
c	speed of light $= c = 2.998 \times 10^8 m/s$
$F_a^2(x, Z)$	Atomic form factor
$F_{mol}^2(x)$	Molecular form factor
M	Multiple scatter component
N_0	Number of primary beam incident photons
$n_0(l)$	Number of scatter centers per unit volume at l
r_e	Classical electron radius $= \frac{e^2}{mc^2} = 2.82 \times 10^{-15}m$
T_p	Transmission of incident photons
T_s	Transmission of scattered photons
x	Momentum transfer argument nm^{-1}

Z	Atomic number
EGS4	Electron Gamma Shower version 4 - particle Monte Carlo system
EGS5	Electron Gamma Shower version 5 - particle Monte Carlo system
EGSnrc	Canadian National Research Council modified version of EGS4
FBP	Filtered Back Projection
GEANT4	GEometry ANd Tracking - particle Monte Carlo system
ICRU	International Commission on Radiation Units
MCNP	Monte Carlo N-Particle Transport Code - particle Monte Carlo system

CHAPTER I

INTRODUCTION

Coherent Scatter Computed Tomography (CSCT)

Coherent Scatter Computed Tomography (CSCT) is an imaging technique that uses the coherent scattering properties of a material to produce images. In traditional Computed Tomography (CT), reconstructed 2D tomogram represent the spatial distribution of the linear attenuation properties of an object relative to the attenuation properties of water. In contrast, CSCT generates images from scattered photons that reflect the scattering properties of an object. Scattered photons are always present in any radiographic examination and have generally been an unused source of information[54].

At photon energies (∼20-140 keV) used in diagnostic radiography, the primary photon interactions of concern are the photo-electric effect, Compton (incoherent) scatter, and Rayleigh (coherent) scatter.[1] Coherent scatter refers to the elastic scattering of x-ray photons into a new direction without loss of energy; it is strongly forward-peaked and dominates over Compton scatter at low scatter angles ($0° - 10°$)[23]. Coherent (Rayleigh) scatter is the result of a resonant interaction with the bound electrons of an atom or molecule. In contrast, incoherent (Compton) scattering occurs when an

[1] In this work, the term "Rayleigh scatter" and "coherent scatter" are used interchangeably to describe the phenomenon of photon elastic scatter by atomic electrons. Some purists may object since Rayleigh scattering is just one type of photon elastic scattering contributing to the total coherent scattering process. Photons may also undergo elastic scattering with the nucleus (i.e., nuclear Thomson scattering, Delbruck scattering – a radiative correction to nuclear Thomson scattering, and nuclear resonance scattering)[27]; however, these interactions occur well above the diagnostic energy range, and thus are of no concern. Hence, the synonymous use of "Rayleigh scatter" and "coherent scatter" to describe photon elastic scattering with matter.

incident x-ray interacts with a free or weakly bound electron where there is a measurable amount of momentum transferred, resulting in energy loss and a change in the direction of the outgoing x-ray.

Due to the fixed spatial arrangement of atoms within a specific molecule, Rayleigh scatter results in an inter-atomic interference pattern that is characteristic of the molecular structure; it dominates over Compton scatter at low x-ray energies in low-Z materials, and in well ordered systems such as crystals, produces well defined interference patterns that reveal the underlying unit cell symmetry. In contrast, amorphous materials do not exhibit distinct point diffraction patterns, but rather exhibit a cylindrically symmetric characteristic coherent scatter pattern[14].

Tissue, though not perfectly amorphous, produces a cylindrically symmetric scatter pattern that is determined by its molecular composition. Several investigators exploited this property to analyze a range of medically relevant materials; examples include the mineral composition of bone[2, 47] and urinary calculi[9], breast tissue samples for cancer diagnosis[12, 46], and the extent of cancerous invasion in collagen-breast tissue[46, 24]. These investigators illustrated the potential clinical utility of utilizing coherent scatter in medicine.

The acquisition geometry of CSCT requires the detection of photons scattered in the forward direction from the primary beam path (pencil or fan-beam). Reconstructed CSCT images are highly dependent upon the angle of photon detection from the scattering medium. The scatter angle depends on the atomic arrangement of the scattering centers within a specific molecule and the energy of the incoming photon[23, 16, 15, 17, 55, 60, 61]. For a pencil-beam acquisition geometry, a cylindrically-symmetric diffraction pattern results because there is no preferential molecular orientation in amorphous material (see figure I.1). The detected scatter signals may then be be reconstructed into images, which are indicative of the coherent scatter properties of the scattering object.

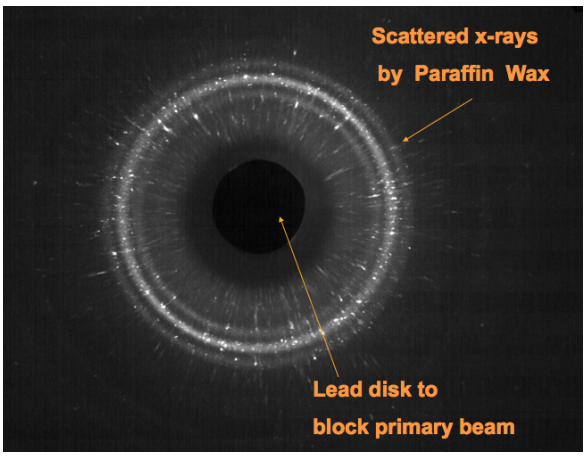

Figure I.1: Detected scatter pattern produced from photon scatter off of a rectangular 2 cm thick paraffin wax sample in a pencil-beam geometry. This particular sample appears to have been cooled quickly after being formed, which created small crystalline structures that contributed to the generation of point intensities in the image.

Coherent Scatter Modeling

Rayleigh (coherent) scattering is typically characterized by using the form factor approximation where the atomic coherent differential cross section (scattering amplitude) per unit solid angle ($(d\sigma/d\Omega)_{coh,a}$) is written in terms of a coherent scattering atomic form factor ($F_a(x, Z)$), which incorporates the atomic electronic configuration, and the Thomson differential electronic cross section:

$$\left(\frac{d\sigma}{d\Omega}\right)_{coh,a} = \left(\frac{d\sigma}{d\Omega}\right)_T F_a^2(x, Z), \tag{I.1}$$

where

$$\left(\frac{d\sigma}{d\Omega}\right)_T = \frac{r_e^2}{2}(1 + \cos^2\theta), \tag{I.2}$$

is the Thomason differential cross section per solid angle per free electron and θ is the photon scattering angle. The momentum transfer argument x is defined as:

$$x = \frac{\sin(\theta/2)}{\lambda}, \tag{I.3}$$

and is dependent upon the incoming photon wavelength (λ) and has units of inverse length.

From the classical view point, $F_a(x, Z)$ is the Fourier transform of the electron charge density surrounding the nucleus; it characterizes the effective charge that scatters a photon by modifying $(d\sigma/d\Omega)_T$, and it is calculated from various atomic models with varying degrees of complexity (e.g., Thomas–Fermi, Hartree, Hartree–Fock, S-matrix). Tabulated atomic form factor tables are typically reported in terms of x.

The momentum transfer argument, x, plays a fundamental role in scattering theory: all scatter measurements can be reduced to the determination of scatter intensity for all possible values of x[14]. It relates the incoming photon energy ($\lambda = c/\nu$) and photon scatter angle (θ) together into a single variable. For CSCT, the typical momentum transfer range of concern is $0.5\ nm^{-1} \leq\ x\ \leq 5\ nm^{-1}$[17]. Above $\sim 5\ nm^{-1}$, free-atom behavior is observed where interference effects are due to intra-atomic electrons.

To allow particle transport Monte Carlo systems (e.g., GEANT4, EGS4, EGS5, EGSnrc, MCNP) to treat compounds and mixtures generally, the total molecular coherent scatter cross section, σ_{coh}, and $F_{mol}(x)$ are calculated from tabulated atomic data as a weighted sum of the individual atomic constituent. Specifically, the molecular form factor for a given compound is calculated as a weighted sum of individual atomic properties:

$$F_{mol}^2(x) = \sum_i \rho_i F_a^2(x, Z_i), \tag{I.4}$$

where $F_{mol}(x)$ is the coherent scatter molecular form factor, x is the momentum transfer argument, ρ_i is stoichiometric ratio of the i^{th} element in the molecule/mixture/compound, and $F_a(x, Z_i)$ is the atomic form factor for i^{th} element.

This method of calculating $F^2_{mol}(x)$ is known as the independent atomic approximation (IAA) method. Although accurate at high momentum transfer, at low momentum transfer the IAA fails to correctly model the interference effects of coherent scatter[23, 7, 32, 31, 51, 41]. The IAA approach only accounts for coherent scatter from intra-atomic electrons; it does not incorporate inter-atomic coherent scatter from other atoms in a molecule, which are present in empirical diffraction data at low momentum transfers[51, 57, 58]. Leliveld (1996) illustrated the pronounced discrepancies between IAA calculated molecular form factors and the empirical molecular form factor data of Morin (1982)[37] and Kosanetzky (1987)[29].

Most particle Monte Carlo systems use the IAA method to determine form factors and coherent cross section for materials; however, EGS4[32], EGSnrc[41], and EGS5[18] can use user-supplied empirical molecular form factors ($F^2_{mol}(x)$) and coherent scattering cross sections (σ_{coh}), which incorporate the inter-atomic interference effects of coherent scatter at low angles. Analytically, integrating the $F^2_{mol}(x)$ with the $(d\sigma/d\Omega)_T$ yields the total molecular coherent scatter cross section, $\sigma_{coh} = \int_0^\pi (d\sigma/d\Omega)_T F^2_{mol}(x) d\theta$, which is the probability of a photon to undergo a coherent interaction in a particular material. Although no single repository exists for measured molecular form factors, several authors have compiled empirical data on medically relevant materials[11, 12, 42, 44, 46, 47, 49, 24, 57, 58, 22, 10, 57, 59]. In this work we have chosen to use the coherent scatter molecular form factors and cross sections that were supplied with the EGS5 distribution.

Coherent scatter theory in CSCT

Tomographic image reconstruction from coherent scatter patterns was first developed by Harding (1985, 1987). What follows is a description of his theory as modified by Westmore (1997) and shortened by Batchelar (2002). Figure I.2 is the pencil-beam geometry used to explain the acquisition geometry.

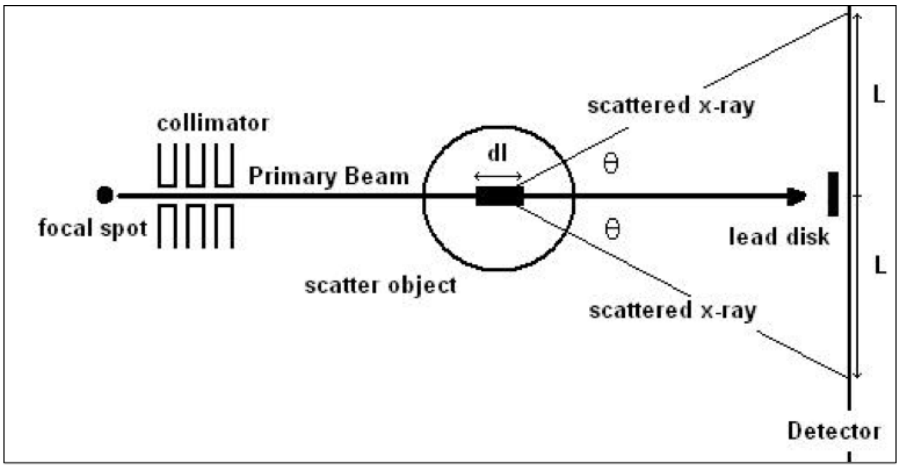

Figure I.2: Pencil-beam geometry illustrating forward azimuthal isotropic photon scattering from an amorphous object.

The number of x-ray photons $dN(\theta)$ scattered at angle θ into the detector element dA from the segment dl located at a distance l within the object is described as

$$dN(\theta) = N_0 T_p(l) n_0(l) \left(\frac{d\sigma}{d\Omega}[l, x(\theta, l)] \right)_{tot} \Delta\Omega(\theta, l) T_s(l) dl + M, \tag{I.5}$$

where N_0 is the number of primary beam incident photons, $T_p(l)$ is transmission fraction of primary beam photons to object element dl, $n_0(l)$ is number of scatter centers per unit volume at l, $x(\theta, l)$ is momentum transfer for object element at l, $\Delta\Omega(\theta, l)$ is solid angle subtended by detector element dA, $T_s(l)$ is transmission of scattered beam from l to dA, M is multiple scatter component, and $(d\sigma/d\Omega)_{tot}$ is the combined coherent and incoherent differential cross section per unit volume per scattering center,

$$\left(\frac{d\sigma}{d\Omega} \right)_{tot} = \left(\frac{d\sigma}{d\Omega} \right)_{coh} + \left(\frac{d\sigma}{d\Omega} \right)_{inc}, \tag{I.6}$$

where $(d\sigma/d\Omega)_{coh}$ is the differential coherent cross section, and $(d\sigma/d\Omega)_{inc}$ is the differential incoherent cross section. A series of simplifying assumptions transforms

equation I.5 into a more manageable equation for image reconstruction purposes. These are:

- The multiple scatter component, M, can be neglected or removed if the object size is $< \sim 3$ half value layers[61].
- Attenuation is identical for all path lengths through the object, that is, $N_0 T_p T_s = N_t$ is a constant and equal to the number transmitted through the object[61].
- The l dependence of x and $\Delta\theta$ is negligible when the object-detector separation is large compared to object size ($L \gg l$)[61].

With these assumptions, the number of x-ray photons scattered into the detector element dA from object element dl is

$$dN(\theta) \approx N_t n_0(l) \left(\frac{d\sigma}{d\Omega}[l, x(\theta)] \right)_{tot} \Delta\Omega(\theta) dl, \tag{I.7}$$

where each scatter pattern measured by the area detector is just the integration of the x-ray fluence over each detection element. The scatter fluence at dA from object element dl is $d\Phi(\theta) = dN(\theta)/dA$.

Since amorphous materials produce azimuthally symmetric diffraction patterns (see figure I.1), analysis of how many photons are scattered into the i^{th} annulus of width dr on the detector from object element dl may be written as

$$dN_i \approx N_t n_0(l) \left(\frac{d\sigma}{d\Omega}[l, x(\theta_i)] \right)_{tot} \Delta\Omega_i dl \tag{I.8}$$

The total number of scattered x-ray photons in the i^{th} annulus is found by integrating along the path length l through the object:

$$N_i \approx N_t \Delta\Omega \int_l n_0(l) \left(\frac{d\sigma}{d\Omega}[l, x(\theta_i)] \right)_{tot} dl \tag{I.9}$$

Normalizing this equation by the unit solid angle per transmitted x-ray ($\Delta\Omega_i N_t$) yields:

$$Q_i = \frac{N_i}{\Delta\Omega_i N_t} \approx \int_l \left(\frac{d\sigma}{d\Omega}[l, x(\theta_i)]\right)_{tot} dl = \int_l \gamma[l, x(\theta_i)] dl \tag{I.10}$$

where

$$\gamma[l, x(\theta_i)] = n_0(l) \left(\frac{d\sigma}{d\Omega}[l, x(\theta_i)]\right)_{tot} \tag{I.11}$$

is the differential linear coherent-scatter coefficient per unit solid angle. The quantity $Q_i \approx \int_l \gamma[l, x(\theta_i)] dl$ is similar in form to the measured projection line profile, $P = \int_l \mu(l) dl$, in conventional CT imaging, where $\mu(l)$ is the linear attenuation coefficient.

Since coherent scatter dominates over incoherent (Compton) scatter at low scattering angles ($\theta \sim 10^o$)[23], the total differential cross section effectively equals the coherent differential cross section, $(d\sigma/d\Omega)_{tot} \approx (d\sigma/d\Omega)_{coh}$, which implies that the differential linear coherent scatter coefficient $\gamma[l, x]$ is representative of the differential coherent scatter coefficient $(d\sigma/d\Omega)_{coh}$:

$$\gamma[l, x(\theta_i)] = n_0 \left(\frac{d\sigma}{d\Omega}[l, x(\theta_i)]\right)_{coh}. \tag{I.12}$$

Every i^{th} annulus is essentially a separate data channel from which the signal detected can be used to reconstruct i separate images. However, in principle it is not necessary to integrate the total signal in an annulus since the detector elements can take any shape[61].

Additionally, since the form of Q_i (equation I.10) is similar to the projection profile in conventional CT imaging, $P = \int_l \mu(l) dl$, the variance, $var_i\{\gamma\}$, in every i reconstructed image should also be similar in form[61]. As stated by Westmore (1997), the variance in the reconstructed value of the differential linear coherent scatter

coefficient at the center of the image is

$$var\{\gamma[x(\theta_i)]\} = \frac{\pi^2 W \gamma[x(\theta_i)]}{12 m \Delta\Omega_i N_t a^2}. \tag{I.13}$$

where a is the pixel dimension in the reconstructed image, m is the number of projection angles, W is the object width, and where $l = 0$ at the image center (l ranges from $-W \rightarrow W$). Since it is assumed that the number of photons scatted into the i^{th} detection element follows Poisson statistics, the SNR is calculated to be

$$\mathrm{SNR}_i = \frac{\gamma[x(\theta_i)]}{\sqrt{var\{\gamma[x,(\theta_i)]\}}} = \sqrt{\frac{12\gamma[x(\theta_i)] m \Delta\Omega_i N_t a^2}{\pi^2 W}}. \tag{I.14}$$

These equations demonstrate that CSCT reconstruction may be performed in the same manner as conventional CT image reconstruction and provide the foundation for the experiments performed in this work.

CHAPTER II

VERIFICATION OF COHERENT SCATTER MODELING IN EGS5

Introduction

EGS5 is designed to simulate the transport of electrons and photons in the energy range of few keV to several hundred GeV (depending on the atomic number of the target material) in an arbitrary geometry. For Rayleigh scattering, EGS5 uses the total coherent scattering cross section data for elements 1 through 100 determined by Storm and Israel[56]. For modeling interference effects, EGS5 uses pre-computed coherent cross sections and empirical form factors.

At the present tme, EGS5 has available seven medically relevant materials: water, blood, fat, liver, muscle, kidney, and plastic (poly-methyl methacrylic, PMMA)[18]. A plot of the EGS5 form factor and coherent scatter cross section data shows it to be consistent with the Peplow and Verghese (1998) data set, and for water, the data is consistent with the Morin (1982) data tables[37]. EGS5's ability to simulate Rayleigh scattering from liquid water has been shown to produce excellent agreement with empirical measurements [39].

Before investigating CSCT in a simulated environment, it was necessary to verify the reliability of EGS5 simulations to reproduce experimental molecular interference effects due to coherent scattering. A pencil-beam acquisition geometry was used to record the scatter pattern produced from three different 1 cm thick samples (liquid water, beef fat, and beef muscle). Laboratory and simulated normalized angular scatter distributions were then compared utilizing statistical methods in order to quantify their similarity.

Method: Pencil-beam geometry

Laboratory setup

The laboratory photon source was a GE Senographe 600T Senix H.F. mammography unit with a molybdenum anode, a 0.3 mm focal spot, an x-ray tube window of 0.8 mm of Beryllium, and an operating range of 22 - 49 kVp and 4 - 600 mAs. The unit's molybdenum and aluminum filters were removed along with the unit's lead collimators and replaced with custom pin-hole Pb collimators. These collimators consisted of three separate 2 mm thick sheets of lead with a single pin-hole opening in the center of each sheet. The pin-hole openings of 5 mm, 3 mm, and 4 mm were aligned with the primary beam axis and the sheets positioned at 17 cm, 20 cm and 25 cm from the tube focal spot, respectively. This was done in order to collimate the beam down to a 4 mm diameter pencil-beam at the surface of the sample and to minimize its divergence, while simultaneously allowing enough photon flux to reach the object to interact and generate a scatter pattern on the detector during its brief exposure period. Figure II.1 illustrates the laboratory pencil-beam acquisition geometry. The tube was operated at 600 mAs and 32 kVp. While no spectral measurement was obtained for the x-ray tube, it was assumed that the tube did not differ significantly from published molybdenum energy spectrums, such as those published by Boone et al (1997).

A flat panel amorphous selenium mammography detector (LMAM, Anrad, Montreal, Canada) with a pixel pitch of 85 μm and an image matrix of 3585 x 2816 pixels was used to measure the scattered x-rays. The detector operated with a bias voltage of 2000 V and had a maximum active exposure time window of 7 seconds during which an exposure could be recorded. Prior to every exposure, the detector software recorded the detector dark current and applied a correction to the x-ray generated photocurrent. It was assumed that the detector response was linear with mAs and

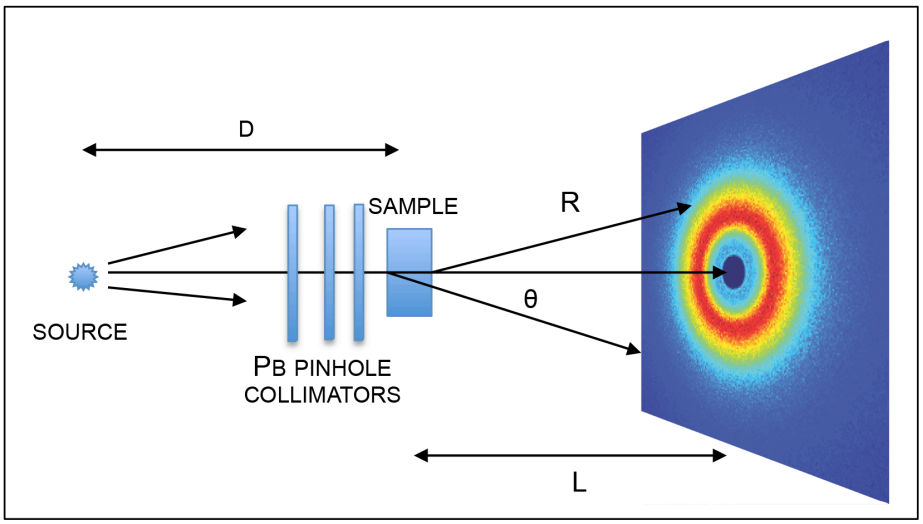

Figure II.1: Pencil-beam geometry illustrating forward azimuthal isotropic photon scattering from an amorphous object. L = distance from center of the object to the detector plane, D = distance from source to the center of the object, θ is the photon scattering angle, R = is the distance a scattered photon traveled from the scattering volume to the detector. A lead disk was positioned on detector in order to block un-attenuated primary beam photons from being recorded by the detector, hence the absence of signal in the middle of the detector plane.

uniform over the kVp range used for the experiment. To avoid over-ranging the detector when using a 600 mAs technique, a 1 mm thick lead disk was used as a beam stop to block any un-scattered primary beam photons. This allowed use of the full digital dynamic range (13 bits) to be allocated to the scattered radiation detection.

As mentioned previously, 1 cm thick samples of beef fat, beef muscle (sirloin cut), and purified liquid water were used. The beef fat and muscle samples were obtained at a local grocery store and cut into roughly 5 cm x 4 cm rectangles that were 1 ± 0.1 cm thick. The beef muscle was positioned such that the axis of the x-ray beam was perpendicular to the muscle grain. For liquid water, the sample was contained by a 0.2 mm thick nitrile container with the total sample thickness along the x-ray transmission axis being 1 ± 0.1cm. Blank samples taken with only the thin nitrile container produced no measurable scatter above that produced by air alone, therefore

no container correction to the water scatter data was applied. The center of all samples were located 27.8 ± 0.2 cm from the detector surface.

Simulation setup

For the simulation, an x-ray spectrum generated using the MASMIP (molybdenum anode spectral model using interpolating polynomials) technique published by Boone, Fewell, and Jennings[4] was used as an approximation to the laboratory source photon energy spectrum. In order to simplify coding the source, the primary beam was considered to be non-diverging; the simulated x-ray beam consisted of parallel rays directed along the source-to-detector axis with an area density that was Gaussian distributed with a FWHM of 3.4 mm in diameter. A visual representation of the source energy distribution and photon areal density is illustrated in figure II.2.

The simulated detector was modeled as a single block of selenium with dimensions of 20 cm x 20 cm x 1 cm. X-ray photons that reached the plane of the detector were terminated and had their energy, direction vectors, and positions recorded; positions were addressed into a 200 x 200 image matrix. This aspect made the simulated detector a photon counter and not an energy integrator like the laboratory detector, which generated a signal based on the amount of electron-hole pairs created in the solid state photoconductor medium by an interacting x-ray photon. However, the focus of the simulation was not to model detector performance, but to determine whether or not the methods used in EGS5 properly modeled coherent scatter from various materials.

The source was positioned 60 cm from the face of the detector and 30 cm from the center of a 10 cm x 10 cm x 1cm sample targets. Using the energy spectrum in figure II.2 (a), a total of 555,547,036 photons were shot at each sample, this corresponded to a maximum of 1×10^8 photons at 17.5 keV. The detected scatter pattern was then processed for comparison with the laboratory data.

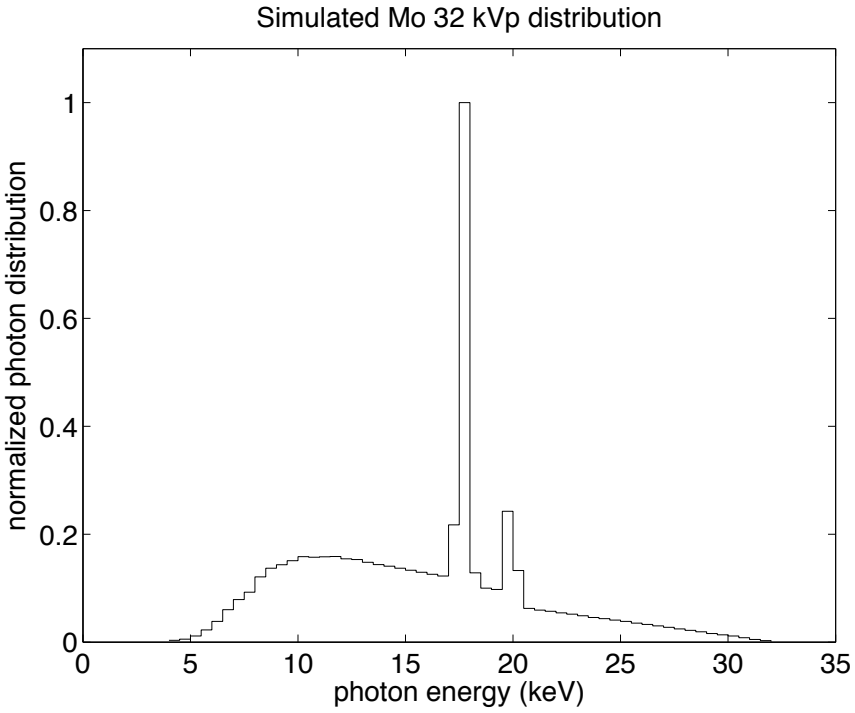

(a) Simulated energy spectrum (32 kVp Mo).

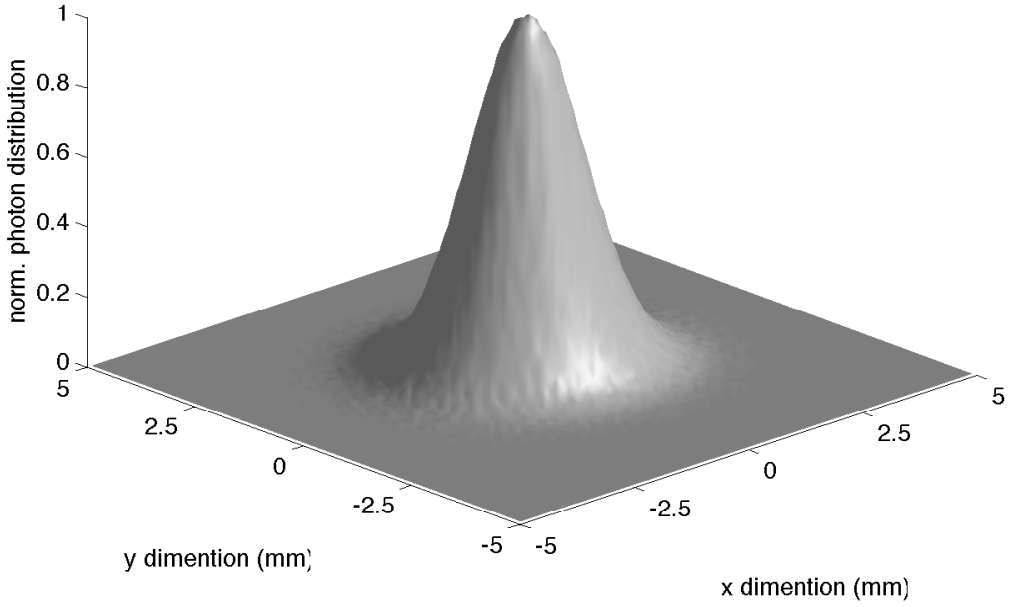

(b) Spatial distribution of photon emitted from the source – FWHM ∼3.4 mm. The z-axis represents the number of photons emitted by the source at a spatial positions (x,y) normalized by the max number of photons emitted at a position (0,0).

Figure II.2: Source characteristics.

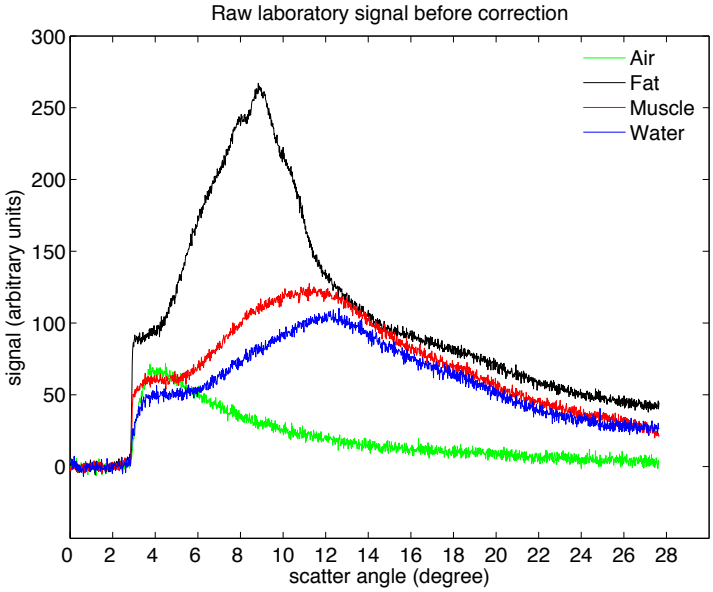

Figure II.3: Raw laboratory signal profiles. The zero signal region at low angles is due to the lead beam stop on the detector attenuating incoming x-rays.

Measurement processing

Laboratory Data

Multiple images were obtained and averaged to achieve comparable noise level with and without samples in the beam path. The National Institutes of Health's public domain software ImageJ[1] was used to make measurements on the 2D images. A rectangular ROI (1.1 mm x 146.7 mm) was used to extract a scatter profile in the same location on each image. The ROI spanned an angular range from zero degrees (center of the primary beam) to 27.7 degrees (edge of the image). Within each ROI the signal was averaged along the shortest dimension. The ROI measurements for each sample were used to calculate a sample average signal profile and its associated standard deviation at each angular location. The standard deviation served as the measure of uncertainty in the signal. All calculations used standard propagation of error methods. Uncorrected average scatter signal profiles are plotted in figure II.3.

Signal profiles generated from Air-only images (referred to as blank from here on)

were multiplied by a correction factor and then subtracted from each average material signal profile. This was necessary in order to correct each material signal profile for scatter due to beam geometry effects (i.e., beam divergence and asymmetry). A separate correction factor was determined for each of the three material by calculating the sample-to-blank scatter signal ratio in angular region of 4 to 6 degrees. As can be seen in figure II.3, in this angular region the fat sample produced a higher scatter signal than did the blank; therefore, the constant was set to 1.0 and the entire blank signal was subtracted from the fat signal to generate a corrected scatter profile, which now represents the scatter in this region due to sample only. An example of a corrected laboratory signal profile are plotted in figure II.4 (a). Each profile was normalized by the maximum fat scatter signal in order to preserve in the plot the relative amount of scatter each sample produced. Plotting the normalized signal was chosen over plotting the relative probability, since it made it more manageable to statistically compare the laboratory and simulated distributions due to their unequal grid sampling in scatter angle, although the relative probability could have been selected as long as the scatter angle integral range was the same for both the laboratory and simulated data sets.

Simulated Data

Simulated data was processed in a similar manner as the laboratory data. For each material and the blank, a total of eight sample signal profiles were combined to generate an average sample signal profile. These simulated profiles were corrected by the simulated blank and are shown in figure II.4 (b). For the this data set, the simulated lead beam stop covered a larger detector area. The zero signal region extends up to 4 degrees; in comparison the laboratory data zero signal region extended only to about 3 degrees.

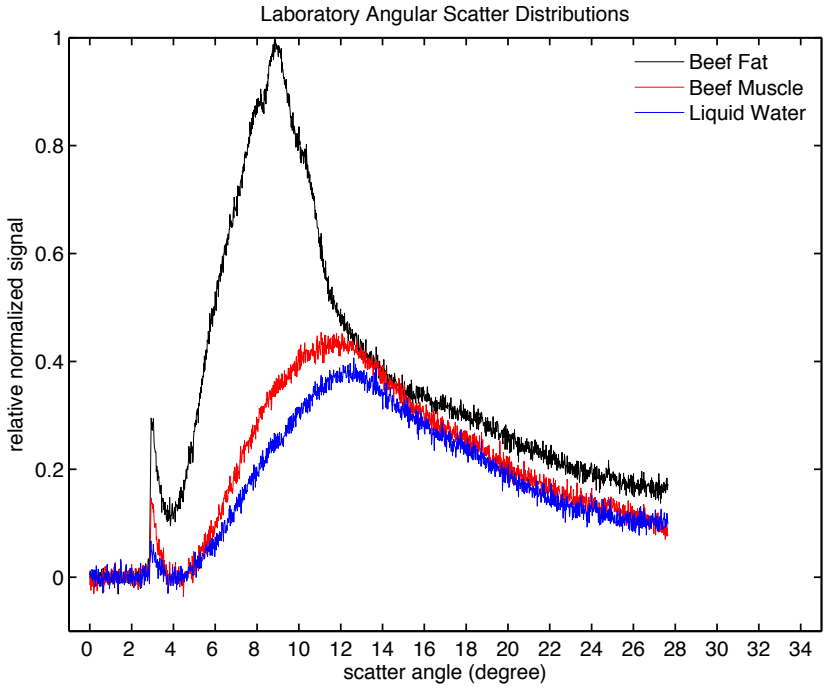

(a) Laboratory Mo 32 kVp pencil-beam scatter profiles. Due to the detection geometry setup, scatter angle measurements were limited to $\leq 27.7°$.

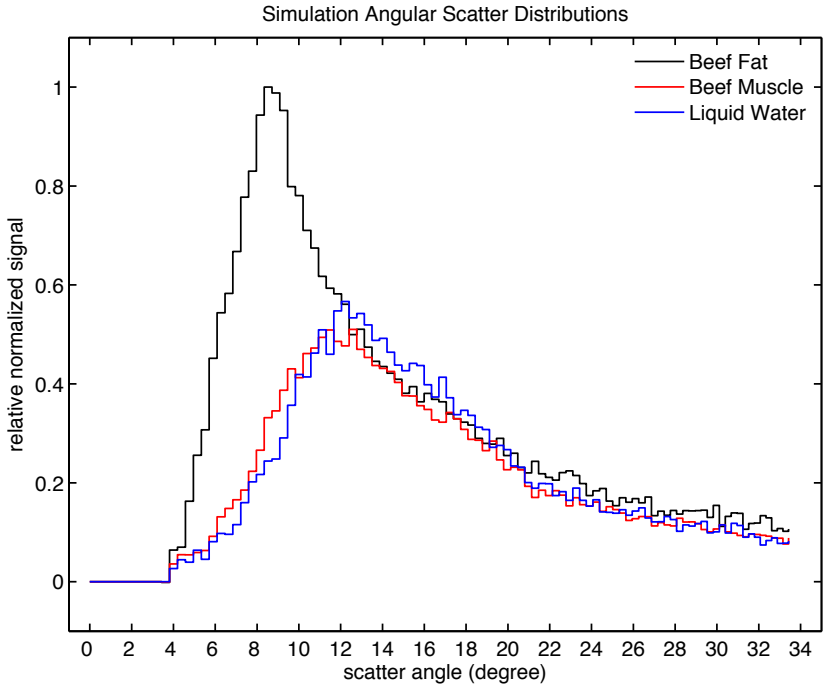

(b) Simulation Mo 32 kVp pencil-beam scatter profiles.

Figure II.4: Scatter data profiles.

Distribution Comparison

The corrected profiles (distributions) in figure II.4 (a) and (b) were compared to each other using several statistical methods to measure the goodness of fit. The use of several methods to compare experimental and simulated results provided greater confidence that the observations were valid. The MATLAB© [34] $statistical toolbox was used to perform$

Since each laboratory distribution contained 1727 scatter angle measurements covering 27.7 degrees and each simulated profile only had 100 measurements covering 33.4 degrees, the laboratory distribution was sampled by linear interpolation on the same grid as the simulated data. No extrapolation was performed for scatter angles larger than 27.7 degrees. Therefore, all statistical measures of distribution similarity occurred for angles $\leq$ 27.7 degrees where the laboratory and simulated data overlap.

The comparison of the interpolated empirical values and associated simulated values is plotted in figures II.5(a) to II.7(a). The uncertainty in an empirical measurement is shown as an error bar, which indicates plus or minus one standard deviation. The plots were normalized by the maximum signal in each distribution.

The Q-Q plot (quantile-quantile plot) is a graphical statistical goodness-of-fit method that allows two distributions to be compared by plotting their quantiles against each other. Quantiles are the set of values that a random variable can take at regular intervals from a cumulative distribution function (CDF), which separate an ordered data set into separate data subsets of roughly equal size[62]. Quantiles are the boundary location between consecutive subsets. Generally, Q-Q plots are used to compare theoretical models and experimental data, providing a graphical "goodness of fit" Q-Q plots for the fat, muscle, and water samples are plotted in part (b) of figures II.5 to II.7, respectively.

The scatter plot provided a quick visual estimate of similarities between profile distributions. A standard scatter plot of the sorted (ordered) laboratory and simulated distributions is shown in part (c) of figures II.5 to II.7, respectively. A line of slope one

is plotted as a visual reference illustrating virtual linearity of the data when compared with each other.

A paired t-test was performed between the laboratory and simulated distributions to determine whether their values come from parent distributions with the same mean. This test served as a rather rough estimate of similarity, since it condensed the entire profile into a single metric for comparison without concern for the profile's shape. Since the t-test is not as detailed as the other tests performed, it can provide an absolute check on non-similarity since it compares the means of the two distributions[3]. That is, if the p-value had been low ($p < 0.05$) then the profiles would have to have been grossly mismatched and the other more detailed sensitive statistical tests would not have indicated profile similarity. Results are listed in II.1 located in the Results section for this and two other statistical tests.

The Kolmogorov-Smirnov test (K-S test) is a nonparametric test for the equality between two different empirical distributions. Since it quantifies the difference between two different empirical cumulative distributions, it is sensitive to both differences in position and shape between the two samples[13]. The hypothesis that two empirical cumulative distributions are similar is rejected if the p-value < 0.05.

The final statistical test performed was the Anderson-Darling test (A-D test). The A-D test is a nonparametric test that quantifies the square of the difference between two empirical CDFs[13]. It is considered more stringent than the K-S test since it gives more weight to the tails of the distributions, thus making it more sensitive to outliers. Like the K-S test, p-values < 0.05 indicate the two empirical distributions are not similar.

Results & Discussion

Lab/sim comparison: poly-energetic beam

The results of the laboratory and simulated experiments are analyzed in this section. Table II.1 summarizes the three statistical tests quantifying the degree of similarity between the laboratory and simulated data. Comparison plots of the angular scatter distribution due to coherent photon scatter from three different materials are shown in figure II.4. The extraneous laboratory data point plotted at ∼3 degrees in part (a) of figures II.5 through II.7 is an artifact of scatter around the beam stop. It emerged when interpolating the laboratory data on the same grid as the simulated data for comparison purposes. Over all, the simulated data was found to be in good agreement with laboratory measurements as illustrated visually in figures II.5 through II.7 and as quantified in table II.1. For the statistical metrics calculated in table II.1, an entire laboratory scatter profile, which consisted of 1727 scatter measurements per material, was compared to its associated simulated profile.

Table II.1: Statistical comparison between laboratory and simulated angular scatter distributions.

	Statistical Test		
Sample	t-test (p-value)	Kolmogorov-Smirnov (p-value)	Anderson-Darling (p-value)
Beef Fat	0.965	0.485	0.318
Beef Muscle	0.900	0.885	0.627
Water	0.636	0.695	0.411

Fat

The fat data set has the lowest measurement uncertainty due to its high scattering and low attenuation properties. The molecules of fat, triglycerides, tend to be large molecules composed of long chains of hydrogen and carbon. These long chains can order themselves through intermolecular forces to compose relatively layered ordered

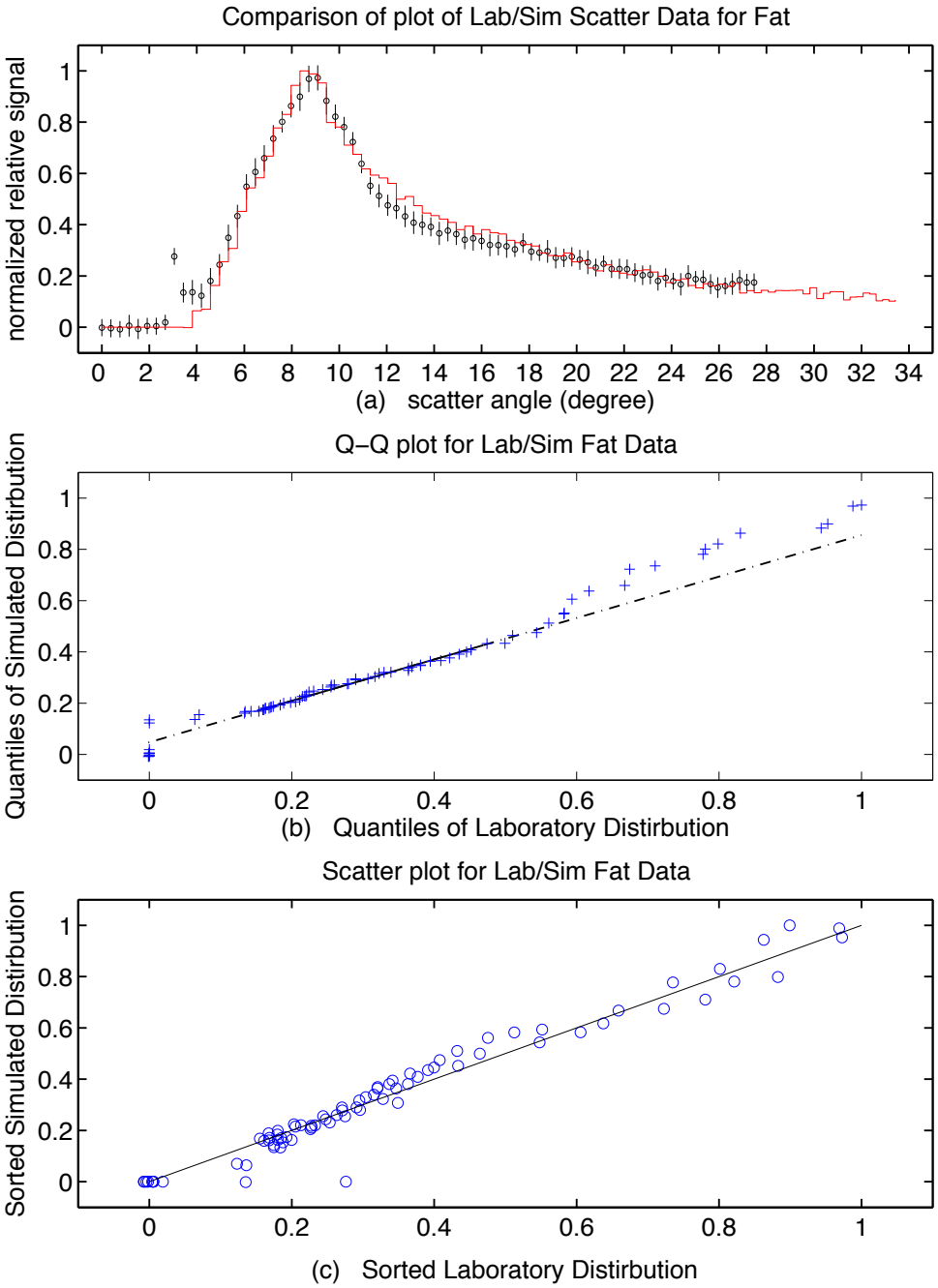

Figure II.5: (a) Comparison of laboratory and EGS5 simulated photon scatter distribution from 1cm of beef fat. Laboratory data plotted as dots with error bars representing one standard deviation of the measured data. Simulated data plotted as a continuous stair step. (b) Quantile - Quantile plot. (c) Scatter plot.

structures. It is this aspect which gives fat a more distinctive scatting profile than that of either muscle or water.

The distribution in figure II.5 shows a slight mismatch between the simulated and laboratory data for scatter angles 11 to 16 degrees. The simulated data in this region tends to under estimate the amount of scatter. It is possible that the degree of hydration in the fat sample may be slightly lower than the fat samples that were used by Peplow et al. (1998) to determine the form factors for fat. In figure II.4(a & b), between 12 and 18 degrees, the water and muscle signals are just below the fat signal. It is conceivable that a more hydrogenous fat sample may lead to an increased scatter signal in this region. In addition, the slightly wider and diverging laboratory beam may contribute more photons to higher scatter angles than does the simulated parallel beam. For example, photons traveling on an upward trajectory will scatter to high angles compared to those traveling parallel to the source-object axis. The over shoot in the simulated data fat data manifests itself clearly in the Q-Q plot, figure II.5(a), where the quintile data points drift to the simulated data axis side of the dotted line. The effects of the mismatch are seen in the K-S test for fat (table II.1), where the p-value for fat is lower than the that for water or muscle.

The scatter plot in figure II.5(c) illustrates a nearly linear relationship except at the lower angles, where the scatter around the laboratory beam stop has influenced the weighting towards the laboratory data side of the line. The t-test indicates a high degree of similarity between the profile means. All tests in table II.1 indicate that the simulated scatter distribution matches the laboratory scatter distribution for beef fat.

Muscle

Figure II.4 shows a subtle difference in the relative position of the scatter profile for muscle and water. An examination of figure II.4(a) shows that the muscle scatter signal is drawn in the direction of the fat scatter peak for the laboratory samples. A similar trend is noticed in the simulated muscle signal in figure II.4(b), where the

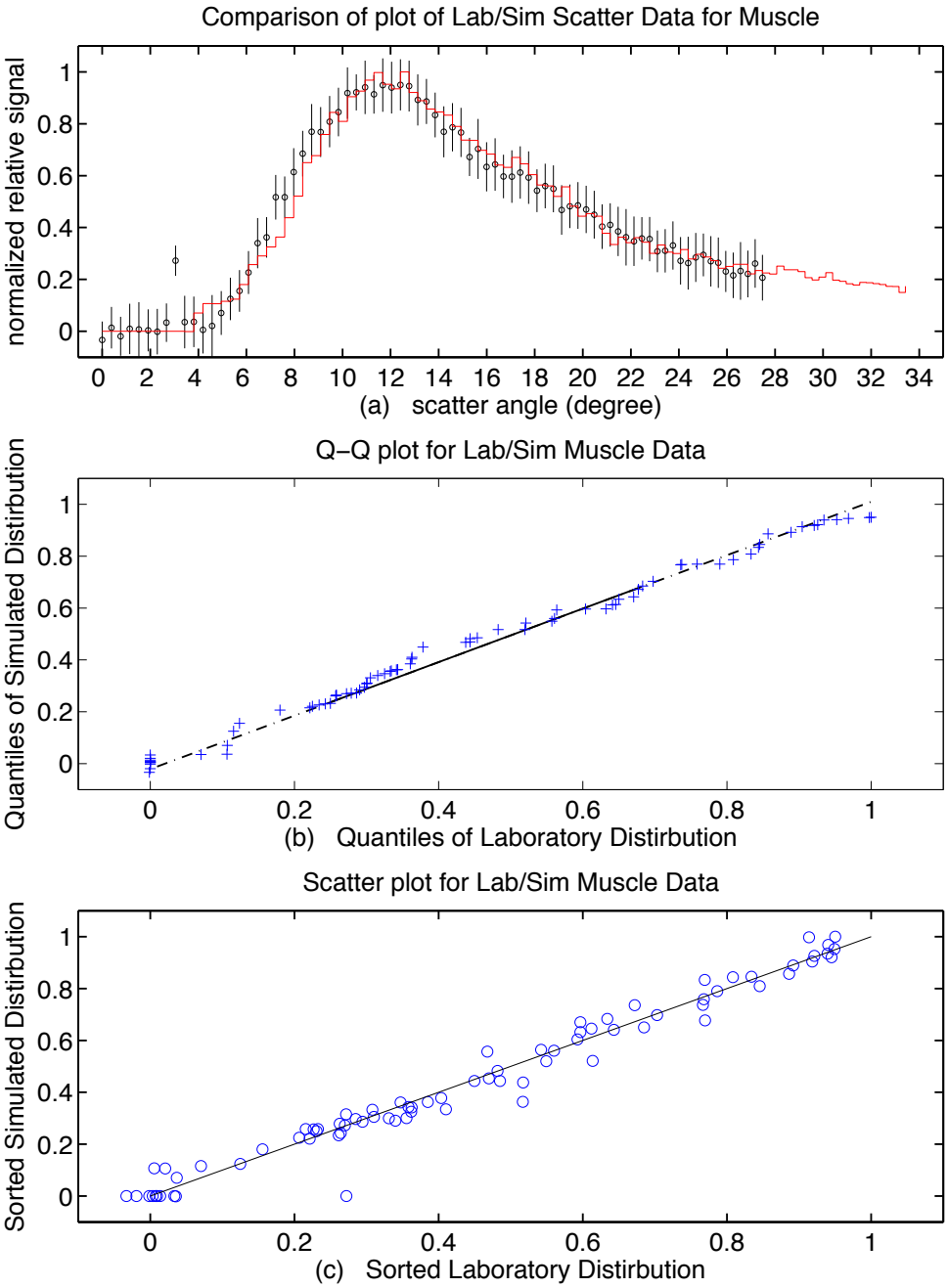

Figure II.6: (a) Comparison of laboratory and EGS5 simulated photon scatter distribution from 1cm of beef muscle. Laboratory data plotted as dots with error bars representing one standard deviation of the measured data. Simulated data plotted as a continuous stair step. (b) Quantile - Quantile plot. (c) Scatter plot.

muscle signal remains slightly higher than water signal at angles below the water peak. Just beyond the muscle scatter peak, the muscle and fat signals are roughly equivalent, after this point the two sample signals begin to diverge with the fat signal remaining higher in both data sets. The most probable explanation is that the beef muscle sample for the laboratory experiment contained a larger percentage of fat than did the beef muscle samples that were used to generate the form factors for EGS5. This may also explain why in figure II.6(b) the simulated profile tracks closely with the measured data except around 8 degrees, where the laboratory signal is slightly higher that the simulated signal. It may also be due to noise in the laboratory data as the simulated profile appears to be within the two standard deviations of the laboratory measurements.

Examination of figure II.6(a) reveals a noisier measured signal compared to the fat measurements in figure II.5(a). Muscle is composed of many different molecules that are not as strongly ordered to reinforce coherent scatter to the degree that fat molecules are, hence the lower scatter signal compared to fat in both laboratory and simulated cases. The Q-Q plot does show a subtle undulation along the unit slope line, which indicates that there are regions where the simulated data measures higher than the laboratory, and vice versa. However, the Q-Q plot for muscle (figure II.6(b)) shows an over all tighter agreement than do the fat quantiles. Also, the muscle scatter plot remains essentially linear except for the extraneous measured data point due to scatter around the beam stop. The statistical test results in table II.1 all indicate that the laboratory and simulated distributions are similar.

Water

In addition to the water - muscle profile differences mentioned in the previous section, there exists difference in the laboratory/simulated data sets between water and fat. In the laboratory data set, figure II.4(a), the water profile remains below the fat profile at all scatter angles. In the simulated data set, figure II.4(b) between

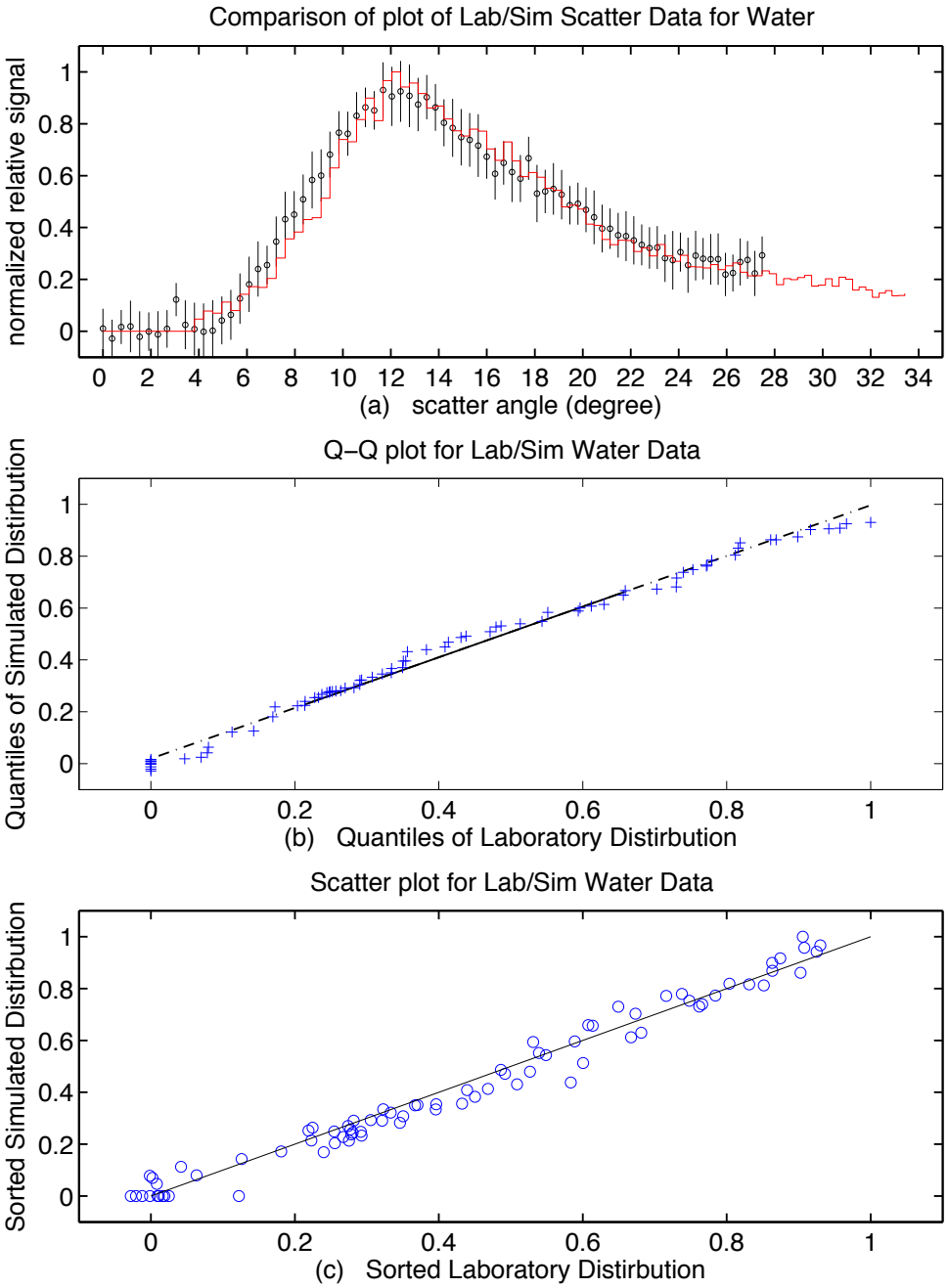

Figure II.7: (a) Comparison of laboratory and EGS5 simulated photon scatter distribution from 1cm of water. Laboratory data plotted as dots with error bars representing one standard deviation of the measured data. Simulated data plotted as a continuous stair step. (b) Quantile - Quantile plot. (c) Scatter plot.

12 to 16 degrees, the water profile is above the fat profile. As mentioned previously, these differences are likely due to the differences in the amount of hydration and/or fat content in the non-water samples.

Figure II.7 illustrates the similar properties as the muscle scatter data. The laboratory measurements are noisier than the fat measurements, and like the muscle profiles, are slightly higher than the simulated measurements in the region of 8 degrees. Again, this may be due to noise in the laboratory measurement, but since there is close agreement with the remaining data points in both the water and muscle profile, this could indicate that there is a slight discrepancy in processing the raw data profiles or in simulating scatter on the lower scatter angle side of the scatter peak. Given that the laboratory/simulated data match for higher angles, and that at scatter angles below the scatter peak the fat profiles (figure II.5) match remarkably well, it appears that the corrections applied to the scatter signal for beam geometry effects are the cause. Extending the uncertainty in the measured data to two standard deviations encompass the simulated profile. The Q-Q plot, (figure II.7(b)), shows a subtle undulation about the unit slope line like the muscle data. The scatter plot shows tight agreement, but with a slight weighting towards the laboratory data. Again the statistical measures in table II.1 support equivalency of the distributions.

Conclusion

The EGS5 simulations utilizing embedded empirical form factor for coherent scatter were found to reproduce the independently measured experimental scatter profiles from three 1 cm thick samples (beef fat, beef muscle, and water) for a polyenergetic source. Statistical measurements of the goodness-of-fit confirmed that the simulated scatter profiles are in agreement with laboratory scatter profiles. From the results it is concluded that the form factors used in EGS5 are appropriate for use in simulations to model coherent scatter effects for beef fat, beef muscle, and water.

CHAPTER III

EGS5 CSCT SIMULATIONS: PART I

Introduction

In Chapter II, a comparison of the laboratory and simulated scatter measurements for select materials indicated that EGS5 properly modeled coherent scatter interactions. In this chapter, the previously described pencil-beam geometry is used to compose a discrete fan-beam CSCT acquisition geometry. That is, a 2D fan-beam was composed of a number of individual 1D pencil-beams. The manner in which the simulation was performed essentially mimicked a system with "perfect" post-scatter collimators positioned at the detector face, which did not permit lateral photon scatter detection. A description of how this simulated geometry is achieved is explained in the next section. Extension of the scatter acquisition geometry to a fan-beam setup permitted the investigation of 2D coherent scatter data acquisition in a more relevant CT geometry.

Figure III.1 illustrates the simulated scatter pattern generated from a 32 kVp molybdenum spectrum x-ray beam impinging on 1 cm thick sample of water. The fan-beam produced the scatter line pattern in Figure III.1(b), which is essentially composed of individual pencil-beams annular scatter patterns, where the annular scatter patterns are reenforced to form the peak scatter lines above and below the fan-beam plane. Without post-scatter collimators, it is difficult to determine the location from which a scatter event occurred. Post-scatter collimators restrict the scatter in object space, which permits the reconstruction method described in Chapter I to be used.

All current multi-slice CT scanners use an area-wide detector along with an area-wide-beam source, see figure III.2(a). Source collimators are adjusted in the z-direction (along the bore-axis direction) to permit the acquisition of a variable number

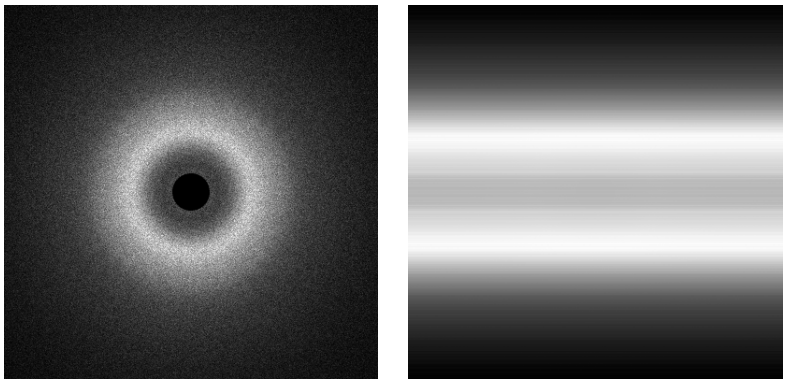

(a) Mo 32 kVp pencil-beam simulated scatter pattern produced from 1 cm of water.

(b) Mo 32 kVp fan-beam simulated scatter pattern produced from 1 cm of water with no post-scatter collimators. The intensity of the scatter between the principle line peaks is due to lateral scatter. Post-scatter collimators eliminate this phenomenon.

Figure III.1: Pencil and fan-beam scatter patterns

of transaxial-slices during a single rotation of the x-tube. By collimating the x-ray area-wide beam in the z-direction into a thin fan-beam, a multi-slice scanner can be made to mimic the acquisition geometry of a single-slice CT scanner. In this geometry, with an area-wide detector, the detection of photons scattered out of the thin fan-beam plane is possible. Currently, all clinical CT scanners reject photons detected outside the specified slice width. In principle, area-wide detector elements located above and below the fan-beam plane could be used to detect scattered photons for use in CSCT image reconstruction, see figure III.2(b). This chapter explores this possibility through EGS5 simulations.

Method

The segmented fan beam simulation geometry described in this section is also the same setup used for the experiments in Chapter IV with a few minor exceptions, which are noted in the next chapter. One of the most import differences between the

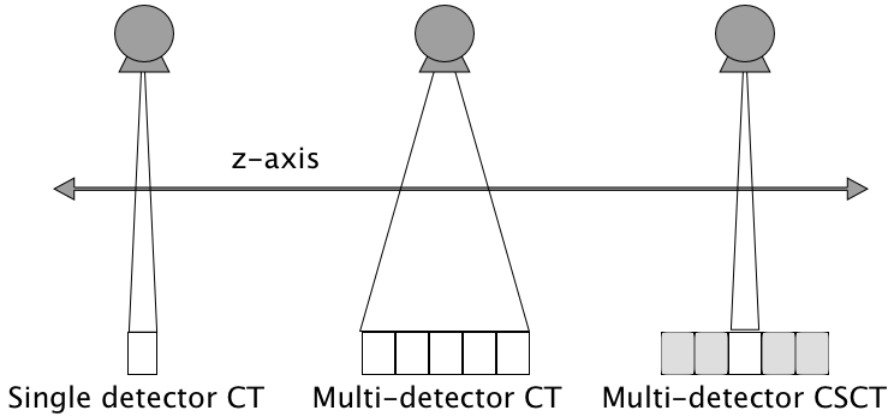

(a) Side view of fan-beam plane: source and detector geometry for three CT systems. Gray detector elements in the CSCT geometry detect out-of-fan-beam-plane scatter.

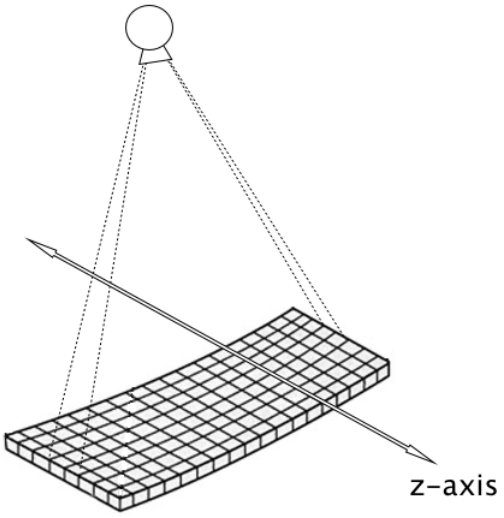

Multi-detector CSCT

(b) Oblique view of fan-beam CSCT geometry sans post-scatter collimators, which prevent lateral scatter detection.

Figure III.2: Multi-element detector configuration

experiments in this chapter and the next is the difference in heterogeneous phantoms used. This chapter used a 3-material phantom, while Chapter IV used a 4-material phantom.

A total of three different phantoms were utilized in this chapter:

1. 10-cm diameter, heterogeneous, cylindrical phantom, labeled phantom#1.
2. 10-cm diameter, homogeneous, cylindrical phantom composed of beef fat.
3. 5-cm diameter cylinder composed of muscle.

Heterogeneous Phantom #1

Phantom #1 was composed of beef fat with two embedded 3.75 cm diameter cylinders, one composed of beef muscle and the other with air, figure III.3.

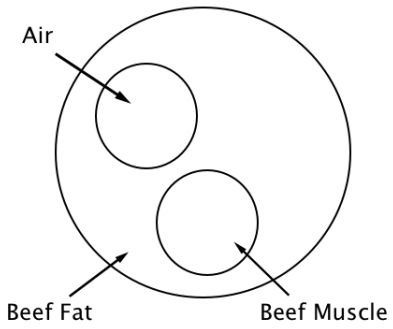

Figure III.3: Phantom #1; 10 cm outer diameter.

The materials in this phantom were selected due their distinct scattering properties, which allowed separation of the material scatter peaks. Fat scattered at a lower angle than muscle, which allowed for identification of the material based on scatter angle. The results section contains an illustration of this property that will make this more clear. Table III.1 lists the composition of the materials used.

Table III.1: EGS5 material composition. Tissue mixture compositions match ICRU 46 Appendix A table A.1 elemental composition for adult tissues. Beef Kidney material is used in Chapter IV.

	Elemental composition (mass fraction)											density
Materials	H	C	N	O	Na	P	S	Cl	K	Ca	Ar	(g/cm^3)
Beef Fat	0.114	0.598	0.007	0.278	0.001		0.001	0.001				0.95
Beef Muscle	0.102	0.143	0.034	0.710	0.001	0.002	0.003	0.001	0.004			1.05
Beef Kidney	0.103	0.132	0.030	0.742	0.002	0.002	0.002	0.002	0.002	0.001		1.05
Air at NTP			0.75575	0.23143							0.01282	1.205×10^{-3}

Segmented Fan Beam Geometry

Multiple simulated fan-beam geometry experiments were performed to investigate the affects on CSCT image quality due to three principle variables (scatter material, photon energy, and number of photons). Several CSCT images were generated for various monoenergetic beams for phantom #1, a 10-cm diameter phantom. Filtered back projection (FBP) was used to reconstruct all CSCT images.

EGS5 was used to generate scatter projections from four mono-energetic beams (30, 50, 70, and 90 keV) for a 10-cm diameter cylindrical phantom composed of fat enclosing two off-axis 3.75 cm diameter cylinders (one of muscle and the other of air)[33]. The axes of the muscle and air cylinders are parallel to the axis of the fat cylinder. The central axis of the phantom was positioned 30 cm from the x-ray source and 30 cm from a cylindrical detection arc composed of Se (figure III.4(a)).

For the fan-beam geometry, the x-ray source had a vertical FWHM Gaussian intensity distribution of 3.4 mm. The peak intensity of the source was coplanar with the center of the semi-cylindrical detector array (dotted line in figure III.4(b)). The detection plane consists of a 175 x 577 (row, column) array of $1mm^2$ photon-integrating elements with 100% detection efficiency, positioned on a 55° cylindrical arc at a distance of 60 cm from the source.

The fan-beam geometry was simulated by re-directing the beam toward each of the detector columns along the 55-degree arc. The manner in which the simulation was executed effectively simulated post-scatter collimation slits oriented parallel to the axis of the cylindrical phantom and separating each vertical column of the detector array (figure III.5).

Performing the simulation in this manner allowed for simpler coding of the geometry by reducing the number of objects to code for (i.e., collimator vanes and other detection elements) and also reduced the amount of memory and time necessary to run simulations.

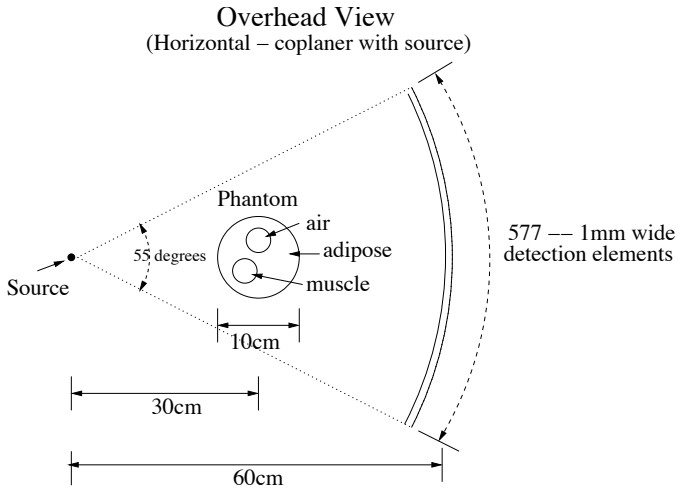

(a) Overhead view of simulation geometry (not to scale); source is coplanar with 577 central detection elements as shown in figures III.4(b) and III.5.

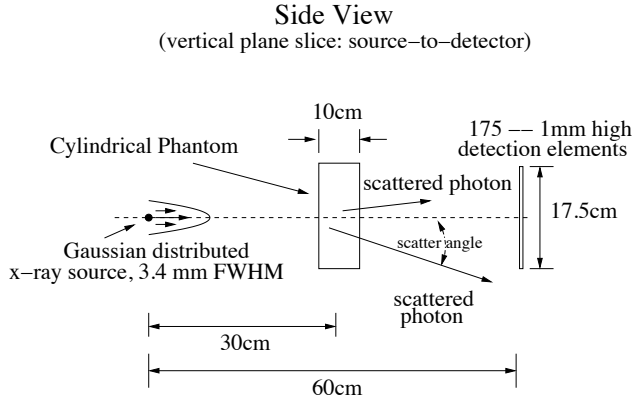

(b) Side (vertical plane) view of simulation geometry (not to scale); one of 221 simulation runs per angular sample.

Figure III.4: Fan-beam geometry

Specifically, the simulation partitioned a fan beam setup into individually separate vertical spatial segments. Photon transport only occurred within a rectangular space with dimensions 1 mm wide x 175 mm high x 700 mm long. The transport space included the source as it swept through the phantom and intersected the detection plane, see figure III.5. Photons were only transported if they remained in this defined volume. Unlike a full-fan beam geometry with an associated area-wide detector and no post-scatter detector collimators, the restricted transport space ensured that the individual detector columns recorded only scatter from the object within the transport

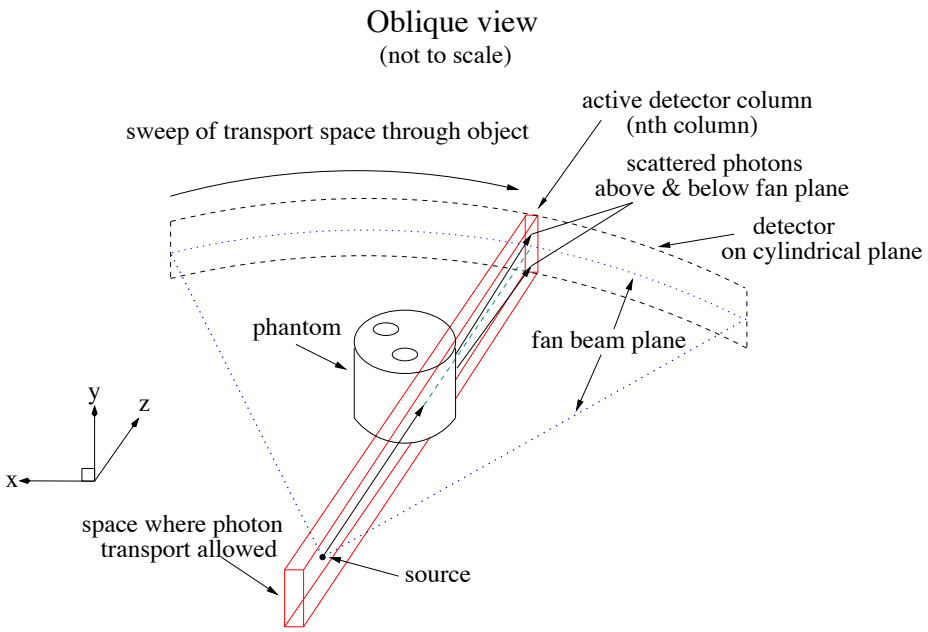

Figure III.5: Oblique view of simulation geometry (not to scale); source is coplanar with 577 central detection elements. The photon transport space is defined as a rectangular space with dimensions 1 mm wide x 175 mm high x 700 mm long. This corresponds to dimensions of a single detection column and the distance from the source to the detector elements plus 10 cm.

region and no lateral scatter by other portions of the object located outside this region. When the data from the individual detector columns are combined into a single 2D data set, the setup essentially mimics a full fan beam source with perfect post-scatter lateral collimation.

The range of scatter angle acceptance at a particular detector element from an extended object is greatest for those elements located at the top and bottom of the detector array (± 8.75 cm above the central detector plane, which corresponds to a scatter angle of $\pm 16.1^\circ$ relative to the center of the object). At those locations, scatter from a 10-cm diameter cylindrical object with its center located 30 cm from the detector results in a maximum of $\pm 5.2^\circ$ of scatter angle acceptance; at a scatter angle of $\pm 6^\circ$ the range of scatter angle acceptance is only $\pm 2^\circ$. In contrast, the range of the lateral scatter angular acceptance for each detector element is approximately $\pm 0.3^\circ$.

Processing Details

The EGS5 simulations were performed on a Dell (Dell, Inc., Round Rock, TX) n-series high performance workstation utilizing a dual quad-core Xeon x5560 (2.8GHz) processor. Each individual simulation segment, mentioned previously, is a run. Each run simulated 10^7 photons and took approximately 12 minutes. The low energy photon transport cutoff was 3 keV. The phantom was sampled at 5.54° intervals for 360 degrees (65 angles). Thus, a total of 650 million photons were used to interrogate a section of the phantom with only about 2.4% to 3.6% of the photons utilized for coherent scatter tomogram reconstruction. Each angular sample consisted of 221 runs where the detector elements recorded scatter from the phantom plus approximately ten detector columns on either side of the phantom in the air-filled space for a total of 14365 runs per data set. Initially, one complete data set took approximately 14 days to simulate. No alteration of the EGS5 source code was attempted in order to optimize the run time. Later on it was discovered that an approximately 70% reduction in simulation time resulted if a separate dedicated binning program was used to histogram photon counts outside of the EGS5 simulation. This aspect greatly facilitated data acquisition and, thus, permitted more sample angles to be obtained for the follow-on simulations that used phantom #2.

Image Reconstruction

Since each simulated data set contained both attenuation and scatter information, both traditional attenuation-based CT and multiple CSCT images were reconstructed from a single acquisition. Each sampling section along the vertical direction on the detector plane corresponded to a different scatter angle. Data from a selected range of scatter angles was used to create a sinogram, which was then reconstructed into a CSCT image. The general assumptions and formalism covered in Chapter I permitted the detected scatter signal to be interpreted as being proportional to the sum of

scattering centers which scattered photons into a particular detection element. As mentioned in Chapter I, the formula describing the photon scatter (equation I.12) integrated over the length of the scattering object possesses the same form as the line integral of the linear attenuation coefficient from a measured projection used in conventional FBP CT image reconstruction, with the exception that the attenuation coefficients are replaced by the quantity $\gamma[l, x]$, the differential linear coherent-scatter coefficient. From the simulated data, coherent scatter and conventional attenuation images were reconstructed into 220x220 pixel images utilizing a java FBP code run through ImageJ. This FBP method performed a spatial convolution as the filtering operation with a kernel size of 65x65 with a standard Hamming window.

Results

The results section is divided into essentially two portions based on which phantom was used in a simulation. Simulations that utilized the two homogeneous phantoms were for illustrating the difference in material scatter angle through scatter profile plots, while the those utilizing the heterogeneous phantom, phantom #1, were used to generate CSCT images where the image contrast was derived from the number of detected scattered photons.

Homogeneous phantoms: Scatter Profiles

The simulated fan-beam geometry illustrated in figures III.4 and III.5 was used to collect simulated out-of-plane scattered photons from a homogeneous cylinder of fat (figure III.6 top row) and muscle (figure III.6 bottom row) as a function of energy (30, 50, 70, and 90 keV). The unscattered photons in the fan-beam plane were removed by means of the simulated beam-stop located in the plane of the fan-beam. By segmenting the fan-beam and limiting the detector to a thin vertical section (see figure III.5), a "virtual" ideal post-scatter collimator is simulated. Lateral scatter

contributions would result if the object was illuminated with a full fan beam and had no post-scatter collimator.

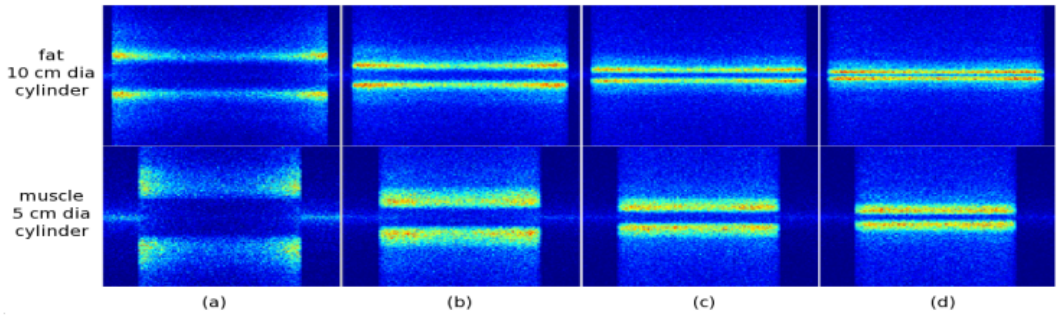

Figure III.6: EGS5 simulated scatter patterns produced by four separate monoenergetic x-ray beams incident upon two different homogeneous cylindrical phantoms for the geometry illustrated in figures III.4 and III.5. Top row: 10 cm diameter of simulated adipose tissue; bottom: 5 cm diameter of simulated muscle tissue. (a) 30 keV, (b) 50 keV, (c) 70 keV, and (d) 90 keV. Primary photons within the source plane have been removed to reduce the display dynamic range in order to visually enhance the scatter out of the source plane .

The images of figure III.6 represent one angular projection of the cylindrical phantom (one of 65 - 5.54° samplings). The corresponding plots of scattered x-ray intensity versus scatter angle for each x-ray energy used are shown in figure III.7. As illustrated, the location of peak scatter intensities shown in figure III.7 are strongly dependent upon beam energy; the peak intensity scatter angle is reflected in the distance of vertical displacement from the source plane.

To illustrate the selection of a particular scatter angle for maximizing image contrast, figure III.8 presents the superposition of scatter profiles for both fat and muscle for beam energies of 30 keV, 50 keV, 70 keV, and 90 keV. As an example, in the 50 keV graph a scatter angle of approximately 3° produces a maximum of scatter from fat and a corresponding minimum amount of scatter from muscle.

Heterogeneous phantom: CSCT Image Contrast

For scatter from heterogeneous phantom #1, traditional FBP CT image reconstruction was used to create the tomograms. As noted previously, angular projection

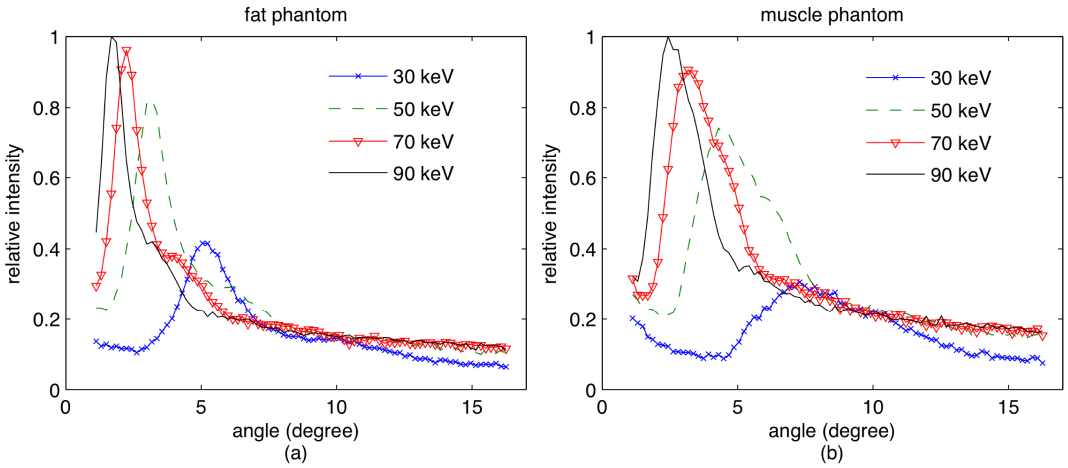

Figure III.7: Simulated scatter profiles produced from a homogeneous (a) 10 cm diameter cylindrical phantom of fat and (b) a 5 cm diameter cylinder phantom of muscle obtained in the fan-beam geometry at 30 keV, 50 keV, 70 keV, and 90 keV.

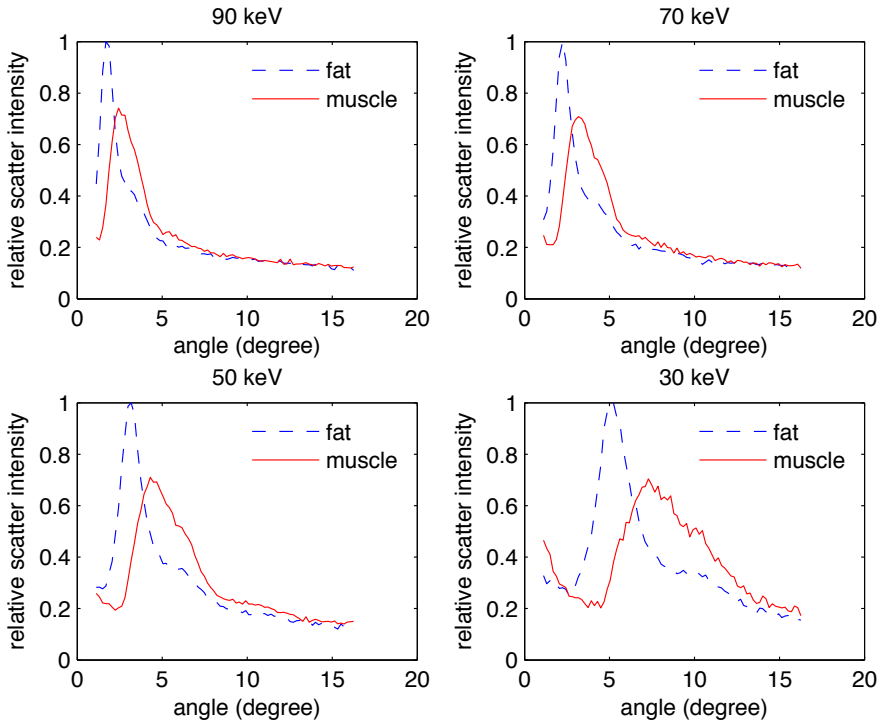

Figure III.8: Comparison of simulated scatter profiles of photon scatter from separate homogeneous fat and muscle cylindrical phantoms at 30 keV, 50 keV, 70 keV, and 90 keV.

profiles from each scatter angle (vertical detector location) can be used to reconstruct a separate transverse image of scattering sites within the plane of the x-ray beam that contributed to a particular scatter angle. Figure III.9 presents the sinogram and corresponding FBP reconstructed images produced from a complete 360-degree set of scatter profiles taken at four different beam energies, 30, 50, 70, and 90 keV, of phantom #1.

FBP images were reconstructed using both the attenuation data (figure III.9, column (a)) from detectors located on the central axis and from the coherent-scatter data for three different scatter angles. In figure III.9, columns (b) through (d) contain CSCT images produced from sinograms derived from summed scatter into a region of the detector array that subtended 2.5°, 2.5°, and 3.9° of arc centered on a scatter angle of 2.3°, 5.0°, and 9.8°, respectively, see figure III.10). These windows were selected because they fully include the peak scatter signal at 50 and 90 keV, and partially at 70 keV. The 3.9° wide window at 9.8° degrees captures the fat signal for 30 keV along with the trailing scatter tails from the other energies.

Table III.2 illustrates how image contrast between muscle and fat is modulated by the selection of beam energy and scatter angle. The contrast was calculated as $contrast = (mean(muscle) - mean(fat))/mean(fat)$, where $mean(x)$ is the average pixel value for material x in a 400 pixel circular area. As an example of contrast modulation, note that at 70 keV, when images are reconstructed from the 5.0° scatter angle, the contrast between muscle and fat is roughly twice the contrast of the conventional attenuation-based CT image (see figure III.9). Thus, the contrast between any two tissues types may be enhanced by the appropriate selection of scatter angles.

Discussion

Figure III.9 illustrates how selecting different scatter angles can be used to manipulate component image contrast (see table III.2). Specifically, in column (b) of figure

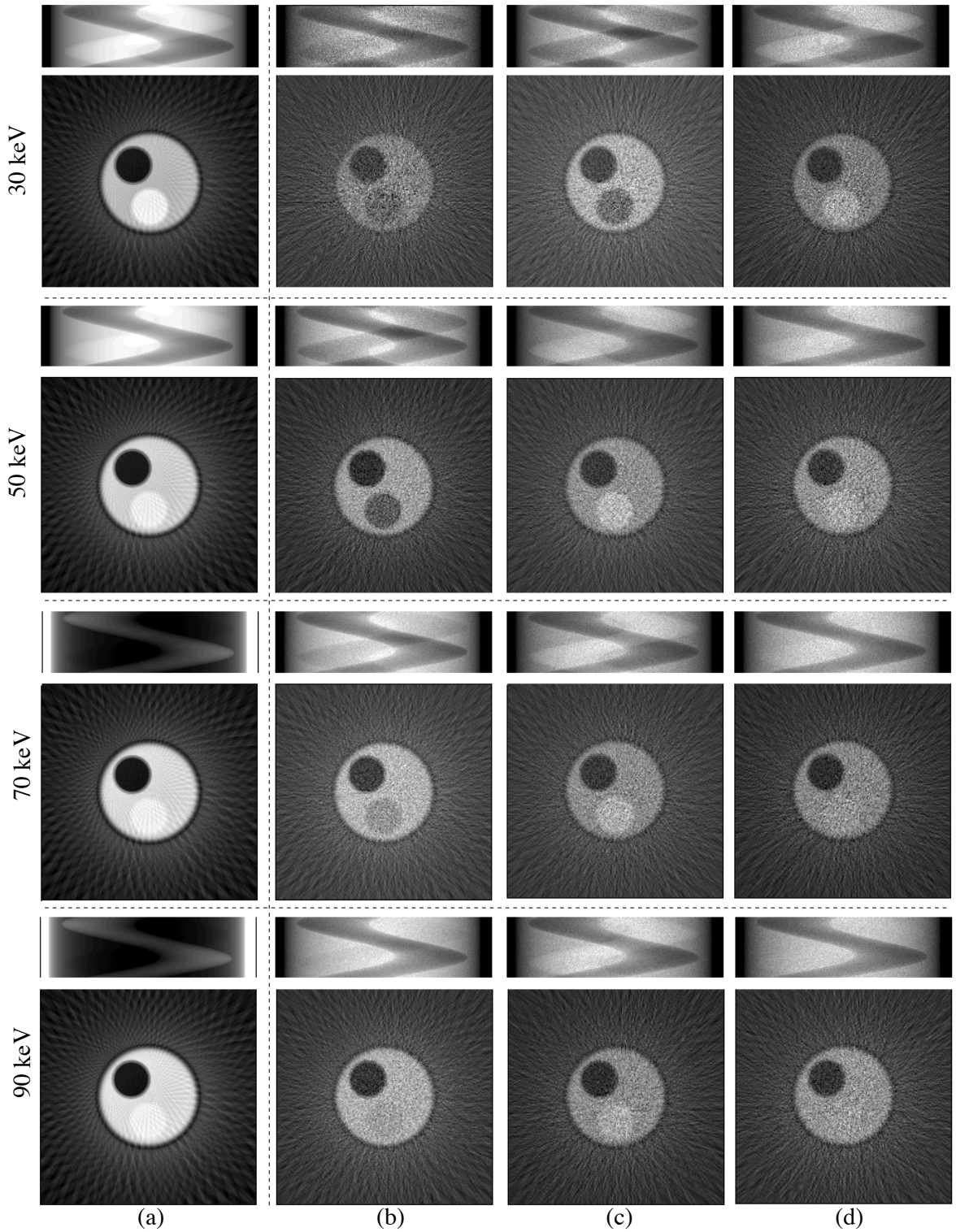

Figure III.9: FBP reconstruction of object from simulated scatter data for 30keV, 50keV, 70 keV, and 90 keV x-ray beams. Column (a) is attenuation only data (traditional CT), remaining columns are CSCT images produced from coherent scatter at angles: (b) 2.3°, (c) 5.0°, and (d) 9.8°. Sinograms used for each reconstruction are positioned directly above each tomogram. See figure III.3 for phantom diagram.

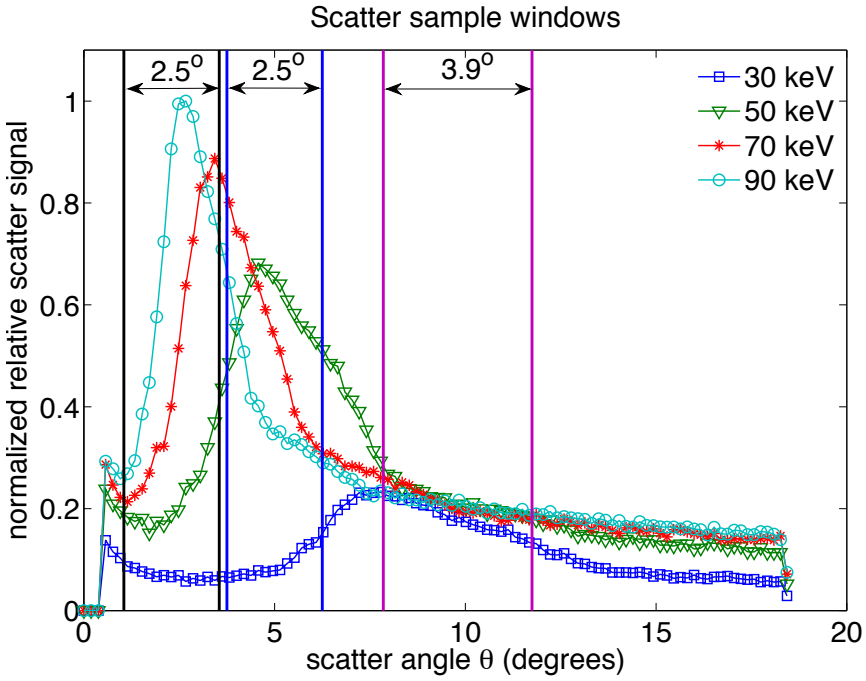

Figure III.10: Sampling scatter windows relative position to scatter profiles.

Table III.2: Muscle-to-fat contrast

Energy	Scatter angle			
(keV)	0 °	2.3 °	5.0 °	9.8 °
30	0.301	-0.192	-0.353	0.317
50	0.149	-0.424	0.269	0.151
70	0.097	-0.179	0.249	0.097
90	0.096	-0.088	0.191	0.047

III.9, we see that muscle has a lower scatter intensity relative to the surrounding fat. With the exception of the 30 keV images, at 5° the muscle is now depicted with a greater scatter intensity; at 9.8° the contrast between muscle and fat is essentially eliminated for 70 and 90 keV images. The reason for this is seen by referring back to figure III.8, where at 5° muscle is the main scatter contributor at that angle for all energies except 30 keV. In figure III.8 at 30 keV, muscle peaks around 7.5° and fat at less than 5°; therefore, scatter from muscle contributes more at higher scatter angles than does fat, see figure III.9 column (d), which shows more pronounced contrast for the 30 keV high-angle scatter image than for the other energies. Thus, the image intensity of a CSCT image reveals the material that contributed the most to photon scattering at a particular angle and energy. Table III.2 shows that the muscle-to-fat contrast for images produced from 2.3° of scatter data is greater than the conventional CT reconstructed images for all energies used. The greatest contrast difference is seen in the 30 keV reconstructed image produced from 5° scatter data.

Relative to conventional attenuation-based CT images, this simulation demonstrates that CSCT images reconstructed from scattered photons may be able to modulate image contrast and provide additional information about soft-tissue composition. Such composition images extend the potential uses for CT imaging into the realm of investigation of tissue properties that could have a significant impact on diagnostic procedures involving subtle tissue differences, evaluation of treatment regimens, and automatic image segmentation, which may be assisted by the varying amounts of relative contrast seen in images produced from different scattering angles.

Simulations are essential for parameter space studies, and can be used to evaluate and optimize system parameters before moving to hardware implementation. EGS5 can be extended to investigate CSCT with a poly-energetic x-ray beam energy spectrum. Poly-energetic simulations are of particular importance due to the known bandwidth effect on angular broadening of coherent scatter patterns. Future simulations may investigate coherent scatter produced from other medically relevant

material in various positions, optimal system geometries, the dependence of absorbed radiation dose on image noise, and reconstruction of material-specific images by using the basis function analysis method described by Westmore[60]. Since the coherent scatter dominates incoherent scatter at low x-ray energies and in low-Z materials, CSCT may have the potential to allow differentiation of tissues of different molecular composition but with similar physical density and/or similar effective Z, relative to conventional attenuation-based x-ray computed tomography.

Conclusion

EGS5 potentially allows one to simulate geometries and materials in order to assist in the design of a dedicated CSCT system for improved detection of a selected material and/or tissue. The segmented fan-beam geometry used in this chapter demonstrated a basic acquisition setup for gathering scatter data for producing CSCT images. The experiments illustrated how the photon scatter angle is dependent on the material and incoming energy of the photon, and how this manifests itself as different scatter profiles, which can be used to generate contrast in CSCT images.

CHAPTER IV

EGS5 CSCT SIMULATIONS: PART II

Introduction

The experiments in this chapter continued the use of the discrete fan-beam CSCT acquisition geometry developed in the pervious chapter. A wider range of monoenergic beams and polyenergetic spectra are used, and a more expansive set of image metrics are measured and analyzed in order to explore how different materials and energy spectra affect CSCT image quality. The 3-material cylindrical phantom has been expanded into a 4-material phantom containing water, beef fat, beef muscle, and beef kidney. These materials were selected as they are medically relevant tissues, and, for muscle and kidney, create scatter profiles similar to that of water since they are composed primarily of water. The amount to which fat and the water based tissues can be distinguished in CSCT images is dependent upon the their scattering properties, as the pervious chapter demonstrated. However, the amount to which similar-Z and similar density material can be distinguished from each other is investigated in this chapter.

In addition to acquiring a larger set of imaging metrics, an estimate of the dose deposited to the various regions of the 4-material phantom was recorded. For the polyenergetic CSCT acquisitions an attempt was made to associate the simulated beam parameters used with clinical CT scanner techniques. This was accomplished by relating $CTDI_{100}$ measurements obtained from a clinical scanner using a pencil-beam ionization chamber and a 10 cm cylindrical acrylic phantom with those obtained from associated simulations, and by matching the simulated polyenergetic spectra to the spectra of the clinical CT scanner.

Method

Since the experimental methods in this chapter are similar to those in Chapter III, only the differences in the simulations and processing parameters will be noted in this section. These differences include the following:

- 4-material (phantom #2) vs. 3-material phantom (phantom #1).
- Total detector vertical dimension height was 20 cm vs. 17.5 cm (see figure III.4).
- Photon vertical scatter sample angles: $1.7°, 3.0°, 5.0°, 7.4°$, and $9.8°$ vs. $2.3°, 5.0°$, and $9.8°$; this permitted sampling both sides of the main scatter peak and an additional intermediate scatter angle.
- 65 sample angles ($5.54°$ sampling interval) for energies 30, 50, 70, and 90 keV - same as previous chapter's experiments.
- 128 sample angles ($2.81°$ sampling interval) for energies 45, 60, 75, and 85 keV - different from previous chapter's experiments.
- 128 sample angles for polyenergetic spectra.
- Polyenergetic spectra: Tungsten 80, 120, 140 kVp with 6.3, 10.6, and 15.5 mm of Al filtration, respectively.
- Images were reconstructed using a MATLAB© FBP function with a Hamming window in the frequency domain vs. ImageJ[45] with filtering in the spatial domain.
- CSCT images were reconstructed into 221x221 image arrays with pixel dimensions of ∼0.5 mm x ∼0.5 mm vs. 220x220 and ∼1.0 mm x ∼1.0 mm for phantom #1 CSCT images.
- Additional dose deposition data was acquired.

Many of the changes were implemented as greater experience with processing larger data sets was gained. Increasing the number view angles to 128 aided in reducing the angular sampling reconstruction artifact in FBP. Utilizing MATLAB© provides a

widely available reconstruction tool that other investigators can use to recreate CSCT images similar to the ones in this chapter, unlike the custom written java class FBP used with ImageJ in Chapter III.

Heterogeneous Phantom #2

Phantom #2 was composed of a 10 cm diameter water cylinder with three embedded 3.75 cm diameter cylinders, each individually composed of beef fat, beef muscle, and beef kidney, figure IV.1.

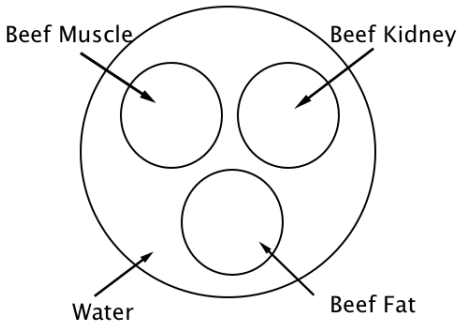

Figure IV.1: Phantom #2

As mentioned in the introduction, these materials were selected because they are medically relevant tissues, and two of the tissues, muscle and kidney, are composed primarily of water. In this phantom, differences in the scattering properties between similar (e.g., water & muscle) and dissimilar (e.g., water & fat) materials can be evaluated in the reconstructed CSCT images. The material compositions are listed in table III.1 located in Chapter III.

Image Metrics: Contast, CNR, and SNR

For all reconstructed mono- and polyenergetic CSCT images, a common set of measurements were taken with the same size ROI and at the same locations in each

image. The circular ROI measured $\sim$ 1200 square pixels. The calculated quantities were SNR, CNR, and contrast. The image contrast was relative to the water background. The equations used to calculate the metrics were:

$$\begin{aligned} \text{SNR} &= \text{mean}(\text{ROI}_{\text{material}})/\text{stdev}(\text{ROI}_{\text{material}}), && \text{(IV.1)} \\ \text{CNR} &= [\text{mean}(\text{ROI}_{\text{material}}) - \text{mean}(\text{ROI}_{\text{water}})]/\text{stdev}(\text{ROI}_{\text{water}}), && \text{(IV.2)} \\ \text{contrast} &= [\text{mean}(\text{ROI}_{\text{material}}) - \text{mean}(\text{ROI}_{\text{water}})]/\text{mean}(\text{ROI}_{\text{water}}). && \text{(IV.3)} \end{aligned}$$

Reconstructed images were created by performing FBP on the input scatter sinograms. Scatter sinograms were generated by accumulating forward-vertically scattered photons at 1.7°, 3.0°, 5.0°, 7.4°, and 9.8° with an associated angular sampling range of 1.14, 1.14, 2.50, 1.87, and 2.59 degrees, respectively.

Monoenergetic Beams

Monoenergetic beam simulations for this chapter can be divided into two major data sets: those performed with 65 sampling angles, and those performed with 128 sampling angles. All mono energetic beams are within the clinical diagnostic x-ray energy range.

The 65 sample angle simulations encompassed four photon energies (30, 50, 70, and 90 keV), and two source photon amounts, a $\times 1$ and a $\times 10$ ($\times 1 = 1.4 \times 10^{10}$ photons per CSCT image acquisition). The angular sampling interval was selected for continuity purposes with the data taken in Chapter III. The two different photon source amounts were used to examine the SNR and CNR of the CSCT images.

The 128 sample angle simulations encompassed four photon energies (45, 60, 75, and 85 keV), each used 2.8×10^{11} photons per CSCT image acquisition. An increase in the sampling interval was used to reduce FBP artifacts relative to the 65 sampling interval data set, and also to illustrate how an increased number of total photons per CSCT data set affects CSCT image SNR and CNR.

Polyenergetic Beams

W 80, W 120, W 140 kVp

Three tungsten polyenergetic data set (80, 120, 140 kVp) were processed in an identical manner as the mono energetic data sets. The polyenergetic spectra used for the simulations are displayed in figure IV.2.

For each of the three polyenergetic beam simulations, the phantom was sampled over 128 sample angles, and each spectra had three different source photon fluxes: $\times 1$, $\times 10$, and $\times 100$. Table IV.17 in the results/dose section lists the number of photons used for the simulations for each energy.

The base $\times 1$ source photon flux for each energy (80, 120, 140 kVp) was different due to the manner in which the spectra were normalized. Each spectrum was self-normalized to the spectrum maximum and then multiplied by a constant to create a scaled distribution of the original spectrum. The integral of the adjusted distribution equaled the number of photon used for a particular simulation.

The x-ray spectra were produced utilizing the tungsten anode spectral model using interpolating polynomials (TASMIP)[5]. This method is similar to the previously mentioned MASMIP[4] method that was used to generate the molybdenum spectrum used for the simulations in Chapter II. To quote the authors Boone and Seibert:

> TASMIP is not semi-empirical and uses no physical assumptions regarding x-ray production, but rather interpolates measured constant potential x-ray spectra published by Fewell et al. [Handbook of Computed Tomography X-ray Spectra (U.S. Government Printing Office, Washington, D.C., 1981)].

The energy increment for the tungsten spectra was 1 eV, whereas the molybdenum energy increment was 0.5 eV used in Chapter II. A larger energy increment was used for tungsten due to the larger energy range covered by W-spectra.

In order to use the TASMIP technique, an appropriate beam filtration had to be chosen. For selecting the appropriate beam filtration, half value layer (HVL)

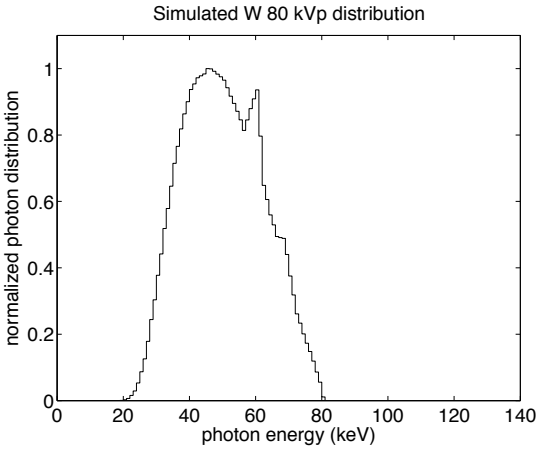

(a) W80 kVp

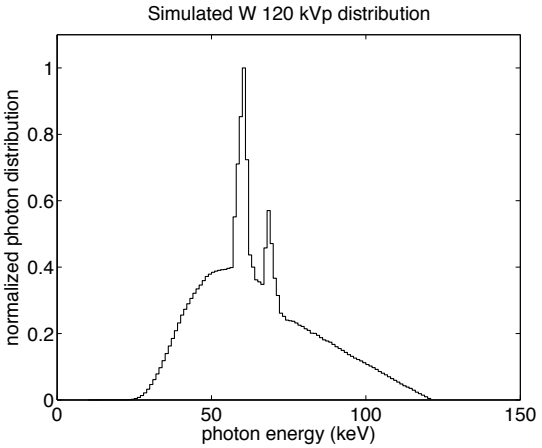

(b) W120 kVp

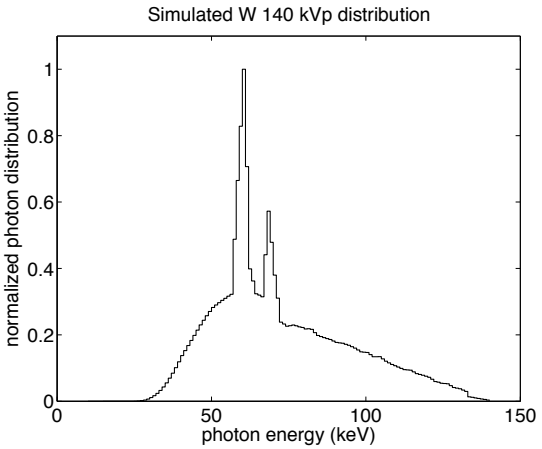

(c) W140 kVp

Figure IV.2: Simulated energy spectra.

measurements for a clinical CT scanner (Philips Brilliance 16) were determined at 80, 120, and 140 kVp. The CT tube was positioned at the bottom of the gantry (180° location), with the detector positioned at the gantry isocenter. A RTI Barracuda x-ray multimeter[48] with a multipurpose detector (MPD) was used for the exposure measurements. The CT was operated in scan mode, which held the tube stationary at the 180° location. The source was collimated to 40 mm in the z-direction, and the z-table movement was minimized to ensure that the detector sensitive area was exposed to the x-ray field. Various thickness of aluminum were placed on the gantry near the tube collimators, and exposure measurements recorded in order to determine the quality of the beam at a particular kVp.

After determining the HVL for 80, 120, and 140 kVp, simulations of TASMIP generated spectra with differing amounts of filtration for the three kVp energies were conducted. A simulated beam attenuation experiment was performed on the generated spectra to determine the associated HVL for each spectra. Filtration for a particular simulated kVp spectrum was adjusted until its calculated HVL matched that of the Philips scanner for the associated kVp setting. From the HVL measurements, the effective energy of each spectra was interpolated from a NIST table of Al HVL vs. photon energy. Table IV.1 contains the details for the polyenergetic spectra used in the CSCT simulations. One of the motivations for matching the beam quality in the simulation to an actual clinical scanner was to facilitate a number-of-photons-to-mAs comparison between the two experimental environments through $CTDI_{100}$ measurements.

Table IV.1: Polyenergetic spectra characteristics for the simulations.

Energy (kVp)	Eff. Energy (keV)	Filtration (mm of Al)	HVL (mm of Al)
80	46	6.3	6.1
120	60	10.5	9.0
140	66	15.5	10.3

Mo 32 kVp

The same experimental setup used for the tungsten spectra was repeated for a single molybdenum spectrum, minus the $CTDI_{100}$ aspect and HVL determination. Two separate runs were performed, with one run utilizing $\times 10$ the number of photons than the other. Figure IV.3 shows energy molybdenum spectrum, which was generated utilizing the MASMIP[4] method, and is identical to the spectra used in Chapter II to verify EGS5's ability to model coherent scatter.

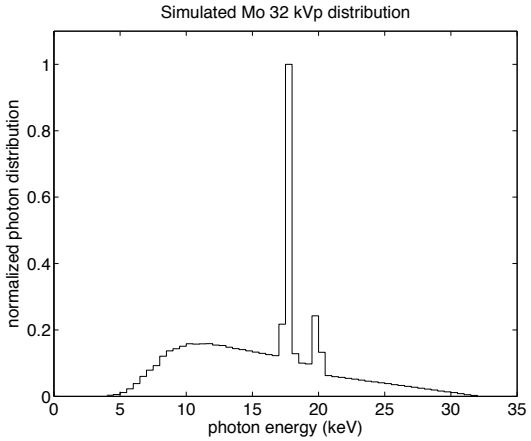

Figure IV.3: Simulated energy spectrum (32 kVp Mo). Same as figure II.2(a).

$CTDI_{100}$

In order to relate the polyenergetic simulation techniques (kVp, beam width, number of sampling angles, and number of photons) to clinical scanner techniques (kVp, mAs, collimator width), a Computed Tomography Dose Index 100 ($CTDI_{100}$) comparison was performed. Beam width and collimator width both refer to the total x-ray beam incident upon an object at the CT isocenter. Appendix C contains additional information regarding $CTDI_{100}$.

A 10 cm diameter, cylindrical acrylic phantom (CIRS Model 007A - see figure IV.4) used for clinical pediatric head CTDI measurements was used since it was the same diameter as the two simulated material phantoms mentioned previously.

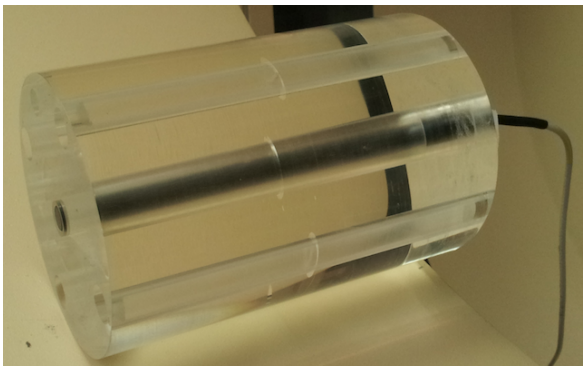

Figure IV.4: 10 cm diameter CIRS model 007A phantom with Exradian A101 pencil ionization chamber.

This acrylic phantom was 100 cm in length, and contained five 1.3 cm diameter holes, four located at the cardinal angles and one located in the center of the phantom. Each hole was designed to accommodate a standard Exradian A101 100 cm long CT pencil beam ionization chamber. The ion chamber was placed in the central hole of the acrylic phantom and the entire ensemble centered in the bore of the clinical scanner with the ion chamber at the CT isocenter. Exposure measurements from a single 360° tube rotation were then measured for a 7.5 mm collimator width (12x0.625 mm detector setting on the scanner). Clinical scanner $CTDI_{100}$ measurements for a 7.5 mm collimator width were obtained for 80, 120, and 140 kVp, see table IV.19 in the Results section. Associated simulations utilizing the TASMIP generated spectra on a simulated 10 cm diameter, cylindrical acrylic phantom were performed to determine the simulation's $CTDI_{100}$ for a 7.5 mm collimator width. Simulated and experimental $CTDI_{100}$ measurements were then used to estimate the clinical technique that corresponded to the simulated technique used.

Dose

Separate from the $CTDI_{100}$ measurements comparison, all the mono- and polyenergetic simulations performed on phantom #2 had energy deposition recorded for the various materials. Since the density of the materials in the phantom were known, and

the sampling slice thickness was taken to be equivalent, the nominal x-ray beam width of 3.4 mm FWHM, an estimate of the dose deposited to the various materials was calculated. This was done in order to relate the imaging metrics of the reconstructed CSCT images of phantom #2 to the number of photons used and dose deposited to the phantom. Tables IV.14 - IV.17 contain the dose measurements and are located in the results section.

Results

Phantom #2 monoenergetic beam experiments can be divided into two sets: those performed with 65 sampling angles (30, 50, 70, and 90 keV) and those conducted with 128 sampling angles (45, 60, 75, and 85 keV). The 30, 50, 70, and 90 keV experiments can be further divided into two more sets with one set using $\times 10$ more source photons than the other.

Two separate sets of sampling angles were used to illustrate the improvement in the reconstructed CSCT image quality with increased sample angles. Imaging metrics and the deposited dose all increased with an increase in the number of photons used whether by increasing the number of sampling angles or just increasing the source output. Two separate source photon fluxes were used to illustrate the image quality improvement with increased number of detected photons.

The polyenergetic experiments include three different source energy spectra and three different photon fluxes, with all simulations performed over 128 sample angles. These parameters were adjusted to illustrate that the same effects occur for polyenergetic sources as they did for the monoenergetic sources.

30, 50, 70, 90 keV; 65 Views; x1, x10

For the 30, 50 ,70, 90 keV simulations, two sets of experiments were conducted with one set utilizing $\times 10$ more source photons that the other.

Figure IV.5 illustrates the FBP reconstructed CSCT images of phantom #2 for 30, 50, 70, and 90 keV and 65 samples angles. A total of 1.4×10^{10} photons were used for each image acquisition. Figure IV.6 illustrates the FBP reconstructed CSCT images of phantom #2 for 30, 50, 70, and 90 keV and 65 samples angles. A total of 1.4×10^{11} photons were used for each image acquisition.

Contrast

A comparison of figure IV.5 to figure IV.6 reveals that the material regions were easier to discern in figure IV.6 due to the reduced noise in those images, as expected. For the 0° (attenuation-based) images, both the ×1 and ×10 case showed that the contrast measurements between the insert material regions and the water background were identical, see table IV.2, but fluctuated for the CSCT images, see figure IV.7. The image noise appeared to give rise to fluctuations in contrast measurements, which was seen primarily at lower scatter angles and lower energies. The ×10 measurements in table IV.2 were within one standard deviation of the ×1 measurements if it was assumed that the contrast measurements followed Poisson statistics, which was not an unreasonable assumptions since the signal was derived from the number of photons detected.

Also in figure IV.6 for the attenuation-based images, we see that the contrast for each material region (fat, muscle, kidney) relative to the surrounding water is highest for the lowest energy, 30 keV, and lowest for the highest energy, 90 keV, These values are quantified in table IV.2 for the ×10 source photon flux case. At 0°, the fat contrast relative to water is negative indicating that the pixel values for water are greater than those for fat; for the muscle and kidney regions the situation is reversed. The pixel intensities at this angle correspond to the attenuation properties of the material at that location within the object.

As we look at the scatter generated tomographs, we see that there is an inversion of the material contrast that occurs at scatter angles beyond the peak fat contrast

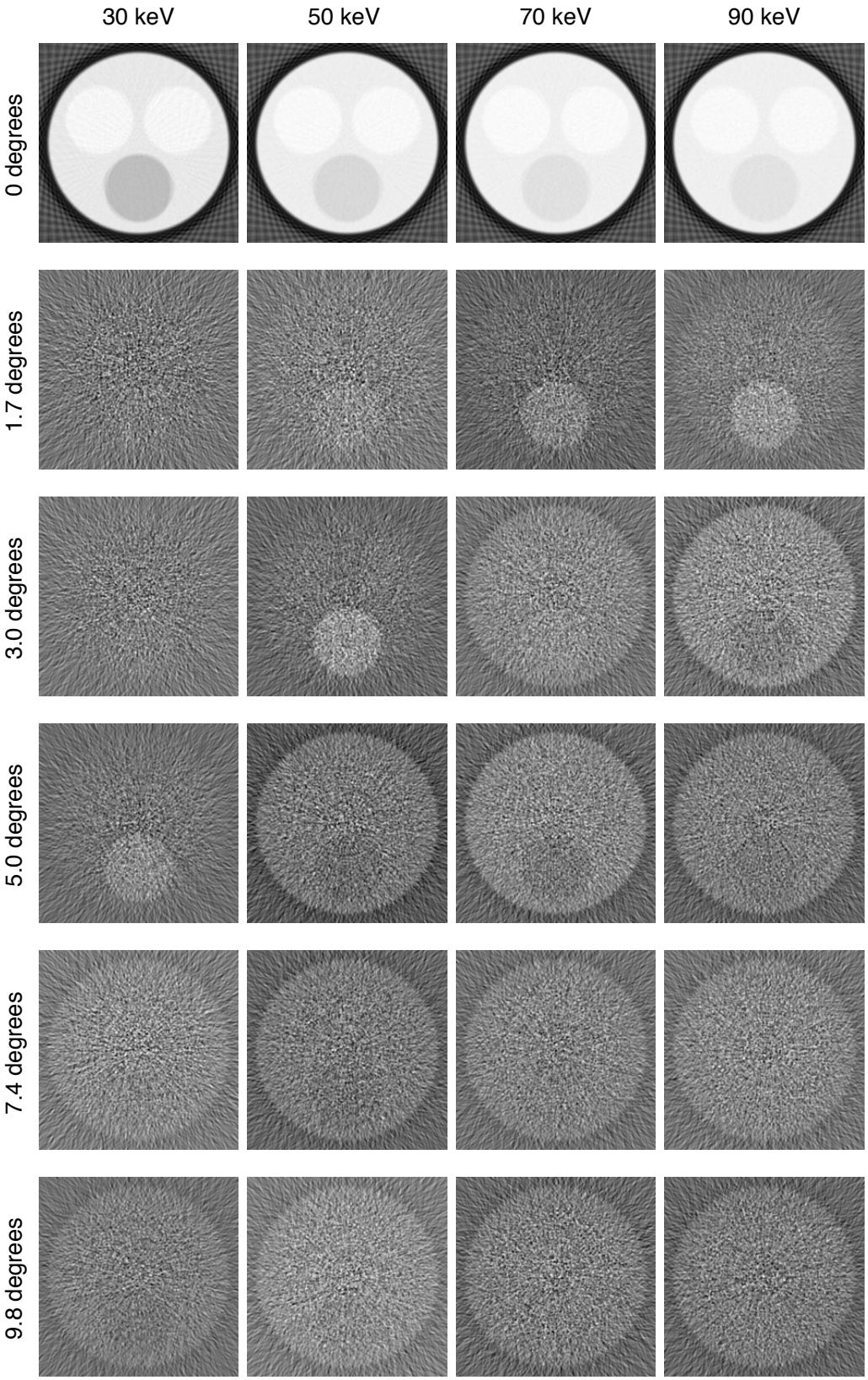

Figure IV.5: CSCT reconstructions for monoenergetic beams (30, 50, 70, 90 keV); 65 view angles; $\times 1$ number of source photons.

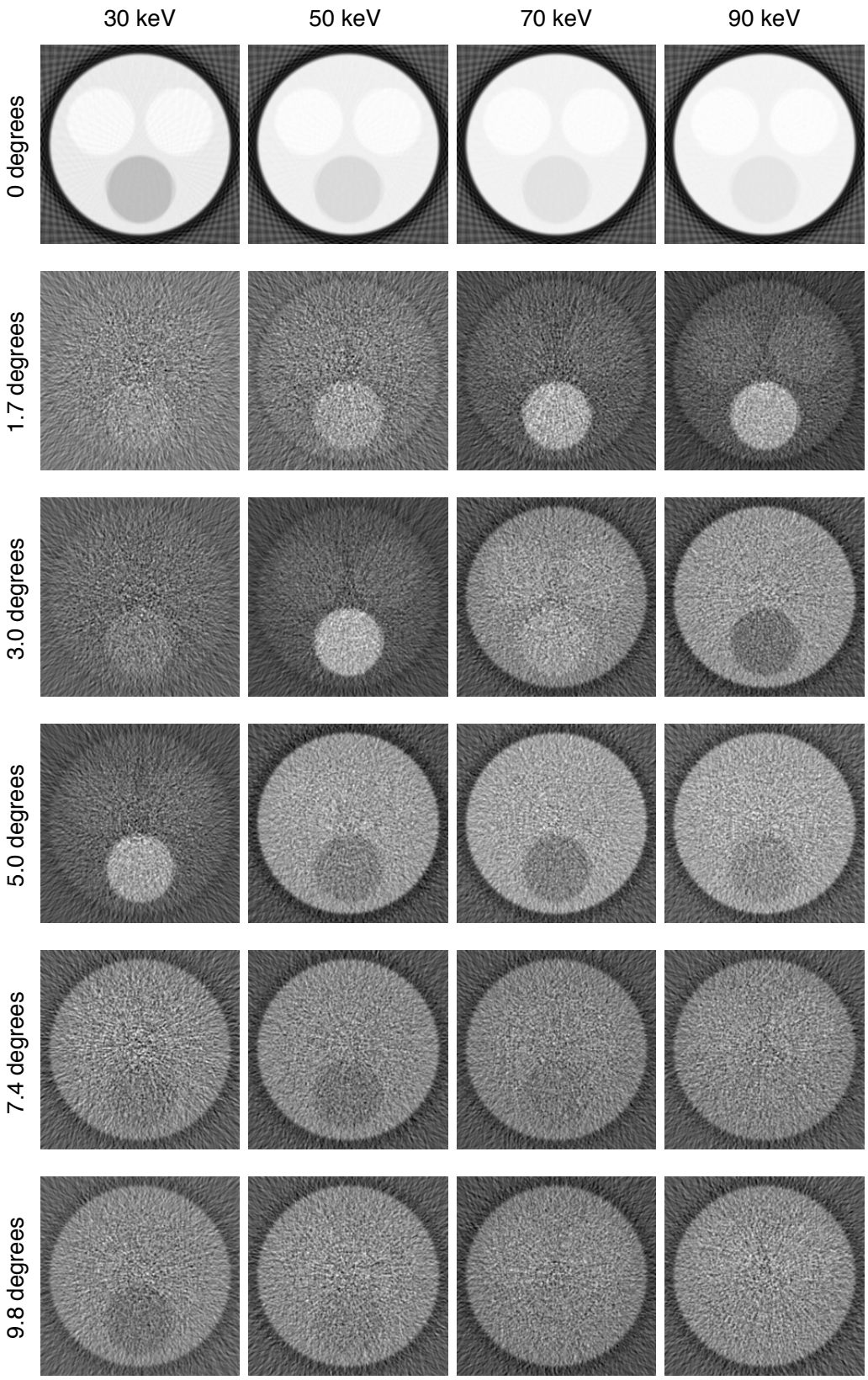

Figure IV.6: CSCT reconstructions for monoenergetic beams (30, 50, 70, 90 keV); 65 view angles; $\times 10$ number of source photons.

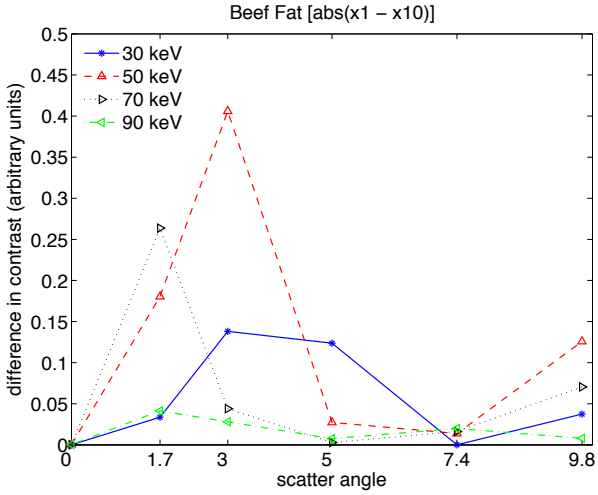

(a) Beef fat

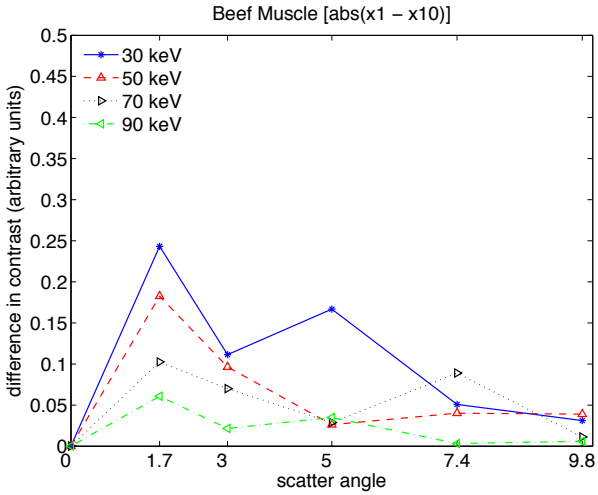

(b) Beef muscle

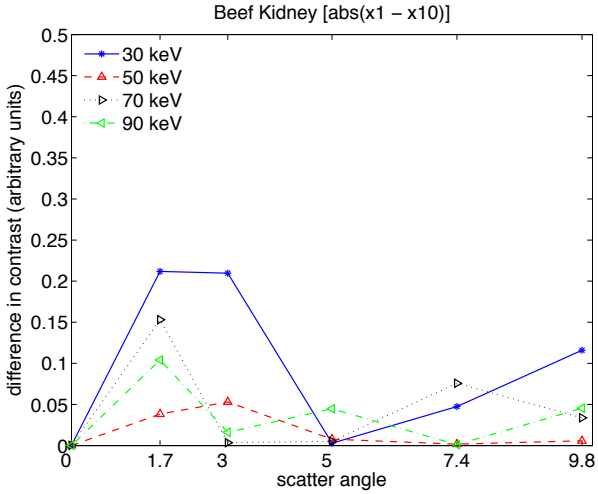

(c) Beef kidney

Figure IV.7: Absolute difference in contrast between ×1 and ×10 measurements.

Table IV.2: Contrast between insert materials and water background for phantom #2 - 30, 50,70, 90 keV, 65 view angles. θ = scatter angle. $\times 10$ = ten times more photons than the $\times 1$ data set.

	30 kVp			50 kVp			70 kVp			90 kVp		
θ	fat	$muscle$	$kidney$	fat	$muscle$	$kidney$	fat	$muscle$	$kidney$	fat	$muscle$	$kidney$
$\times 1$												
0	-0.21	0.07	0.07	-0.10	0.05	0.05	-0.07	0.05	0.05	-0.06	0.04	0.04
1.7	0.91	0.49	0.41	1.34	0.46	0.22	3.19	0.53	0.58	2.27	0.40	0.39
3.0	1.16	0.29	0.13	3.38	0.48	0.73	0.30	0.11	0.15	-0.35	0.05	0.01
5.0	3.39	0.44	0.67	-0.28	0.03	0.01	-0.35	-0.04	-0.04	-0.21	0.09	0.00
7.4	-0.22	0.04	0.02	-0.27	-0.06	0.00	-0.12	0.02	0.01	0.05	0.17	0.13
9.8	-0.45	0.01	-0.18	-0.28	0.06	-0.03	0.08	0.14	0.10	0.01	0.17	0.10
$\times 10$												
0	-0.21	0.07	0.07	-0.10	0.05	0.05	-0.07	0.05	0.05	-0.06	0.04	0.04
1.7	0.94	0.25	0.19	1.16	0.28	0.26	2.93	0.43	0.43	2.23	0.46	0.50
3.0	1.30	0.40	0.34	3.79	0.58	0.68	0.25	0.18	0.15	-0.38	0.03	-0.03
5.0	3.27	0.61	0.67	-0.25	0.06	0.01	-0.35	0.01	-0.03	-0.21	0.05	0.05
7.4	-0.22	0.09	0.07	-0.29	0.02	0.00	-0.14	0.11	0.08	0.03	0.17	0.13
9.8	-0.42	0.04	-0.06	-0.15	0.10	0.03	0.01	0.15	0.13	0.02	0.17	0.15

scatter angle for each beam energy. Specifically, the peak contrast for fat occurs at a scatter angle of 5°, 3°, 1.7°, and 1.7° for 30, 50, 70 and 90 keV, respectively. The scatter peak for fat decreases as the photon energy increases illustrating the forward-peaked nature of coherent scatter, which manifests itself as an increase in fat contrast at lower angles for the higher energy beams. Pixel intensities in the scatter-generated images reflect the scattering properties of the material at that location within the object.

There are other notable CSCT images where several of the materials possess the same contrast. For example, at 70 keV and 3°, muscle, kidney, and fat roughly have the same contrast, and at 70 keV and 5° muscle and kidney are virtually identical but fat is visually distinct.

CNR

As the number of source photons increased from ×1 to ×10, the CNRs of the CSCT images also increased (see table IV.3). Figure IV.8 shows the percent increase in CNR with a ×10 increase in source photon flux. Although not plotted, the muscle and kidney both exhibit an over all increase as well, as can be seen in the CNR table. However, unlike the fat percent CNR increase, for muscle and kidney some of the scatter angles showed a dramatic percent increase in CNR due to the nearly zero CNR measurements at the ×1 photon flux level. For a ×10 increase in photon flux, an increase in the CNR of about $\approx \sqrt{10} = 3.16$ would be expected. In figure IV.8, the fat CNR increased around 250%, which is close to the anticipated amount.

As the photon energy increased more photons penetrated deeper into the phantom, and fewer scattered photons were attenuated as they traveled from their point of interaction to the the detector. An increase in scatter CNR coincided with an increase in beam energy, as illustrated in table IV.3, and was highest for 90 keV for all materials. However, at 0° the CNR trend is just the opposite, it is greatest for all materials at 30 keV, since image contrast is generated by the spatial differential

Table IV.3: CNR of insert materials referenced to water background for phantom #2 - 30, 50,70, 90 keV, 65 view angles. θ = scatter angle. $\times 10$ = ten times more photons than the $\times 1$ data set.

	30 kVp			50 kVp			70 kVp			90 kVp		
θ	fat	$muscle$	$kidney$	fat	$muscle$	$kidney$	fat	$muscle$	$kidney$	fat	$muscle$	$kidney$
$\times 1$												
0	-16.65	5.50	5.42	-11.95	6.36	6.26	-9.12	6.07	5.93	-8.21	6.11	5.94
1.7	0.20	0.11	0.09	0.52	0.18	0.08	1.17	0.20	0.21	1.33	0.23	0.23
3.0	0.23	0.06	0.03	1.50	0.21	0.32	0.29	0.10	0.15	-0.45	0.06	0.01
5.0	1.14	0.15	0.22	-0.40	0.05	0.01	-0.52	-0.06	-0.06	-0.26	0.11	0.00
7.4	-0.14	0.03	0.01	-0.27	-0.06	0.00	-0.11	0.01	0.01	0.04	0.14	0.10
9.8	-0.34	0.01	-0.13	-0.24	0.05	-0.02	0.07	0.11	0.08	0.01	0.15	0.09
$\times 10$												
0	-22.30	7.40	7.29	-17.98	9.54	9.36	-15.58	10.42	10.18	-14.32	10.69	10.42
1.7	0.62	0.16	0.13	1.41	0.34	0.31	3.67	0.54	0.54	4.29	0.89	0.96
3.0	0.79	0.24	0.21	4.94	0.75	0.89	0.85	0.60	0.53	-1.61	0.12	-0.12
5.0	3.18	0.59	0.65	-1.16	0.28	0.06	-1.62	0.05	-0.16	-0.87	0.22	0.19
7.4	-0.47	0.20	0.15	-0.89	0.06	-0.01	-0.36	0.27	0.22	0.07	0.40	0.31
9.8	-0.97	0.10	-0.14	-0.42	0.27	0.09	0.02	0.41	0.36	0.05	0.44	0.40

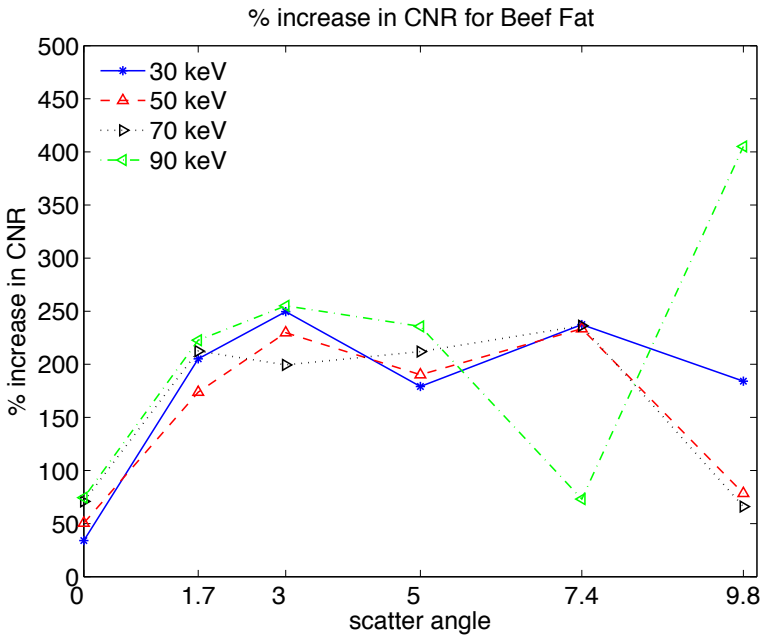

Figure IV.8: % increase in CNR for beef fat between images in figure IV.5 and IV.6.

attenuation of photons by an object. For CSCT images the CNR was highest at high energies and low scatter angles. CNR followed the contrast trend of decreasing as photon energy increased. This is visually noticeable in figure IV.6.

Although the 90 keV 1.7° scatter image had a higher CNR for fat compared to the 70 keV image at the same angle, an inspection of table IV.2 reveals that the 70 keV image had a slightly higher contrast. This is most likely due to a larger amount of separation between the maximum scatter peaks of different materials. That is, at 70 keV and 1.7° scatter from fat contributed slightly more to the signal in the fat region than in the associated 90 keV image where the decreased forward scatter angle slightly increased the amount of scatter in the fat region from other materials. The 70 keV 1.7° scatter image displays roughly equal contrast between fat, muscle, and kidney, which indicates roughly equally photon scatter contributions from each material to the same location on the detector.

There are several scatter angles and energy combinations that possess greater image contrast than the 0° images in figure IV.6 ; however, since the CSCT images

all have much less CNR/photon flux than the 0° images, the contrast resolution is limited.

SNR

In figure IV.6 we see that an increased number of source photons had a positive affect on image quality by reducing noise in the images. Table IV.4 contains the SNR measurements for the material regions, and figure IV.9 displays a plot of the % increase in SNR due to a ×10 fold increase in source photons.

By increasing the number of source photons by ×10 we see that in figure IV.9 SNR increased roughly 200% for all CSCT images, whereas for the attenuation-based images only a 50-100% increase in SNR occurred depending on the material. This demonstrated that CSCT systems were much more sensitive to the number of source photons than traditional CT systems. As the number of photons increased, the number of potential interactions increased, and so did the number of scatter detections.

For all the attenuation-based (0°) and CSCT images, SNR increased either as the number of source photons increased or the energy of the number of source photons increased. In comparison, the CNR for attenuation-based images only increased with the number of photons and decreased with an increase in source photon energy, while for CSCT images the CNR increased with either an increase in the number of source photons or their energy, just like the SNR measurements.

45, 60, 75, 85 keV; 128 Views; x1

All simulations in this section used 128 sample angles and the same number of source photons per image acquisition, 2.8×10^{11} photons – essentially double of that used for the 30, 50, 70, 90 keV ×10 simuliations. Figure IV.10 illustrates the FBP reconstructed CSCT images of phantom #2 for 45, 60, 75, and 85 keV. Increasing the number of angular samples reduced the FBP reconstruction artifact due to a

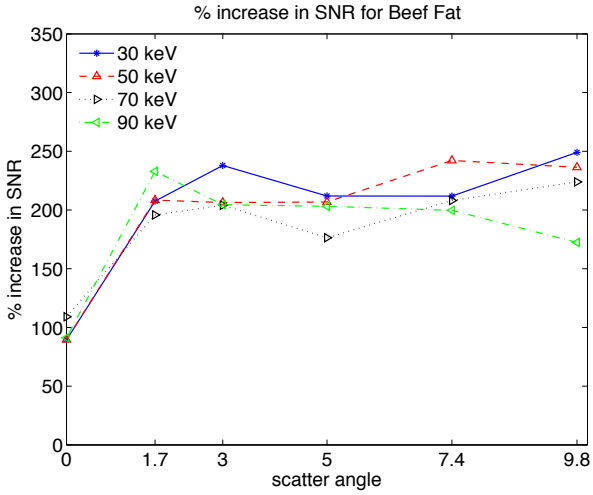

(a) % increase SNR for fat

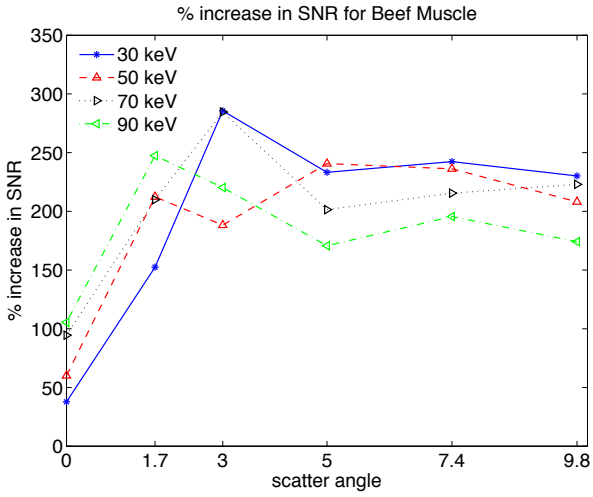

(b) % increase SNR for muscle

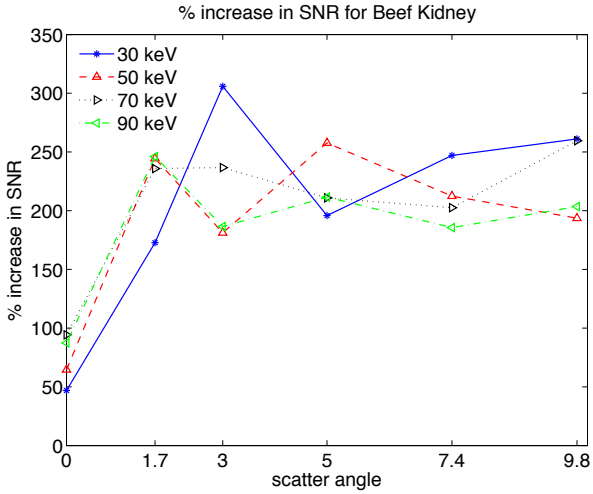

(c) % increase SNR for kidney

Figure IV.9: % increase in SNR from $\times 1$ to $\times 10$ the number source photons.

Table IV.4: SNR for phantom #2 - 30, 50,70, 90 keV, 65 view angles. θ = scatter angle. $\times 10$ = ten times more photons than $\times 1$ data set.

	30 kVp			50 kVp			70 kVp			90 kVp		
θ	fat	$muscle$	$kidney$	fat	$muscle$	$kidney$	fat	$muscle$	$kidney$	fat	$muscle$	$kidney$
$\times 1$												
0	85.05	83.86	80.30	124.18	121.82	118.60	118.16	128.68	127.91	138.33	134.51	143.35
1.7	0.40	0.28	0.25	0.76	0.48	0.41	1.26	0.52	0.53	1.57	0.76	0.75
3.0	0.38	0.20	0.19	1.50	0.61	0.71	1.16	0.93	1.00	0.85	1.21	1.24
5.0	1.16	0.40	0.48	1.06	1.24	1.24	1.05	1.28	1.34	0.99	1.36	1.19
7.4	0.53	0.55	0.55	0.63	0.81	0.89	0.73	0.79	0.78	0.78	0.91	0.86
9.8	0.41	0.61	0.51	0.62	0.80	0.77	0.82	0.88	0.83	0.89	1.00	0.95
$\times 10$												
0	161.11	115.57	117.99	235.38	195.08	195.18	247.10	250.27	248.46	264.54	276.43	268.57
1.7	1.23	0.70	0.69	2.35	1.49	1.40	3.72	1.62	1.76	5.23	2.63	2.60
3.0	1.30	0.78	0.75	4.61	1.74	1.99	3.54	3.57	3.38	2.60	3.87	3.54
5.0	3.61	1.34	1.41	3.27	4.21	4.44	2.89	3.84	4.17	3.01	3.68	3.70
7.4	1.66	1.88	1.90	2.16	2.73	2.77	2.25	2.48	2.37	2.35	2.68	2.45
9.8	1.44	2.00	1.85	2.09	2.46	2.26	2.67	2.83	2.99	2.42	2.75	2.88

large sampling angle step size. This reduction can be noticed by comparing the space outside the reconstructed object in both figures IV.10 and IV.6. Also, the reduced sampled step size for the simulations in this section resulted in more photons being used to generate scatter data for the CSCT images, which ultimately reduced the amount of noise in the CSCT images. Most of the observations made for the 65 sample angle data set have their counterparts in 128 sample angle data set. Although it was difficult to perform a straight comparison of the 45, 60, 75, 85 keV data set with the 30, 50, 70, 90 keV as the energy and number photons used were different.

Contrast

The 45, 60, 75, 85 keV attenuation-based image contrast measurements in table IV.5 showed a similar reduction in contrast like the data in table IV.2 for 30, 50, 70, 90 keV as the photon energy increased.

The CSCT images in figure IV.10 exhibited the same inversion of the material contrast at scatter angles beyond the peak fat contrast scatter angle for each beam energy, similar to the CSCT images in figure IV.6. However, since these simulations were performed at slightly higher photon energies, the peak contrast for fat occurred at a lower scatter angles: 3°, for 45 keV and at 1.7° for 60, 75, and 85 keV.

The equal material contrast seen in figure IV.6 at 3° for 70 keV between muscle, kidney, and fat has now changed in figure IV.10 such that all the materials are virtually indistinguishable from water. This indicates that the contribution of photon scatter into this sampling scatter angle was roughly the same for all materials. At higher scattering angle the amount of material contrast is significantly reduced, but figure IV.10 still showed a slightly discernible amount of contrast that was not easily perceived in figure IV.6.

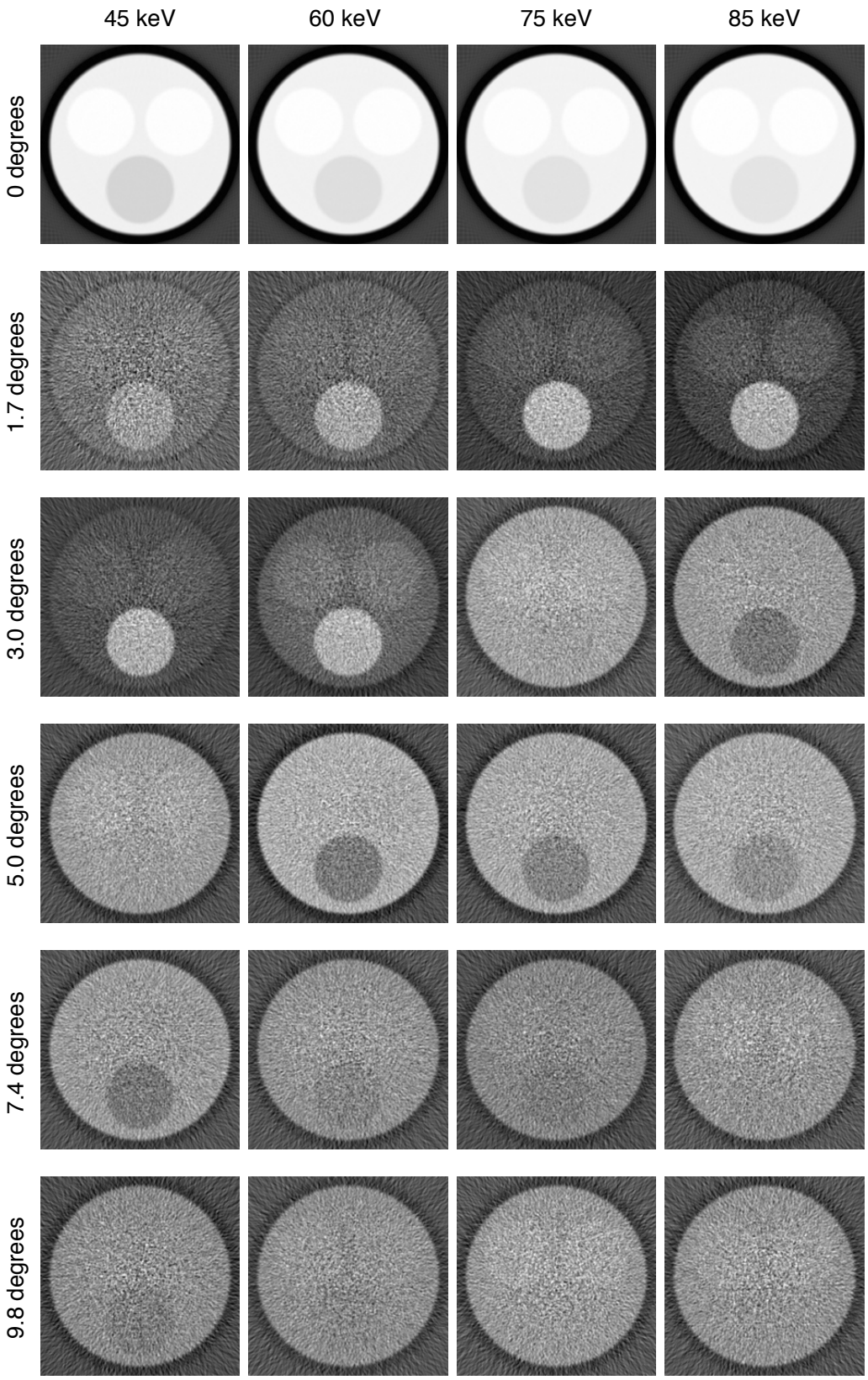

Figure IV.10: CSCT reconstructions for monoenergetic beams (45, 60, 75, 85 keV); 128 view angles.

Table IV.5: Contrast between insert materials and water background for phantom #2 - 45, 60,75, 85 keV, 128 view angles, 2.6×10^{11} photons total. θ = scatter angle.

	45 kVp			60 kVp			75 kVp			85 kVp		
θ	fat	$muscle$	$kidney$	fat	$muscle$	$kidney$	fat	$muscle$	$kidney$	fat	$muscle$	$kidney$
0	-0.12	0.06	0.05	-0.08	0.05	0.05	-0.07	0.05	0.04	-0.06	0.04	0.04
1.7	1.01	0.25	0.28	1.74	0.30	0.29	3.11	0.44	0.44	2.71	0.51	0.56
3.0	4.35	0.57	0.60	1.43	0.38	0.41	-0.04	0.13	0.09	-0.33	0.07	0.03
5.0	-0.01	0.11	0.11	-0.40	0.00	-0.04	-0.30	0.05	0.00	-0.25	0.04	0.01
7.4	-0.36	0.01	-0.03	-0.16	0.11	0.07	-0.13	0.10	0.09	-0.02	0.15	0.12
9.8	-0.16	0.08	0.03	-0.09	0.10	0.05	0.00	0.15	0.14	0.00	0.14	0.14

Table IV.6: CNR of insert materials referenced to water background for phantom #2 - 45, 60,75, 85 keV, 128 view angles, 2.6×10^{11} photons total. θ = scatter angle.

	45 kVp			60 kVp			75 kVp			85 kVp		
θ	fat	$muscle$	$kidney$	fat	$muscle$	$kidney$	fat	$muscle$	$kidney$	fat	$muscle$	$kidney$
0	-49.77	23.90	23.30	-38.10	23.53	22.88	-32.67	22.44	21.82	-32.35	23.47	22.79
1.7	1.72	0.43	0.47	3.41	0.59	0.57	6.26	0.89	0.88	6.59	1.24	1.35
3.0	6.21	0.82	0.86	4.83	1.28	1.37	-0.21	0.69	0.44	-1.93	0.40	0.18
5.0	-0.05	0.63	0.60	-2.66	-0.03	-0.28	-1.82	0.28	-0.03	-1.44	0.22	0.05
7.4	-1.66	0.02	-0.13	-0.63	0.45	0.27	-0.49	0.38	0.33	-0.09	0.55	0.42
9.8	-0.66	0.32	0.11	-0.34	0.38	0.20	0.02	0.59	0.56	0.01	0.53	0.54

Table IV.7: SNR for phantom #2 - 45, 60,75, 85 keV, 128 view angles, 2.6×10^{11} photons total. θ = scatter angle.

	45 kVp			60 kVp			75 kVp			85 kVp		
θ	fat	$muscle$	$kidney$	fat	$muscle$	$kidney$	fat	$muscle$	$kidney$	fat	$muscle$	$kidney$
0	464.93	445.46	506.99	483.05	514.67	536.62	485.00	536.10	515.26	535.82	568.02	597.48
1.7	2.70	1.66	1.72	3.97	2.13	2.11	5.98	2.53	2.70	6.77	3.24	3.52
3.0	5.38	1.91	2.01	6.64	3.73	4.07	4.47	5.09	5.21	3.81	4.73	5.17
5.0	4.93	5.07	5.06	4.23	5.93	5.74	4.36	5.27	4.98	4.01	5.01	4.77
7.4	2.84	3.75	3.62	3.30	3.79	3.84	3.12	3.52	3.74	3.43	3.52	3.58
9.8	2.85	3.73	3.45	3.11	3.34	3.51	3.39	3.98	3.78	3.27	3.61	3.48

CNR

Although the 65 and 128 sample angle data sets were performed at different beam energies, it was interesting to note that by doubling the number of sample angles the scatter CNR improved due to the increased number of source photons.

The CNR for the 45, 60, 75, 85 keV - 128 sample angle data set, table IV.6, showed a roughly two fold increase over the CNR for the 30, 50, 70, 90 keV - 65 sample angle data set, table IV.3 $\times 10$. The increased energy of the 128 data set also contributed to the greater scatter photon detection. As previously illustrated with the 65 sample angle data set, an increase in energy results in an increase in CNR. The same is seen with the 45, 60, 75, and 85 keV source beams. A combination of more photons and higher energies lead to an increase in the penetration depth and the number of scatter interactions within the phantom, which resulted in more detected scatter photons and lower noise in the reconstructed CSCT images.

SNR

The most significant difference between the 45, 60, 75, 85 keV - 128 sample angle data set and the 30, 50, 70, 90 keV - 65 sample angle data set, was in their SNR measurements, see tables IV.7 and IV.4. The SNR measurements for the 45, 60, 75, 85 keV - 128 sample angle data set were approximately 1.5 to 2 times higher than the 30, 50, 70, 90 keV - 65 sample angle data set at the same scatter angle. The improvement in noise reduction due to the increased number of sampling angles and increased number of source photons is evident in the improved resolution and detail in distinguishing the material regions in figure IV.10 compared to figure IV.6.

W 80, W 120, W 140 kVp; 128 Views; x1, x10, x100

Contrast

Figures IV.11, IV.12, and IV.13 display the reconstructed CSCT images for a relative number of source photons $\times 1$, $\times 10$, and $\times 100$, respectively. Contrast measurements for the three different source photon fluxes are listed in table IV.8. Like the 30, 50, 70, 90 keV experiments, the attenuation-based images have constant image contrast for the $\times 1$, $\times 10$, and $\times 100$ source photon flux, while the CSCT images show some fluctuations in image contrast at the lowest photon flux. Differences in image contrast between $\times 10$ and $\times 100$ for all materials and energies appear to be minimal, essentially the image contrast is constant between these two data sets. Since contrast is a difference comparison between the signal intensity between regions, and since signal in CSCT images is highly dependent upon the amount of detected scatter, any variability in CSCT image contrast is due a reduction in scattered photons at lower source photon fluxes.

In figure IV.13 the contrast in the 120 kVp and 140 kVp CSCT images were more similar than either was with the 80 kVp images. Since the effective energies of the 80, 120, and 140 kVp spectra were 46, 60, and 66 keV, respectively, it was reasonable to conclude that since the 120 kVp and 140 kVp have similar effective energies then the contrast in their associated CSCT images should be similar, which they were.

As in the previous experiments, the peak scatter image for fat shifted to a lower scattering angle as the effective energy of the spectra increased, which is consistent with Rayleigh scattering theory.

CNR

Table IV.9 contains CNR measurements of the polyenergetic generated CSCT images for $\times 1$, $\times 10$, and $\times 100$ the number of source photons. The CNRs of table IV.9 showed the same dependance on number of source photons as the monoenergetic CNRs

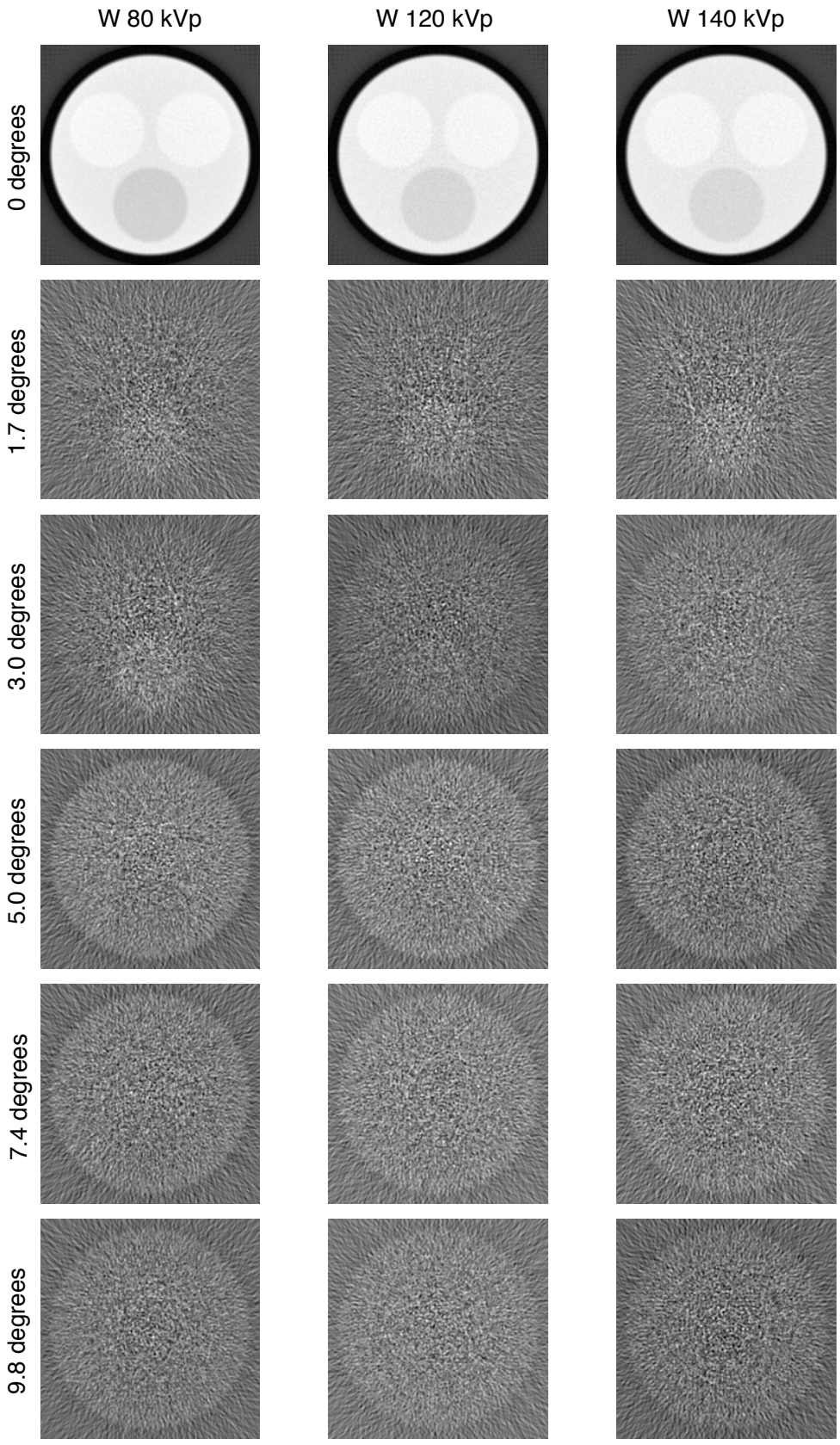

Figure IV.11: 128 view angles; CSCT reconstructions for tungsten spectra with $\times 1$ number of source photons.

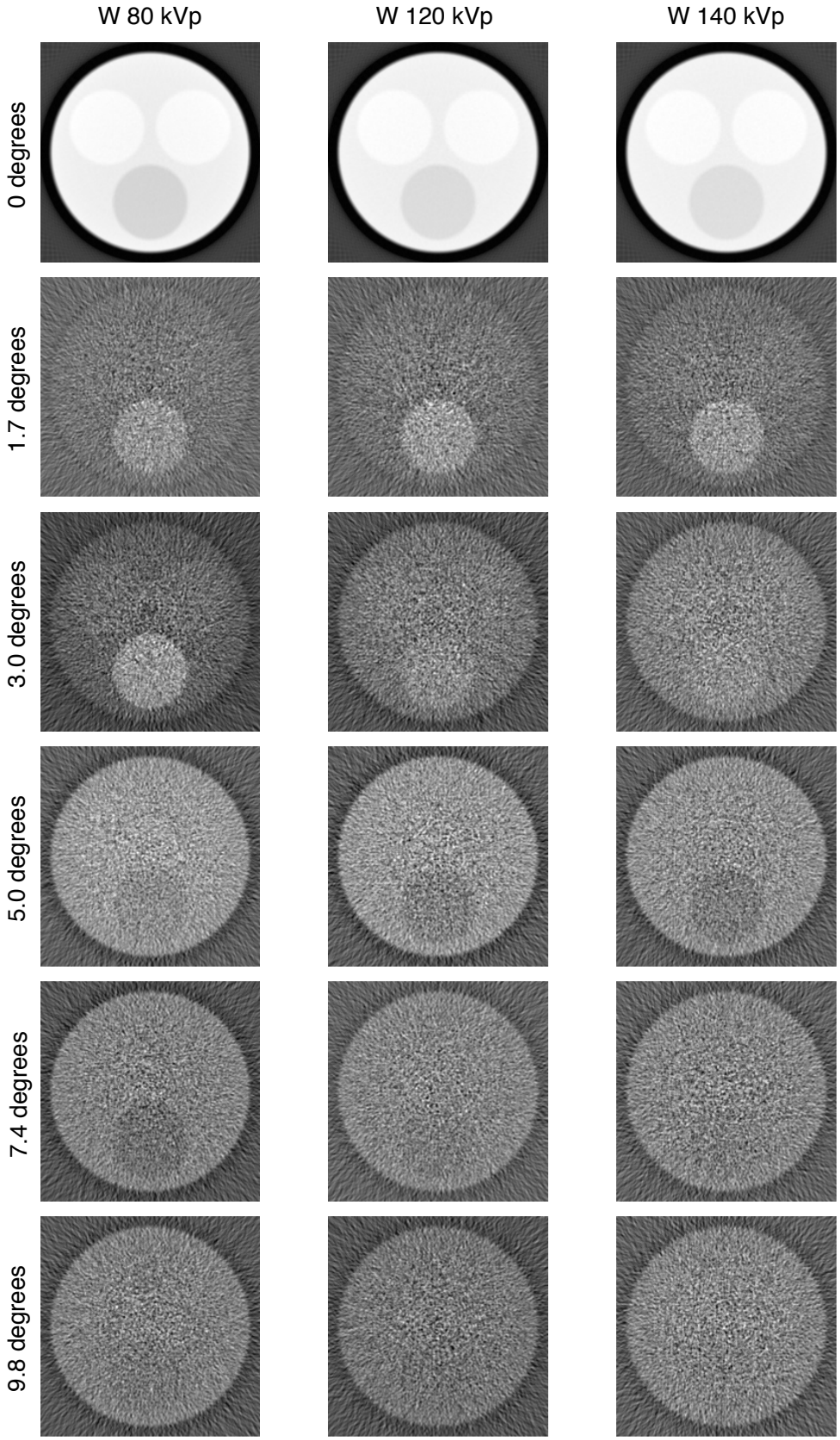

Figure IV.12: 128 view angles; CSCT reconstructions for tungsten spectra with $\times 10$ the number of source photons used in figure IV.11.

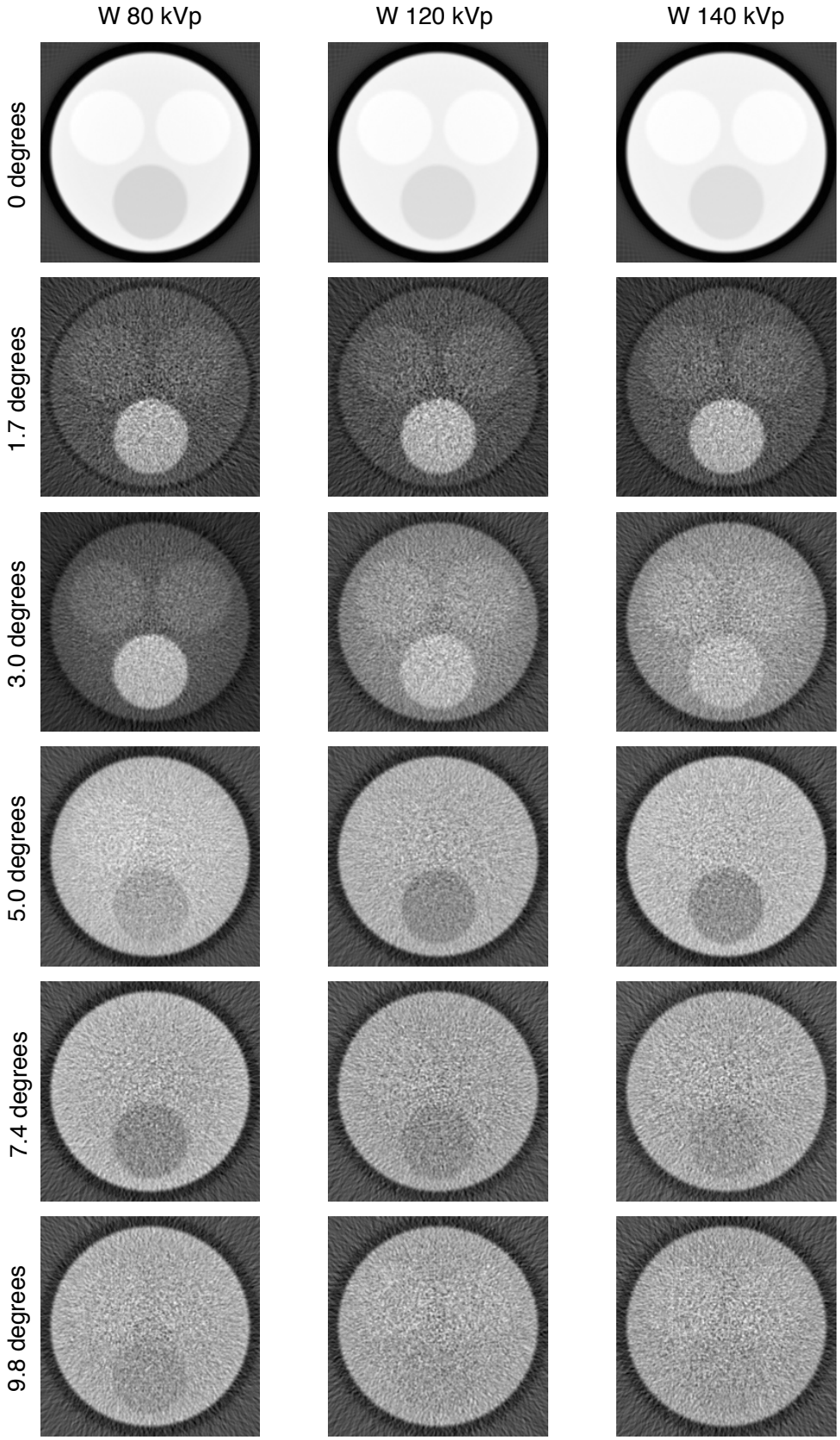

Figure IV.13: 128 view angles; CSCT reconstructions for tungsten spectra with $\times 100$ the number of source photons used in figure IV.11.

Table IV.8: Contrast between insert materials and water background for phantom #2 - tungsten spectra: 80, 120, 140 kVp; 128 view angles. θ = scatter angle. $\times 10$ = ten times more photons than the $\times 1$ data set; $\times 100$ = 100 times more photons than the $\times 1$ data set.

	$W80\ kVp$			$W120\ kVp$			$W140\ kVp$		
θ	fat	$muscle$	$kidney$	fat	$muscle$	$kidney$	fat	$muscle$	$kidney$
$\times 1$									
0	-0.11	0.04	0.04	-0.09	0.04	0.04	-0.08	0.04	0.04
1.7	1.97	0.31	0.17	1.40	0.24	0.56	1.65	0.45	0.51
3.0	1.54	0.52	0.69	0.52	0.31	0.39	0.29	0.30	0.26
5.0	-0.19	0.13	0.06	-0.25	-0.03	-0.02	-0.37	-0.09	-0.13
7.4	-0.26	-0.02	-0.01	-0.15	0.13	0.07	-0.12	0.09	0.01
9.8	-0.20	0.08	0.02	-0.18	0.12	0.02	-0.01	0.12	0.00
$\times 10$									
0	-0.11	0.04	0.04	-0.09	0.04	0.04	-0.08	0.04	0.04
1.7	1.74	0.24	0.33	1.78	0.41	0.33	1.50	0.31	0.40
3.0	1.55	0.42	0.42	0.53	0.24	0.20	0.28	0.16	0.14
5.0	-0.14	0.07	0.03	-0.26	0.01	-0.03	-0.28	0.01	-0.02
7.4	-0.28	0.02	0.00	-0.20	0.07	0.03	-0.16	0.01	0.02
9.8	-0.16	0.04	0.02	-0.10	0.08	0.06	-0.08	0.09	0.06
$\times 100$									
0	-0.11	0.04	0.04	-0.09	0.04	0.04	-0.08	0.04	0.04
1.7	1.60	0.29	0.31	1.94	0.39	0.38	1.66	0.34	0.34
3.0	1.65	0.43	0.45	0.51	0.23	0.21	0.33	0.18	0.14
5.0	-0.14	0.07	0.04	-0.25	0.03	-0.01	-0.28	0.02	-0.02
7.4	-0.27	-0.01	-0.04	-0.20	0.02	0.01	-0.17	0.04	0.01
9.8	-0.15	0.05	0.02	-0.08	0.07	0.07	-0.04	0.09	0.08

in table IV.3, that is, CNR increased as the number of source photons increased. However, unlike the monoenergetic attenuation-based images, which exhibited a reduction in CNR as the source photon energy increased, for the polyenergetic attenuation-based images at $\times 10$ and $\times 100$ source photon flux, there was an increase in the CNR. The material region scatter CNR were generally highest at 80 kVp and about equal at 120 and 140 kVp, and the scatter CNR tended to increase as the number of source photons increased. (This observation is likely due to the effective energies of the the 120 kVp and 140 kVp beams being only 6 keV apart.)

SNR

Table IV.10 contains the SNR measurements for the polyenergetic beams. Similar to the CNR measurements, the 120 kVp and 140 kVp SNR measurements were closer to each other than the 80 kVp SNR measurement for the same number of source photons. Again, this was likely due to the effective energies of the the 120 kVp and 140 kVp beams being only 6 keV apart. As expected, the SNR increased as the number of source photons increased. This aspect is easily demonstrated in figures IV.11, IV.12, and IV.13. As the noise was lowered, material region resolution improved and became more distinguishable at the higher scatter angles.

Figure IV.14 shows the % increase in SNR as function of scatter angle for ten fold increase in source photon flux. The plots in figure IV.14 for $\times 10$ to $\times 100$ are similar to the plots in figure IV.9 for the 30, 50, 70, 90 keV beams. Both sets show an increase of about 200% for the scatter SNR measurements.

Mo 32 kVp; 128 Views; x1, x10

Contrast

FIgure IV.15 shows the CSCT images produced from the 32 kVp molybdenum spectrum. The contrast between the two molybdenum runs remained identical for the

Table IV.9: CNR of insert materials referenced to water background for phantom #2 - tungsten spectra: 80, 120, 140 kVp; 128 view angles. θ = scatter angle. $\times 10$ = ten times more photons than the $\times 1$ data set; $\times 100$ = 100 times more photons than the $\times 1$ data set.

	$W80\ kVp$			$W120\ kVp$			$W140\ kVp$		
θ	fat	$muscle$	$kidney$	fat	$muscle$	$kidney$	fat	$muscle$	$kidney$
$\times 1$									
0	-11.18	4.17	4.06	-8.23	3.96	3.90	-7.47	4.05	4.00
1.7	0.58	0.09	0.05	0.44	0.08	0.18	0.58	0.16	0.18
3.0	0.66	0.22	0.30	0.29	0.17	0.21	0.18	0.18	0.16
5.0	-0.20	0.14	0.06	-0.21	-0.02	-0.02	-0.33	-0.08	-0.11
7.4	-0.21	-0.018	-0.01	-0.09	0.08	0.04	-0.06	0.05	0.00
9.8	-0.14	0.06	0.02	-0.11	0.07	0.01	-0.01	0.07	0.00
$\times 10$									
0	-17.23	6.49	6.37	-18.08	8.85	8.67	-18.41	9.89	9.67
1.7	1.67	0.23	0.32	1.83	0.42	0.33	1.71	0.35	0.46
3.0	2.25	0.61	0.61	0.93	0.43	0.36	0.52	0.30	0.26
5.0	-0.44	0.23	0.10	-0.77	0.03	-0.10	-0.74	0.03	-0.04
7.4	-0.70	0.06	0.01	-0.35	0.13	0.05	- 0.28	0.01	0.04
9.8	-0.36	0.10	0.04	-0.17	0.14	0.11	-0.14	0.17	0.10
$\times 100$									
0	-18.68	7.01	6.89	-23.10	11.28	11.05	-25.82	13.91	13.58
1.7	4.90	0.88	0.94	5.64	1.12	1.12	5.44	1.12	1.14
3.0	7.41	1.93	2.00	2.87	1.28	1.18	1.90	1.03	0.84
5.0	-1.52	0.78	0.3	-2.21	0.25	-0.06	-2.40	0.15	-0.13
7.4	-2.06	-0.09	-0.33	-1.19	0.13	0.06	-0.97	0.20	0.05
9.8	-0.99	0.32	0.1	-0.50	0.39	0.39	-0.22	0.50	0.43

Table IV.10: SNR for phantom #2 - tungsten spectra: 80, 120, 140 kVp; 128 view angles. θ = scatter angle. $\times 10$ = ten times more photons than the $\times 1$ data set; $\times 100$ = 100 times more photons than the $\times 1$ data set.

	$W80\ kVp$			$W120\ kVp$			$W140\ kVp$		
θ	fat	$muscle$	$kidney$	fat	$muscle$	$kidney$	fat	$muscle$	$kidney$
$\times 1$									
0	100.65	105.86	101.85	87.18	90.91	94.91	81.92	90.30	88.67
1.7	0.66	0.33	0.29	0.60	0.35	0.43	0.70	0.40	0.45
3.0	0.90	0.54	0.58	0.72	0.59	0.63	0.67	0.68	0.64
5.0	0.79	0.95	0.95	0.64	0.71	0.76	0.54	0.68	0.65
7.4	0.52	0.67	0.64	0.47	0.57	0.56	0.42	0.47	0.45
9.8	0.51	0.64	0.64	0.47	0.57	0.56	0.52	0.56	0.50
$\times 10$									
0	265.71	262.78	256.65	257.61	252.67	259.73	252.69	269.57	271.86
1.7	2.03	0.98	1.09	2.16	1.22	1.07	2.23	1.22	1.42
3.0	2.87	1.70	1.72	2.27	1.90	1.77	2.12	1.77	1.70
5.0	2.75	2.78	2.89	1.95	2.51	2.33	1.87	2.32	2.27
7.4	1.73	2.12	2.14	1.39	1.62	1.76	1.43	1.50	1.54
9.8	1.81	1.83	1.91	1.45	1.67	1.63	1.43	1.71	1.65
$\times 100$									
0	463.75	371.27	366.40	505.98	489.54	489.94	545.83	526.44	521.30
1.7	6.30	3.23	3.44	6.45	3.32	3.56	7.10	3.41	3.64
3.0	9.65	5.47	5.55	7.17	5.69	6.22	7.04	5.63	6.01
5.0	8.44	9.80	9.77	6.63	7.43	7.15	6.28	7.51	7.63
7.4	5.00	5.81	6.19	4.33	5.08	5.27	4.46	4.82	4.75
9.8	5.23	5.81	5.57	5.17	5.41	5.39	4.87	5.12	5.11

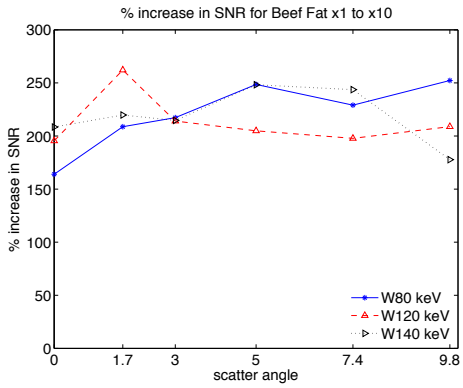

(a) Fat: ×1 to ×10

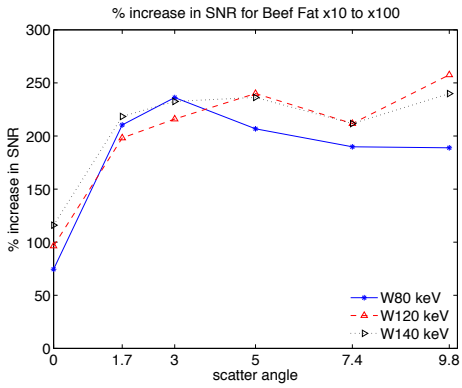

(b) Fat: ×10 to ×100

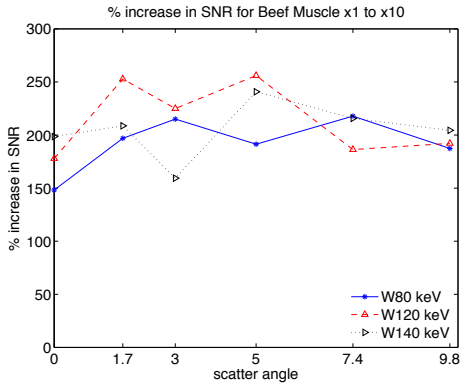

(c) Muscle: ×1 to ×10

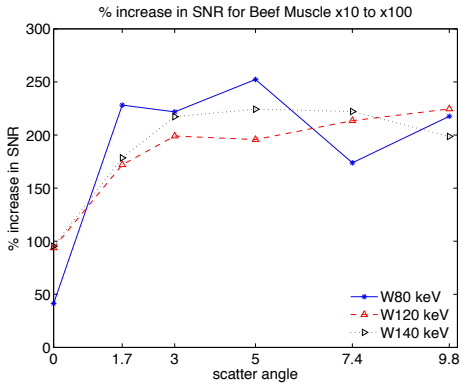

(d) Muscle: ×10 to ×100

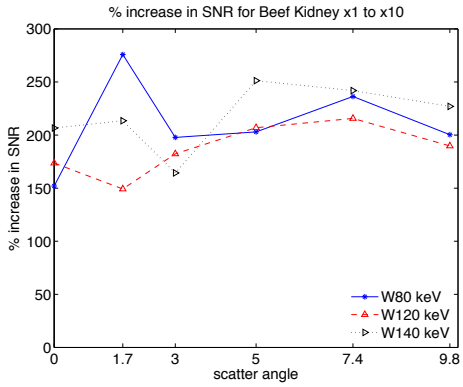

(e) Kidney: ×1 to ×10

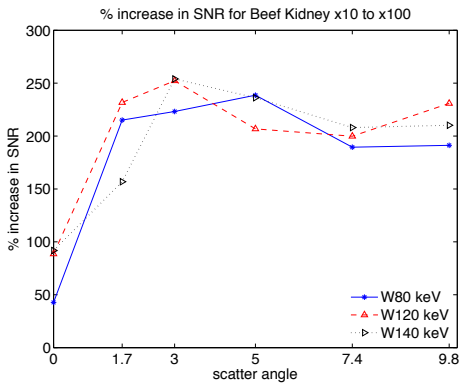

(f) Kidney: ×10 to ×100

Figure IV.14: % increase in SNR from ×1 to ×10 & from ×1 to ×100 the number of source photons.

attenuation based images, just like for the monoenergetic and tungsten polyenergetic experiments (table IV.11. The Mo 32 kVp attenuation based images also possessed similar contrast for the muscle and kidney regions compared to the tungsten images, but had higher contrast for the fat regions. The lower energy Mo spectrum produced more CSCT images with a positive fat contrast than did any of the tungsten spectra, which was expected since lower energy photons forward scatter at larger angles. Assuming that the contrast measurements followed Poisson statistics, all of the $\times 10$ measurements, except for fat and kidney at 3.0°, were within one standard deviation of the $\times 1$ measurement. About the only material that can be distinguished visually with any certainty is the fat region due to the high noise content.

Table IV.11: Contrast between insert materials and water background for phantom #2 - Mo 32 kVp, 128 view angles. θ = scatter angle. $\times 10$ = ten times more photons than the $\times 1$ data set.

	Mo 32 kVp, $\times 1$			Mo 32 kVp, $\times 10$		
θ	fat	$muscle$	$kidney$	fat	$muscle$	$kidney$
0	-0.26	-0.05	-0.04	-0.26	-0.05	-0.04
1.7	1.51	0.85	-0.06	0.78	0.05	0.18
3.0	0.70	-0.59	-0.12	1.39	0.62	0.40
5.0	4.32	1.12	0.84	3.70	0.75	0.79
7.4	0.63	0.44	0.49	0.43	0.30	0.31
9.8	-0.18	0.18	0.13	-0.31	0.02	-0.03

CNR

Like the contrast measurements, all the CNR measurements (table IV.12) were less than the tungsten and monoenergetic spectra CSCT measurements. As can be seen in figure IV.15, the $\times 10$ images contained less noise than the $\times 1$ images, and thus, higher CNR. This observation tracks with the previous experimental results, as does the higher CNR for fat compared to muscle and kidney regions. The high noise definitely impairs visually distinguishing the different material regions.

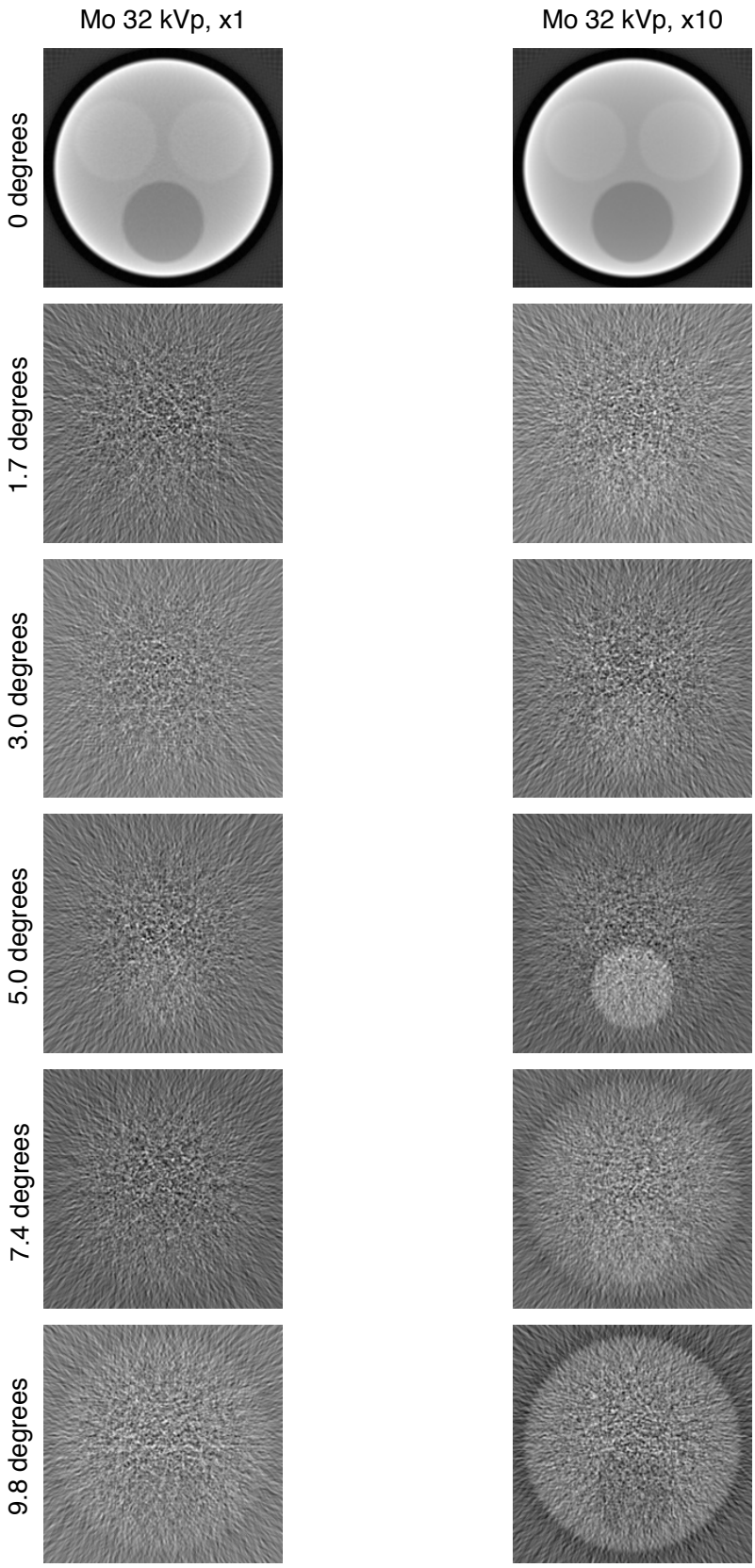

Figure IV.15: 128 view angles; CSCT reconstructions for Molybdenum spectra at 32 kVp; right column used $\times 10$ more photons than the left column.

Table IV.12: CNR of insert materials referenced to water background for phantom #2 - Mo 32 kVp, 128 view angles. θ = scatter angle. $\times 10$ = ten times more photons than the $\times 1$ data set.

	Mo 32 kVp, $\times 1$			Mo 32 kVp, $\times 10$		
θ	fat	$muscle$	$kidney$	fat	$muscle$	$kidney$
0	-4.03	-0.75	-0.69	-4.06	-0.76	-0.70
1.7	0.17	0.10	-0.01	0.36	0.03	0.09
3.0	0.13	-0.11	-0.02	0.60	0.27	0.17
5.0	0.66	0.17	0.13	2.13	0.44	0.45
7.4	0.22	0.16	0.17	0.50	0.35	0.35
9.8	-0.09	0.09	0.07	-0.55	0.03	-0.05

SNR

Due to the low penetrating ability of the photons in the Mo spectrum, the CSCT images contained more noise than the previous tungsten and monoenergetic spectra produced CSCT images.

The $\times 10$ Mo CSCT 3° (figure IV.15) image is visually similar to the $\times 1$ 30 keV 3° image (figure IV.5); however, the number of photons used to create the molybdenum image (1.4×10^{12} photons) was 100 times greater than the photons used in the 30 keV case (1.43×10^{10}). This demonstrated that a monoenergetic beam with fewer photons produces a lower noise image than does a polyenergetic spectrum with roughly the same peak kV and more than 100 times the number of photons. A greater number of lower energy photons in the molybdenum spectrum were attenuated, which lead to a lower scatter signal, than in the monoenergetic case. Attenuation of the lower energy photons also contributes more to absorbed dose, as will be demonstrated in the dose results section.

Dose

All CSCT images created in this chapter had the amount of energy deposited in the various material regions recorded. The dose deposited in these regions were calculated using a nominal acquisition and image slice thickness of 3.4 mm. Since the

Table IV.13: SNR for phantom #2 - 32 kVp, 128 view angles. θ = scatter angle. $\times 10$ = ten times more photons than the $\times 1$ data set.

	Mo 32 kVp, $\times 1$			Mo 32 kVp, $\times 10$		
θ	fat	$muscle$	$kidney$	fat	$muscle$	$kidney$
0	46.46	49.89	45.96	48.73	53.28	48.60
1.7	0.27	0.17	0.08	0.71	0.36	0.43
3.0	0.28	0.06	0.14	0.86	0.49	0.44
5.0	0.70	0.25	0.24	2.11	0.76	0.77
7.4	0.58	0.39	0.41	1.52	1.16	1.20
9.8	0.45	0.45	0.46	1.22	1.36	1.39

simulation used a parallel ray, Gaussian distributed source, the collimator width and slice thickness were the same and equal to FWHM of the source, which was 3.4 mm, since collimator width is defined at the gantry isocenter.

The energy deposited was found to be proportional to number of source photons used for the simulation. This is analogous to the linearity of dose with mAs for CT scanners. The amount of energy deposited in the phantom is directly proportional to the number of inelastic photon interactions, which in turn is directly promotional to the number of source photons used. This property is used in order to normalize dose by a specific number of photons used.

All Monoenergetic Beams

Table IV.14 and IV.15 contain the simulation dose measurements for two monoenergetic data sets. Table IV.16 combines all the monoenergetic beam doses and normalizes them to 1×10^{10} photons for comparison. In figure IV.16, a plot of the data in table IV.16 revealed a u-shaped dose deposition profile as beam energy increased.

The dose minimum occurred around 60 to 70 keV, which was about the mid-range photon energy used in the experiments. An explanation of the curve's downward portion could be that lower energy photons have higher probability interaction cross section than do higher energy photon, therefore lower energy photons have more inelastic interactions. As for the upward increase in dose with photon energy, its

Table IV.14: Dose to phantom #2 segments; 65 view angles; 1.3×10^{11} source photons reaching the phantom. These simulation measurements are from the 30, 50 70, 90 keV, $\times10$ flux data set.

Energy	dose (mGy)			
(keV)	water	fat	muscle	kidney
30	17.47	9.80	14.45	14.43
50	12.64	9.05	12.87	12.84
70	11.96	9.96	12.26	12.25
90	13.61	12.31	13.75	13.74

Table IV.15: Dose to phantom #2 segments; 128 view angles; 2.6×10^{11} source photons reaching the phantom.

Energy	dose (mGy)			
(keV)	water	fat	muscle	kidney
45	26.52	18.10	26.55	26.50
60	23.43	18.27	24.10	24.06
75	24.11	20.62	24.63	24.61
85	25.78	22.95	26.13	26.12

Table IV.16: Slice thickness 3.4 mm; estimated dose per 1×10^{10} photons to phantom #2 material regions. Data is plotted in figure IV.16.

Energy	dose (mGy)			
(keV)	water	fat	muscle	kidney
30	1.34	0.75	1.11	1.10
45	1.03	0.70	1.03	1.03
50	0.97	0.69	0.99	0.98
60	0.91	0.71	0.94	0.94
70	0.92	0.76	0.94	0.94
75	0.94	0.80	0.96	0.96
85	1.00	0.89	1.02	1.01
90	1.04	0.94	1.05	1.05

possible that the fractional energy deposited per interaction for the highest energy photons, though their interaction cross sections are smaller, is much greater than the fraction energy deposition from the mid-range photons. Also, with an increase in photon energy, there is an increase in photon penetration depth. Therefore, the material regions that rotated towards the detector side and away from the x-ray source see proportionally more higher energy photons, which helps explain the rise in dose for all material regions.

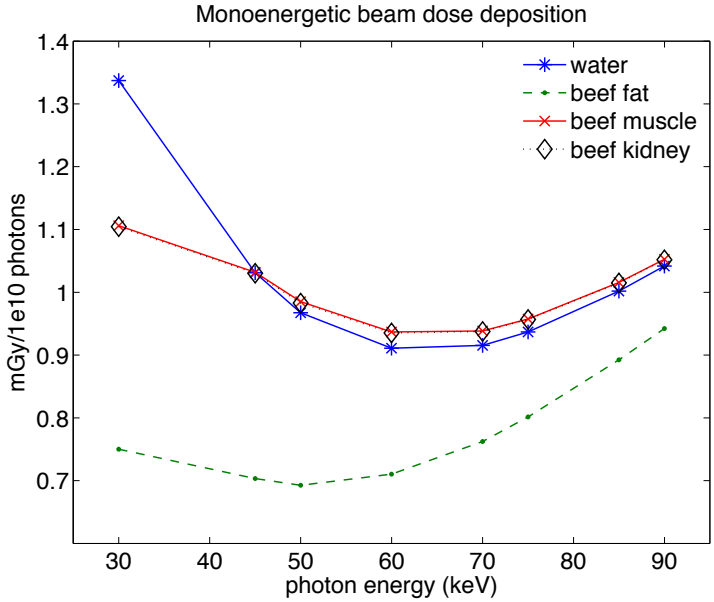

Figure IV.16: Monoenergetic beams: dose per 1×10^{10} photons to phantom #2 material regions.

This suggests that imaging metrics could be optimized with respect to dose. A look back at tables IV.2 and IV.5 showed that the fat contrast was 0.94, 1.01, 1.16, 1.75, 2.93, 3.11, 2.71, and 2.23 for 30, 45, 50, 60, 70, 75, 85, and 90 keV, respectively. The highest fat contrast was 3.11 at 75 keV, which deposited a slightly higher dose than the 60 and 70 keV beams with associated fat contrast simulation measurements of 1.74 and 2.93, respectively. Thus we can conclude that either the 60 or 70 keV beam would be the appropriate selection to minimize dose while maximizing image contrast for fat.

W 80, W 120, W 140 kVp

Table IV.16 reports the dose for the ×100 polyenergetic data set, which corresponds the images in figure IV.13 . The dose deposited was linearly proportional to the number of photons that interact within the object.

Figure IV.17 contains a plot of the data in table IV.16 normalized to 1×10^{10} photons. The plot absissa is labeled with both the kVp and effective energy of the polyenergetic spectra used.

Table IV.17: Tungsten (W) spectra: dose to phantom #2 segments; 128 view angles; ×100 source photon flux.

Energy	dose (mGy)				Number of
(kVp)	water	fat	muscle	kidney	photons
80	90.9	63.5	89.1	88.9	8.83×10^{11}
120	55.2	43.4	55.6	55.6	5.57×10^{11}
140	53.5	44.0	54.2	54.1	5.30×10^{11}

Figure IV.17 showed relatively flat dose deposition in the water based materials compared to monoenergetic beams, figure IV.16, however, the fat did show a similar rise with higher photon energies. The subtle dip in dose to the water based materials is not as dramatic as that for the monoenergetic beam. The dip occurs at the effective energy, 60 keV, which appears to coincided with the same energy as the dose low point in figure IV.16. Although it would be reasonable to conclude the dose to water, muscle, and kidney was constant over the kVp range used, the fact there was significant dose increase to fat indicates that the perceived dip may actually correspond to a true reduction in dose deposition, like the monoergetic case. Like the monoenegetic case, this also suggests that imaging metrics can be optimized for dose, but that the effect may not be as dramatic. Figure IV.13 illustrated that there was not much of visual difference between the three sets of CSCT images.

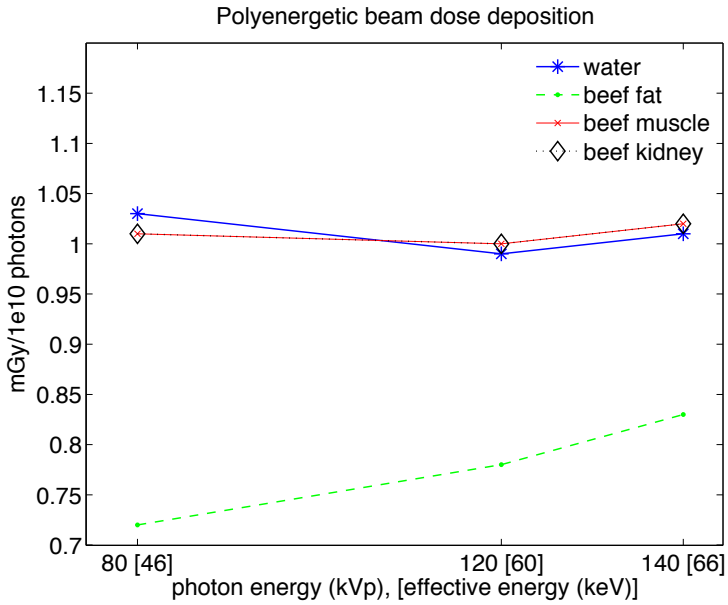

Figure IV.17: Polyenergetic beams: dose per 1×10^{10} photons to phantom #2 material regions.

Mo 32 kVp

Table IV.18 contains the absorbed dose to the phantom regions for the Mo 32 kVp spectrum. It was interesting to note that a increase in the number of photons did not exactly result in a 10 fold increase in absorbed dose to the water, muscle, and kidney regions, as it did for the tungsten and mono energetic beams. It is possible that since a much larger portion of the Mo spectrum contained low energy photons (<17 keV), a greater percentage were attenuated and not detected compared to the higher energy spectra. However, assuming Poisson statistical behavior for the dose, the $\times 10$ doses were within ten times the $\times 1$ $\pm\sigma$ dose simulation measurements.

A look back at the 30, 50, 70 90 keV simulation measurements (table IV.14), which used only 65 sample angles and 1.3×10^{11} photons, showed that the difference between the maximum and minimum dose was less than a factor of two, but for the Mo 32 kVp doses (table IV.18) the maximum to minimum dose spread was about four for roughly the same number of photons used. A comparison with the other spectra revealed a similar trend. It was expected that a majority of the dose would

Table IV.18: Molybdenum (Mo) spectra: dose to phantom #2 segments; 128 view angles; ×1 and ×10 source photon flux. [1]The simulated Mo 32 kVp beam had an inherent filtration of 0.5 mm of Be and no additional filtration. The results in table IV.18 indicated a high energy deposition at the surface of the phantom due to low photon attenuation, as evident in figure IV.18.

Energy	dose (mGy)				Number of
(kVp)	water	fat	muscle	kidney	photons
32	16.9	3.64	4.29	4.29	1.43×10^{11}
32	148.6[1]	36.0	31.8	39.0	1.43×10^{12}

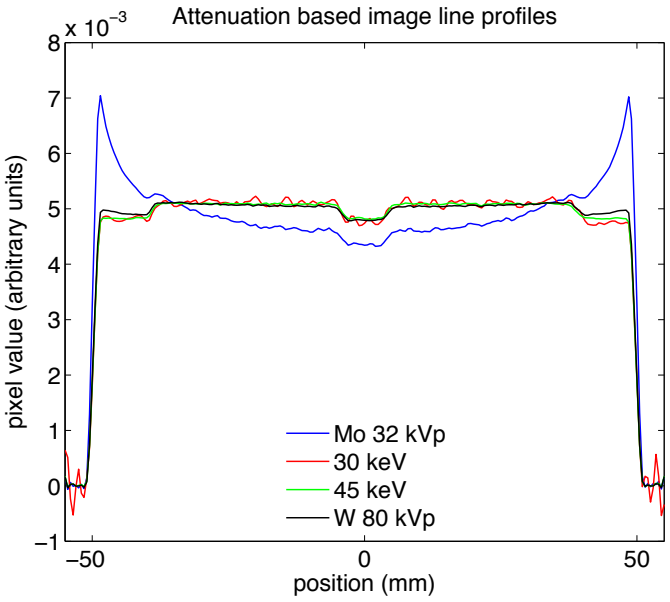

Figure IV.18: Horizontal line profiles across selected attenuation based images. The image produced from the Mo 32 kVp has a cupping artifact due to the attenuation of the lower keV photons at the surface of the phantom. A ratio of the boundary to center pixel values is ∼1.6.

be deposited in the water due to the primarily low energy of the photons used – matter has a higher interaction cross sections for lower energy photons. To put the dose into perspective, the average glandular dose from a single view mammogram to a 8 cm diameter breast composted of 100% glandular tissue is 5.2 mGy for a Mo/Mo target/filter combination[6]. Over all, the molybdenum spectrum delivered the highest dose and lowest CSCT image quality than any of the other spectra investigated.

$\mathbf{CTDI_{100}}$

Tungsten Polyenergetic Beams

$CTDI_{100}$ dose measurements were taken on a Philips Brilliance 16 CT scanner utilizing a 10 cm diameter acrylic phantom and are contained in table IV.19 for a 7.5 mm slice thickness. This data showed that $CTDI_{100}$ increased with both peak photon energy and the number of photons used (mAs). The dose increased linearly with mAs and supra-linearly with kVp.

The associated simulated $CTDI_{100}$ measurements for the 10 cm acrylic phantom are contained in table IV.20. Due to the manner in which the polyenergetic spectra were created attention must be paid to the total number of photons used for each spectra. In the simulations, a set number of photons can be selected regardless of the energy or slice thickness specified. This not the case with a real clinical CT scanner where the number of photons emanating from the source is dependent on mAs, kVp, and source collimation, and an increase in any one of these parameters increases the number of source photons, and thus the dose deposited.

The simulated $CTDI_{100}$ measurements were performed with the same scanning parameters that were used to generate the CSCT images; however, the energy deposited in the simulated ion chamber was taken to be over a 7.5 mm slice thickness in order to match the Philip CT scanner collimation. By comparing the real and simulated

$CTDI_{100}$ measurements an equivalent CT scanner mAs was determined for the simulations. The equivalent mAs values for the simulated CSCT geometry and photon source parameters are contained in table IV.20.

Table IV.19: Philips Brilliance 16: $CTDI_{100}$ to 10 cm diameter acrylic phantom for 7.5 mm slice thickness.

	$CTDI_{100}$ (mGy)		
mAs	80kVp	120kVp	140kVp
30	1.5	4.4	6.3
50	2.3	7.1	10.5
100	4.4	14.5	21.2
200	8.9	29.2	42.1
300	13.2	43.5	63.0

Table IV.20: Polyenergetic simulation: $CTDI_{100}$ to 10 cm diameter acrylic phantom and the equivalent mAs technique interpolated from the measurements in table IV.19.

Energy (kVp)	Number of Photons	$CTDI_{100}$ (mGy)	Equiv. mAs (mAs)	$CTDI_{100}$ per Equiv. mAs
80	8.83×10^{11}	27.0	620	0.04
120	5.57×10^{11}	19.2	130	0.15
140	5.30×10^{11}	19.0	90	0.21

A comparison between the simulated $CTDI_{100}$ normalized by the equivalent mAs of table IV.20 and the clinical $CTDI_{100}$ data of table IV.19 revealed that the simulated measurements and clinical measurements differed by approximately the same percentage between kVp settings. Specifically, the average percent difference between the clinical 80 kVp and 120 kVp $CTDI_{100}$ per mAs measurements relative to the 120 kVp measurement was 68.5%, and between 120 kVp and 140 kVp relative to the 120 kVp measurement it was 45.3%. The associated simulated percent difference in the simulated $CTDI_{100}$ per effective mAs was 73.3% between 80 kVp and 120 kVp, and 40.0% between the 120 kVp and 140 kVp. Since the percent difference measurements

appeared to be similar between the simulated and measured $CTDI_{100}$, it was reasonable to relate the simulated CSCT techniques to clinical scanner techniques through $CTDI_{100}$ measurements.

Discussion

The experiments in this chapter illustrate how various parameters affect CSCT image quality and dose deposition. Although the experiments were all simulation based with no identical associated laboratory experiments for confirming simulation results, it is reasonable to assume that similar results would be obtained by laboratory experiments, since it was shown in Chapter II that EGS5 properly modeled coherent scatter in the diagnostic mammography energy range, and, in this chapter, that the percent difference in $CTDI_{100}$/mAs measurements between different kVp's were approximately the same for the simulated and clinical scanner.

Low-contrast detectability is one of the hallmarks of traditional CT. In comparison, CSCT images achieve a far greater degree of image contrast between materials. For example, an inspection of table IV.8 shows that for 120 kVp and $\times 100$ at a 1.7° scatter angle, fat contrast is 1.94 and muscle is 0.39 for a total difference of 1.55. The same difference in contrast between fat and muscle for the 120 kVp attenuation-based image is only 0.13. The CSCT images has 11.9 time more contrast between fat and muscle than does the traditional CT.

CSCT also allows for creating composite images that possess different weights of the CSCT images. Any number of images in figure IV.13 can be processed and combined to create additional images. For example, figure IV.19 shows a simple manipulation of fat contrast in the 80 kVp image set: by subtracting from the 3.0° image the 7.4° image times the ratio of the water regions of the two images, a high-contrast fat image is produced. Table IV.21 compares the image metrics of the output composite image against its input images. The table shows that that the contrast for

each of the materials increased dramatically over the input FBP CSCT images. This method can be used to combine any number of CSCT images together, including those produced from different spectra (e.g., 80 kVp and 120 kVp), to generate composite images with enhanced contrast characteristics.

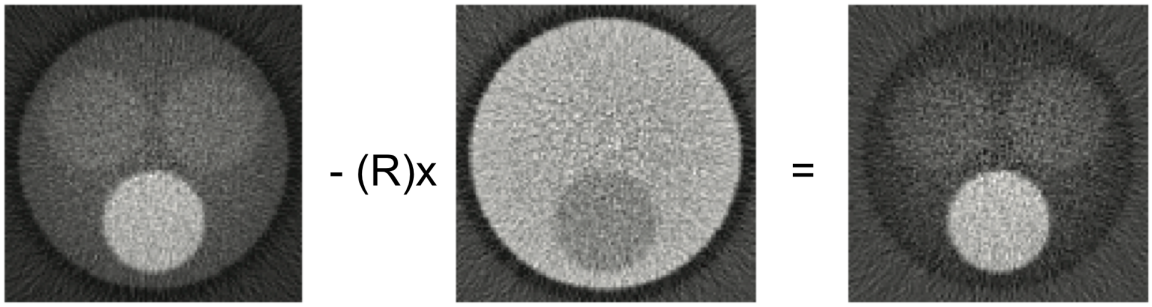

Figure IV.19: Composite image fat enhancement for 80 kVp. R is the ratio of the average water pixel values of the 3° image to average water pixel values in the 7.4° image.

Table IV.21: Composite image metrics of resultant image in figure IV.19 compared with 80 kVp ×100 simulation metrics in table IV.8, IV.9, IV.10.

	Contrast			CNR			SNR		
material	3.0°	7.4°	result	3.0°	7.4°	result	3.0°	7.4°	result
fat	1.65	-0.27	144.30	7.41	-2.06	7.33	9.65	5.00	6.17
muscle	0.43	-0.01	33.08	1.93	-0.09	1.68	5.47	5.81	1.39
kidney	0.45	-0.04	36.63	2.00	-0.33	1.86	5.55	6.19	1.52

CTDI

For the polyenergetic beams, although no periphery measurements were taken on the 10 cm diameter acrylic phantom, a reasonable estimate of the periphery dose was that it was equal to the central dose, since the phantom diameter was < 16 cm[20]. The $\mathrm{CTDI_{vol}}$ for this case was simply the $\mathrm{CTDI_{100}}$ measurement, since

$$\mathrm{CTDI_{weighted}} = \frac{2}{3}\mathrm{CTDI_{periphery}} + \frac{1}{3}\mathrm{CTDI_{center}}, \quad \text{(IV.4)}$$

$$\mathrm{CTDI_{vol}} = \frac{1}{\mathrm{pitch}}\mathrm{CTDI_{weighted}}, \quad \text{(IV.5)}$$

where pitch = 1 for a single axial acquisition and $CTDI_{center} = CTDI_{100}$. The American College of Radiology recommends that clinical CT scanners maintain $CTDI_{vol}$ for head techniques below 80 mGy as measured on a 16 cm acrylic phantom. As the diameter of the acrylic phantom increases, the difference between the periphery increases, and the $CTDI_{periphery}$ measurement is weighted more heavily. Since it could be assumed that the simulated $CTDI_{100} \approx CTDI_{vol}$, and all values were < 80 mGy, this indicates that the simulated techniques were within the normal operating dose ranges for traditional CT scanners. Therefore, it is plausible to conclude that doses associated with CSCT are reasonable, and that CSCT may be a viable option to explore for imaging appendage size objects that minimize attenuation of scattered photons. However, the affects of a strong attenuator like bone in an appendage would need to be studied before proceeding, as CSCT techniques may have to be adjusted, which may lead to an unacceptable bone dose for a diagnostic study.

Nonetheless, the contrast, CNR, SNR, and dose tables presented in the results section may be used to create a CSCT technique for generating a CSCT image with a certain amount of contrast and noise for a specific absorbed dose. For example, at a 3° scatter angle, the W 80 kVp $\times$100 beam deliver a dose of 90.9 mGy to the water region, had fat to water contrast of 1.65, a CNR of 7.41, and achieved a SNR 9.65 for the fat region; by comparison, the W 140 kVp $\times$100 beam used 40% fewer photons, delivered a dose of 53.5 mGy to water, had fat to water contrast of 0.33, a CNR of 1.90, and achieved a SNR of 7.04 for the fat region. The molybdenum $\times$10 beam at the same scatter angle used 59% and 180% more photons than the W 80 kVp and W 120 kVp beam, respectively, deposited more dose to the water (148 mGy) region, and produced an image with lower contrast (1.39), compared to W 80 kVp, and higher noise content (SNR = 0.86, CNR = 0.6). From this analysis it is clear that the tungsten beams are more dose efficient. A user could adjust the source flux to control the amount of noise in the image and dose delivered to the object, while the kVp could be adjusted to achieve a specific amount of contrast. When using ionizing

radiation for imaging purposes there is always a balance between dose delivered and value added information.

Conclusion

This chapter used the simulated fan-beam geometry of Chapter III to conduct a series of experiments on a 4-material phantom of medically relevant materials. The simulation geometry served as tool for analyzing the CSCT parameter space and illustrated the effects that different parameters had on CSCT image generation and dose deposition. An analysis of CSCT images generated from both monoenergetic and polyenergetic beams revealed that subject contrast remained constant with photon flux as expected, with CSCT images having more noise than the attenuation-based images. Also, for the CSCT images, subject contrast between regions tended to shift towards lower scattering angles as the photon energy increased. The effect of noise greatly influenced the quality of CSCT images as was demonstrated through CNR and SNR measurements. Generation of composite images that are mathematical combinations of various CSCT images can be used to create material specific contrast images. Increasing the photon flux resulted in lower noise for both the attenuation-based and CSCT images, and greatly enhanced resolution of the material regions in CSCT images. It is possible to optimize CSCT image metics with respect to dose by selecting an appropriate beam spectrum and source photon flux. The tungsten spectra sources used five to eight times more source photons than did the molybdenum spectrum, but deposited less dose and generated higher quality images. And, finally, a method was demonstrated for relating simulated CSCT techniques to clinic CT scanner techniques through $CTDI_{100}$, which provided a reasonable estimate of a simulations' equivalent clinical technique.

CHAPTER V

SINGLE SHOT COHERENT SCATTER COMPUTED TOMOGRAPHY (SSCSCT)

Introduction

This last chapter deals with a hypothetical CSCT reconstruction technique that is dependent upon an ideal detector that can resolve the trajectory of a photon at the moment of detection. The polyenergetic simulated data generated for the experiments conducted in Chapter IV was used to illustrate an individual photon back trajectory method for reconstructing a CSCT image. The term single shot coherent scatter computed tomography (SSCSCT) is used to describe this technique. Essentially, if it was possible to record the position and direction vectors of a photon the moment it was detected, then, hypothetically, by reversing the direction vector components of a scattered photon and determining where the reverse trajectory intersects with the fan-beam plane, it should be possible to localize where the scatter event occurred.

Currently, there are no detectors capable of measuring both the detected position of a photon and its direction vectors (momentum vectors) at time of detection. However, if one did exist, and the resolution was fine enough, then it may be possible to reconstruct a CSCT image without the use of a traditional reconstruction algorithm.

Method

For each photon detection in the polyenergetic data set (80, 120, and 140 kVp) of Chapter IV, both photon position and photon direction vectors at the time of detection were recorded. Using simple vector geometry, the trajectories of the simulated scattered photons were reversed and extended from their detection point through the fan-beam plane. The point of intersection of the line and plane mark the interaction

point for the photon. By grid addressing the intersection points into a 200x200 array and counting the number of intersection points in each bin (pixel), a tomographic CSCT image of the phantom was created. Since the detector was sensitive to all photons regardless of energy and origin, stray bremsstrahlung or multiple scattered photons were also detected; however, the back trajectory for these photons did not necessarily intersect the fan-beam plane. Any intersection points that fell outside of the support region where the phantom was located were eventually rejected from the final reconstruction. Figure V.1 illustrates the intersection of the reverse trajectory of the scatted photons with the fan-beam plane.

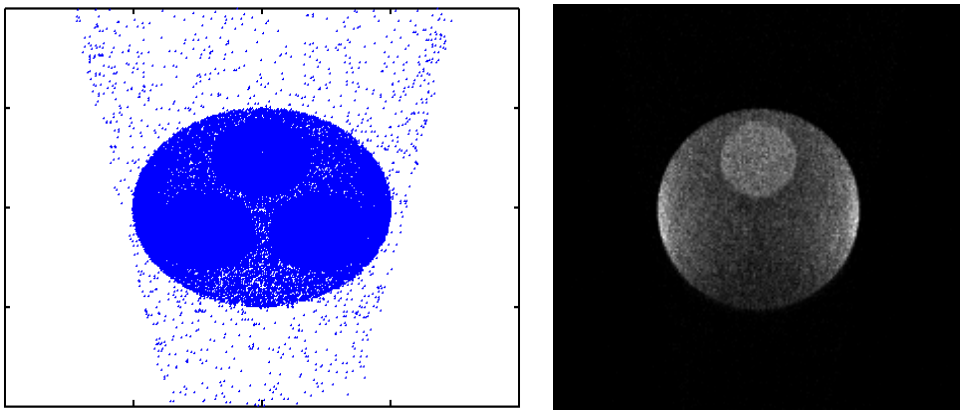

(a) Snapshot of reverse photon trajectory intersections with the fan-beam plane for a single view angle.

(b) Image of reverse trajectory scatter data: 120 kVp at 2.3° scatter angle. High intensity areas on the periphery are due to the higher detected scatter from the surface.

Figure V.1: Example of back trajectory reconstruction for a single view angle (1 of 128) for 120 kVp at a scatter angle of 2.3°.

The 128 view angles comprised a set of 64 pairs of 180° opposing view angles. A single composite image was formed by taking the geometric mean of the 128 images, which produced a lower dishing effect (reduction in signal located towards the center of the object) compared to an arithmetic mean; an example result is shown in figure V.2(a).

To account for a lower number of photons emanating from the central portion of the phantom due to attenuation of the scattered photons, a Chang correction was applied

to increase the signal from the central region. The Chang correction is used in nuclear medicine as a first order attenuation correction technique for single photon computed tomography (SPECT), and is commonly used for SPECT brain and abdomen imaging [8]. The technique calculates an average attenuation correction factor (ACF) at each pixel location (x, y), and then divides by the ACF to correct the image. First, an initial image $f(x, y)'$ is reconstructed without any attenuation correction. Then the contours of the image are used to estimate the attenuation path length from each location within the object to its boundaries. A constant linear attenuation coefficient is used for each path length. The ACF is calculated as

$$\mathrm{ACF}(x, y) = \frac{1}{\frac{1}{N}\sum_{i=1}^{N} e^{-\mu d_i}}, \tag{V.1}$$

where d_i is the attenuation path length for location (x, y) for the i^{th} sampling angle and μ is an assumed constant linear attenuation factor. The reconstructed image is corrected by $f(x, y)' \times \mathrm{ACF}(x, y)$ to yield the attenuation corrected image, $f(x, y)$. Figure V.2 shows an example of ACF application.

Circular ROIs, with a diameter of 14 pixels, were used to sample the reconstructed SSCSCT images in each of the material regions in order to calculate the image contrast, CNR, and SNR – similar to the procedure used in Chapter IV.

Results

Figure V.3 shows the results of the SSCSCT reconstructions. Tables V.1, V.2, and V.3 contain simulation measurements for the images in figure V.3 images. For the 80 and 120 kVp 1.7° reconstructions, there were noticeable locations where the pixel values were either zero, or considerably lower than the surrounding pixels. Since the phantom contained no voids, these holes indicated an absence of back trajectory intersections with the fan-beam plane at those locations. This could result from an absence of detected scatter photons originating from that location due to absorption

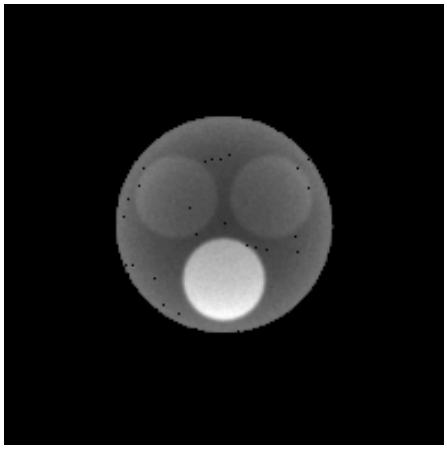

(a) Uncorrected image $f(x,y)'$

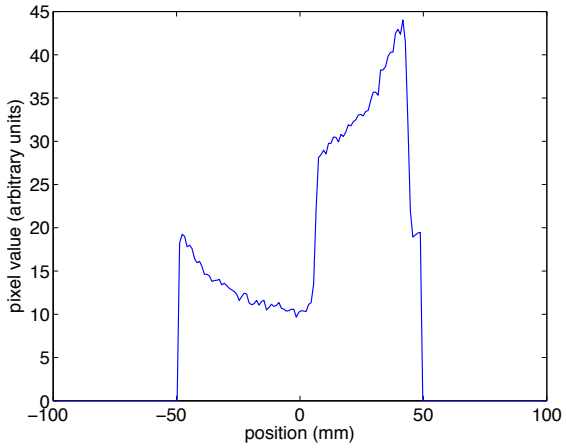

(b) Vertical line profile through uncorrected image $f(x,y)'$

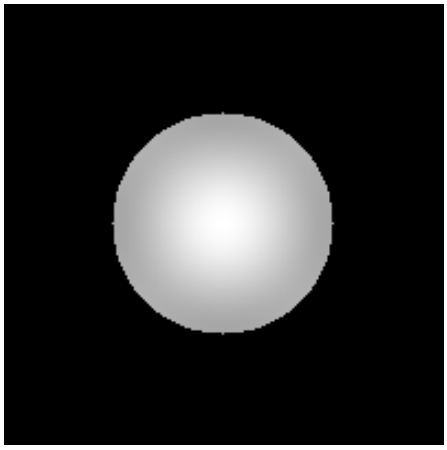

(c) ACF(x,y) map

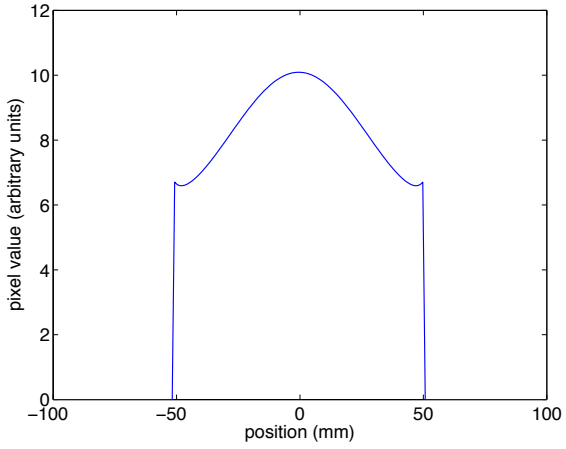

(d) Vertical line profile through ACF(x,y) map

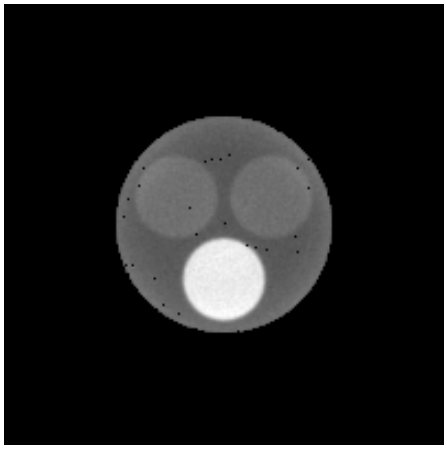

(e) Corrected image $f(x,y)$

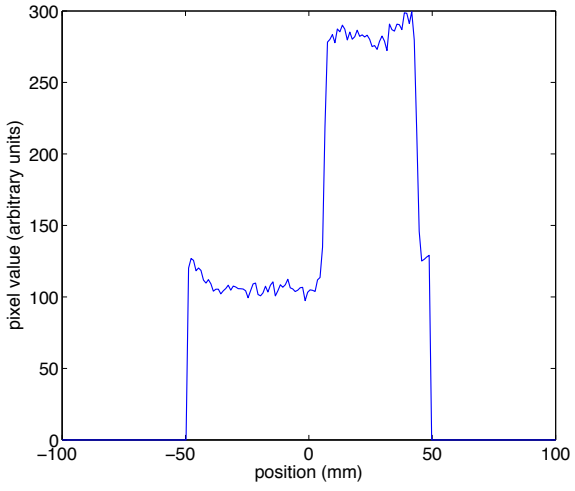

(f) Vertical line profile through corrected image $f(x,y)$

Figure V.2: Example of ACF applied to data for 120 kVp and scatter angle 1.7°.

or scatter as they traveled towards the detector, or a lack of source photons reaching that particular region to begin with. It could also be due to the finite precision of the computer to calculate intersection points, which could result in a point being incorrectly addressed into another bin for counting.

Over all, the most noticeable difference between the SSCSCT images (figure V.3) and the FBP CSCT images of Chapter IV (figure IV.13) was the reduction in noise. This was confirmed by all SNR comparison ratios being > 1.0 (table V.4). Assuming Poisson statistics applied, all simulation measurements in table V.1 were within roughly one standard deviation of the contrast simulation measurements in table IV.8 for the FPB CSCT images of Chapter IV, which indicated that noise in the FBP CSCT images was likely the major contributor to any difference seen in the contrast simulation measurements. Additionally, the SSCSCT CNR simulation measurements (table V.2) were greater than the associated FBP CSCT CNR simulation measurements (table IV.9) for all but seven points; and for those points, it was within one standard deviation of the FBP CSCT CNR simulation measurements, assuming Poisson statistics.

In emission computed tomography, the linear attenuation coefficient of water selected for use in the ACF is typically selected based on the principle energy of the emission photons. The effective energies for the 80, 120, and 140 kVp beams were 46, 60, and 66 keV, which correspond to water linear attenuation coefficients of 0.238, 0.203, and 0.196 cm^{-1}, respectively. However, it was necessary to use attenuation coefficients that were 2.3 times higher in order to correct for the lower signal from the central region of the phantom. This indicated the ACF, which only corrected for attenuation of scattered photons from the scattering region to the detector, was insufficient. Another correction must be applied to account for the attenuation of source photons to the central regions, which contributed to lower scatter interactions in the central portion of the phantom. Also, the increase in the linear attenuation coefficient used in the ACF resulted in a radial gradient in the SSCSCT images with higher pixel

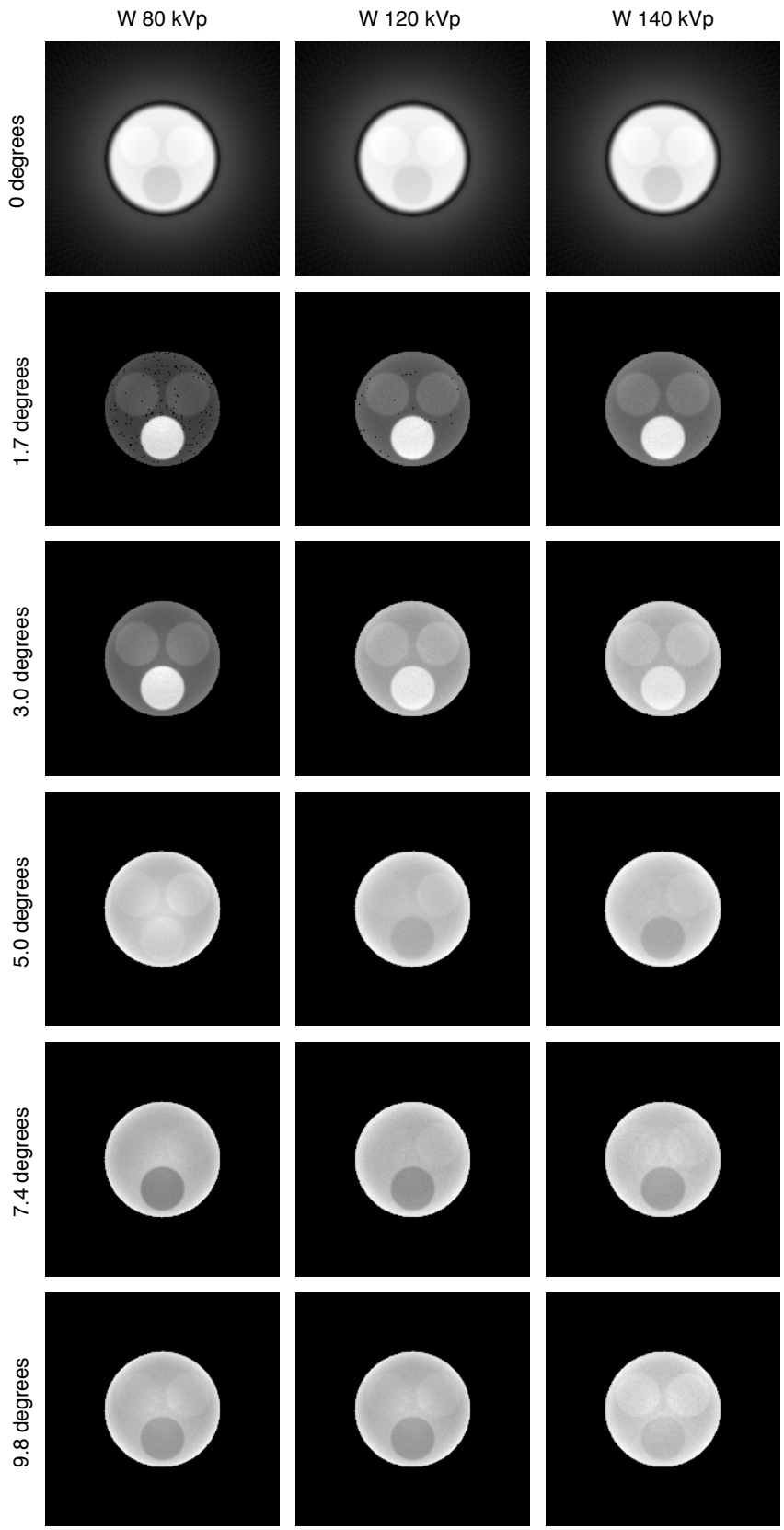

Figure V.3: SSCSCT reconstructed images from a polyenergetic source.

Table V.1: SSCSCT Contrast for phantom #2 - tungsten spectra: 80, 120, 140 kVp; 128 view angles; ×100 data set. θ = scatter angle. The 0° image is the FBP attenuation based image.

	$W80\ kVp$			$W120\ kVp$			$W140\ kVp$		
θ	fat	$muscle$	$kidney$	fat	$muscle$	$kidney$	fat	$muscle$	$kidney$
0	-0.11	0.04	0.04	-0.09	0.04	0.04	-0.08	0.04	0.04
1.7	2.60	0.39	0.35	1.61	0.24	0.21	1.26	0.18	0.16
3.0	1.27	0.23	0.21	0.43	0.08	0.08	0.26	0.04	0.05
5.0	0.08	0.03	0.05	-0.11	-0.02	0.00	-0.15	-0.03	-0.01
7.4	-0.25	-0.03	-0.01	-0.22	-0.03	-0.02	-0.17	0.02	0.03
9.8	-0.14	0.01	0.02	-0.11	0.02	0.02	-0.06	0.05	0.06

Table V.2: SSCSCT CNR for phantom #2 - tungsten spectra: 80, 120, 140 kVp; 128 view angles; ×100 data set. θ = scatter angle. The 0° image is the FBP attenuation based image.

	$W80\ kVp$			$W120\ kVp$			$W140\ kVp$		
θ	fat	$muscle$	$kidney$	fat	$muscle$	$kidney$	fat	$muscle$	$kidney$
0	-18.68	7.01	6.89	-23.10	11.28	11.05	-25.82	13.91	13.58
1.7	12.53	1.88	1.67	19.69	2.91	2.56	34.65	4.86	4.31
3.0	40.18	7.13	6.76	12.44	2.25	2.44	7.62	1.14	1.44
5.0	3.21	1.26	2.01	-3.12	-0.59	-0.04	-4.47	-0.92	-0.41
7.4	-8.09	-1.06	-0.20	-5.49	-0.84	-0.45	-6.30	0.56	1.12
9.8	-4.71	0.35	0.77	-2.65	0.38	0.41	-2.49	2.09	2.36

Table V.3: SSCSCT SNR for phantom #2 - tungsten spectra: 80, 120, 140 kVp; 128 view angles; ×100 data set. θ = scatter angle. The 0° image is the FBP attenuation based image.

	$W80\ kVp$			$W120\ kVp$			$W140\ kVp$		
θ	fat	$muscle$	$kidney$	fat	$muscle$	$kidney$	fat	$muscle$	$kidney$
0	463.75	371.27	366.40	505.98	489.54	489.94	545.83	526.44	521.30
1.7	45.63	32.82	34.05	59.41	39.45	43.92	61.25	43.35	45.88
3.0	51.67	41.92	39.12	60.75	60.10	56.44	57.36	57.26	61.99
5.0	68.41	68.69	50.97	67.32	73.18	80.38	64.29	60.91	76.15
7.4	63.52	62.68	51.25	47.38	50.46	51.24	44.36	39.76	47.19
9.8	53.56	56.29	49.24	50.01	49.57	57.52	52.98	55.31	52.96

Table V.4: Ratio of SNR simulation measurements between SSCSCT to FBP CSCT ×100 data of Chapter IV table IV.10.

	$W80\ kVp$			$W120\ kVp$			$W140\ kVp$		
θ	fat	$muscle$	$kidney$	fat	$muscle$	$kidney$	fat	$muscle$	$kidney$
1.7	7.24	10.16	9.90	9.21	11.88	12.34	8.63	12.71	12.60
3.0	5.35	7.66	7.05	8.47	10.56	9.07	8.15	10.17	10.31
5.0	8.11	7.01	5.22	10.15	9.85	11.24	10.24	8.11	9.98
7.4	12.70	10.79	8.28	10.94	9.93	9.72	9.95	8.25	9.93
9.8	10.24	9.69	8.84	9.67	9.16	10.67	10.88	10.80	10.36

values located towards the central region. Thus, the reconstruction method appears to require two attenuation correction factors in order to account for loss of signal from the central region of the phantom.

Discussion

Although the reconstruction method described above was for a hypothetical situation in which a detector, or set of detectors, was able to determine the trajectory of a scattered photon upon detection, it does raise some interesting points. An inspection of figure V.3 and table V.4 illustrated that the SSCSCT images had SNRs that were on par with the FBP CSCT images, but generally possessed greater CNRs than the CSCT images; thus, the material regions were more distinguishable than in the CSCT images. Also, data from a single view angle acquisition can be used to create a single tomogram (figure V.1(b)), whereas traditional fan-beam CT requires an arc rotation of no less than 180° plus the fan angle.[1] It is possible that a single shot scatter acquisition system could be made portable, and could be used for imaging objects that are unable to be transported to a traditional CT scanner (e.g., bed ridden patients, stationary objects, infected lab animals). Also, a single shot scatter tomograph would deliver less dose to the imaged object than a CT image.

Potential system designs may incorporate a two position detector – one located closer to the object and another, or the same detector located a further distance away. It may be possible to statistically determine trajectory information from a pair or series of detected photon distributions from two or more exposures on the same stationary object with detectors at different distances from the object. For a traditional CT source, the detectors would have to possess a fast recovery time to capture and correlation the incoming photons. However, it may be the case that only

[1]It may be possible to create CSCT images from only 180° of data, however, this was not explored in this work.

a fraction of the scattered photons need be detected. A potential detector component could be cadmium zinc telluride (CZT) detectors.

CZT detectors possess some ideal characteristics for photon detection, to include high Z (50), low band gap energy (1.5eV), room temperature operations, and high resolution spectroscopy[53]. The detectors can be manufactured down to 2.5x2.5 mm^2 elements and have been used to investigate mammography imaging through scintimammography[38]. The fact that they are simultaneously both position sensitive and have energy resolving capability may allow potential CSCT or a SSCSCT system to reconstruction images using only selected photons based on their energy. Also, knowing the energy of a detected photon may aid in determining the region from where it was scattered, since each detector element subtends a certain field of view of the object and the photon scatter angle is energy and material dependent. Area of overlap may be formed to localize where the scatter event occurred. Reference [40] lists other scintillation x-ray detection materials that may be of use.

The SSCSCT reconstruction method currently is technology limited. However, SSCSCT images can be used in an identical manner as the FPB CSCT images of Chapter IV. Specifically, composite or material specific images could be formed from a weighed combination of the various scatter angle images, whether derived from scatter position, scatter photon energy, or a combination of both, so long as photon trajectory information at the time of detection is acquired. A combination of SSCSCT images and FBP CSCT images could also be combined to provide additional information to enhance a tomogram.

Conclusion

The method described in this section illustrated a reconstruction method for creating scatter generated tomograms by utilizing the reverse trajectory of a detected scatter photon. The method is purely hypothetical, as no detection system currently

exists can simultaneously detect and determine the exact trajectory of indirectly ionizing radiation (photons) at diagnostic energies. However, potential advantages exist if it does become possible to obtain this type of precision measurement of scattered photons, such as the creation of a tomogram from scattered photons for a single acquisition view angle, and composite image generation for creating material specific scatter images, as in FBP CSCT.

CHAPTER VI

SUMMARY OF RESULTS

The goal of this work was to explore the parameter space for CSCT image generation. The manner in which this was accomplished was through the use of Monte Carlo simulations of a CSCT system.

The ability of the EGS5 Monte Carlo code system to simulate coherent scatter was investigated and shown to be valid for mammography energies (< 32 kVp) – EGS5 simulated scatter generated in a pencil-beam geometry for beef fat, beef muscle, and water produced scatter profiles that were in agreement with laboratory measurements.

A simulated pencil-beam geometry was extended to create a discrete fan-beam geometry, thus mimicking current CT scanners with area wide detectors. This geometry also had the the added benefit of not detecting any lateral forward scatter from extended regions of the phantom to reach the detector elements that were not in-line with a source photon's original trajectory from source to the detector. Both monoenertic and polyenergetic spectra were used to create simulated scatter data for performing CSCT reconstructions. Reconstructions were carried out using FBP methods per Harding's and Westmore's formulations, which permitted the use of FBP with a few underlying assumptions. Results from the polyenergetic simulations (anodes: tungsten and molybdenum) were used to demonstrate that composite images can be formed from multiple images, at various angles and energies, to create material specific images. A $CTDI_{100}$ dose comparison between the simulated polyenergetic techniques and a clinic CT scanner were performed in order to associate the simulated source parameters to an equivalent clinical CT technique. Also, through $CTDI_{100}$ measurements, it was estimated that the simulated polyenergetic techniques had a $CTDI_{vol} < 80$ mGy, and were therefore dose feasible for at least a 7.5 mm beam width or collimator thickness. A look at the dose tables in Chapter IV show that the

simulated dose deposited in the various material regions were also less than 80 mGy for all beams except the $\times 10$ Mo 32 kVp spectra. The various image metric and dose tables in Chapter IV also illustrate which source parameter to adjust to achieve the desired amount of image contrast and noise.

Future investigations could expand on this work by experimentally verifying that EGS5 does model coherent scatter properly for polyenergetic spectra > 32 kVp. Also a more realistic detection system could be modeled which takes into account lateral scatter and other elements that degrade signal detections to further investigate how CSCT image quality is influenced by off-axis scatter and noise. With regards to the SSCSCT reconstruction method, a more extensive investigation into an attenuation correction factor that incorporates both primary beam attenuation as well as scatter photon attenuation.

Since this work only investigated soft tissue with relatively moderate attenuation properties compared to bone, a thorough investigation into how highly attenuating objects affect CSCT images and dose deposited would be beneficial. It could be that CSCT is limited to small diameter objects composed primarily of soft tissue. In that case, it is possible that CSCT imaging could find a use in small animal imaging research or breast imaging. For any imaging study, dose is a concern, and any future CSCT study should contain a thorough review of potential benefits of the images produced versus the risk associated with the dose for the examination. As mentioned in the "historical contributions to CSCT research" in Appendix A, there are researchers who have created libraries of medically relevant coherent scatter form factors of healthy and diseased tissues. For small animal imaging, CSCT may potentially provide another tool to assist in identifying and analyzing induced pathologies such as specific types of cancers.

APPENDIX A

HISTORICAL CONTRIBUTIONS TO CSCT RESEARCH

What follows is a brief summary of the research that has advanced the field of coherent scatter computed tomography. The discussion is not intended to be an inclusive list of all research conducted in the field, but instead is designed to provide a framework for referencing other works. Essentially, these contributions can be separated into two broad categories: material investigation and image generation. A succinct perspective of research conducted up to 1999 is summarized by Harding (1999)[17].

In 1895, Wilhelm Conrad Röntgen, winner of the first Nobel Prize in Physics in 1901, discovered x-rays and launched the field of planar radiography. The field of coherent scatter x-ray research can draw its linage primarily back to Max Von Laue, a German physicist who won the 1914 Noble Prize in Physics for his observations of interference patterns produced by transmitted x-rays through crystalline materials. His discovery in turn lead to William Henry Bragg and his son, William Lawrence Bragg, the discoverer of the Bragg law of X-ray diffraction, winning the 1915 Nobel Prize in Physics for their work in solving the inverse problem of determining crystal structure from images produced by coherently scattered photons. From that time forward, the field of x-ray material analysis and x-ray planar imaging essentially developed separately.

It wasn't until after the invention of Computed Tomography (CT) in 1971 by Godfrey Houndsfield and Allen Cormack, both co-winners of the 1979 Nobel Prize for Physiology or Medicine, did a detailed study of how scattered x-rays, which produced streaking artifacts in CT images, begin to take shape[17]. It had been known since the early days of planar radiography that scattered photons degraded image contrast, hence the use of anti-scatter grids on film cassettes. The degree to which coherent

scatter contributed to image degradation had not begun to be quantified until the early 1980's.

In 1982, Johns and Yaffe definitively illustrated the effects of coherent scatter in radiography. They showed that molecular form factors calculated from a weighted sum of atomic form factors for hydrogen and oxygen failed to match experimentally measured molecular from factors for liquid water, thus demonstrating the degree to which intermolecular coherence effects x-ray scattering from liquid water.[1] Additionally, they quantitatively demonstrated that for a typical radiographic abdominal scan, first coherent scatter photons comprises up to 26% of the primary exit fluence[23]. At high diagnostic energies, first coherent scatter is highly forward peaked and diverges very little compared to other scatter, thus making it more difficult to remove before being detected, which leads to images with lower image contrast and CNR.

In 1985, Neitzel, Kosnaetzky, and Harding performed a Monte Carlo simulation study utilizing tabulated molecular form factor data for liquid water compiled by Morin (1982). The simulation produced scatter profiles for a mono-energetic 60 keV and poly-energetic 140 kVp pencil beam incident on 10 cm of water. Their calculations indicated that coherently scattered photons dominate the scatter in the neighborhood of the transmitted radiation beam. Building on their previous work two years earlier, the trio described a technique called x-ray diffraction computed tomography (XRDCT), in which the coherent scattering properties of a material can be exploited to generate a tomogram of an object. This study used a first generation CT acquisition geometry (pencil-beam source with step-and-shoot translation) with a quasihexagonal array of 61 1x1cm^2 bismuth germinate (BGO) scintillator coupled to photomultiplier tubes to detected scattered photons, from which tomograms of varying contrast were reconstructed[16]. For amorphous materials, the coherent scatter

[1]It should be mentioned that by the early 1980's, physicists had compiled libraries of calculated atomic and measured molecular coherent scatter form factors primarily for validating theoretical models and for use in crystallography. Major contributors to these libraries include Hubbell, Narten, Levy, Morin, Roy, Kissel and Pratt.

is isotropic and produces an annular scatter pattern centered on the primary beam. For their experimental set up, they identified three principle factors contributing to momentum resolution in XRDCT: 1) detector spatial resolution; 2) polychromatic x-ray source (energy spread); and 3) the size of the region an object subtends at the detector. Since the angle (θ) of photon scatter detection can be correlated with a momentum transfer argument (x), it is customary to see scatter profile plots with either x or θ on the abscissa versus a measurement of detected intensity along the ordinate. The invention of modern solid-state detectors with sub millimeter size detection elements have mitigated the effect of factors 1 and 3; however, the polychromaticity of the x-ray source still leads to a blurring of the annular scatter pattern, with the amount of blurring linearly proportional to the distance between the detector element and the center of the detector.

By the 1990's, various researchers had created new ways to process the scatter data in order to synthesize material-specific images, while other experimentalists measured the molecular form factors of a variety of medically relevant materials. Westmore (1996), Fenster, and Cunningham created a prototype imaging system that used a polychromatic pencil beam source and an image intensifier as the detector. They expanded the reconstruction of material-specific images by decomposing radial profiles on a pixel-by-pixel basis using known diffraction patterns from homogeneous materials. A non-negative least squares fitting algorithm was used to minimize the difference between the measured cross section at a particular detector location for a multi-material phantom and the cross sections at the same detector location for single materials[60].

On the material analysis front, Peplow and Verghese (1998) produced data tables of measured molecular form factors for various animal tissues. A portion of this data set is incorporated into the EGS5 distribution to provide the Monte Carlo system with the ability to properly model coherent scatter interference. Peplows and Verghheses molecular form factor data set include measurements for lucite, lexan, kapton,

formaline, water, breast tissue, and fat, muscle, liver, kidney, heart muscle for both pork and beef. A beam line at the National Synchrotron light source at Brookhaven National Laboratory was used to irradiate their samples with two different energies, 8 and 70 keV, which corresponded to two momentum transfer range, x = 0.056 to 3.2 nm^{-1}, and x = 0.14 to 13 nm^{-1}, respectively[42].

Also in 1998, Kleuker et al. conducted a feasibility study on soft-tissue imaging using x-ray diffraction computed tomography (XRDCT). His group used a 60 and 80 keV beam line at the European Synchrotron Radiation Facility to interrogate a pork chop and reconstruct tissue-selective image from wide-angle diffracted photons. The tissue-selective image produced by the mono-energtic x-ray source produced images with high tissue contrast[28].

Continuing into the early 2000's, researchers Schomka (2000), Schneider (2001), and Harding, at Philips research laboratories in Germany, modeled and experimentally verified the feasibility of a prototype CSCT system which used a fan beam x-ray source in a third generation CT geometry[51, 52]. This was a significant step forward in reducing the scan time in CSCT over the first generation (step-and-shoot) geometry. Additionally, Schlomka (2004) when on to demonstrate the feasibility of incorporating an energy-resolving detector into the third generation geometry, allowing increased momentum transfer (scatter angle) resolution due energy discrimination when using poly-chromatic sources[50].

In 2002, Poletti et al. (2002) investigated photon scatter from human breast tissue (adipose and glandular) and from mammographic breast-equivalent materials: water, polymethylmethacrylate (PMMA), nylon, PE, nylon, and four commercial breast-equivalent materials. For the commercial breast materials, three samples from Computerized Imaging Reference System, Inc. (CIRS) with different glandular content were selected, and one sample from Radiation Measurements Inc. (RMI). The radiation source was a 17.4 keV beam produced from a powder diffractometer operating in transmission mode. For photon scatter less than 25 degrees, Poletti demonstrated

that 1) scatter from breast tissue differed from scatter by breast-equivalent materials; 2) scatter from adipose tissue was similar to scatter from commercial breast-equivalent material; and 3) glandular tissue scattered similar to water. Data generated by this investigation can be used to model elastic scattering from breast tissue in Monte Carlo programs.

Johns and Wismayer (2004) conducted coherent scatter experiments to measure the molecular form factors of PMMA polystyrene, lexan, nylon, polyethylene, beef muscle, and water utilizing the Rigaku and Scintag powder diffractometers, and compared their results to previously published tables. They concluded that, although well suited for samples with sharp Bragg peaks, powder diffractometers are not well suited to handle amorphous materials

By 2005, Batchelar, Davidson, Dabrowski, and Cunningham demonstrated the first quantitative use of CSCT by analyzing excised bone samples. A first generation pencil-beam geometry setup, similar to Westmore, was used to demonstrate how CSCT could be used for tomographic densitometry. A year later, Davidson expanded this technique to perform ex-vivo non-destructive analysis on intact urinary calculi. The images generated were essentially mineral composition maps, which could aid in recommending preventative measures since mineral spatial composition is an indicator of the etiological process for non-calcium stones[9].

Lastly, King (2010, 2011) and Johns used a poly-chromatic source and an energy-sensitive detector to develop an energy-dispersive technique to measure the coherent molecular form factor for amorphous materials. Their measurements were in close agreement with previously published data, and further confirmed the limitations diffractometer based systems[25]. In collaboration with Landheer, the researchers compiled a form factor library of medically relevant (fat, muscle, liver, kidney, bone, and water) and phantom relevant (polyethylene, polystyrene, polycarbonate (lexan) and nylon) materials[26].

APPENDIX B

PHYSICAL PRINCIPLES OF COHERENT SCATTER

This section explains the physical principles underlying molecular coherent scatter starting with the simplest form of coherent scatter – photon coherent scatter by a free electron. The significance of the form factor is discussed and how it modifies the Thomson differential scattering cross section in order to determine the Rayleigh (coherent) differential scattering cross section for an atom/molecule.

Thompson Scatter - classical scattering from a single free electron

The scattering of an electromagnetic wave by a free electron was first analyzed in terms of classical electromagnetic theory by J.J. Thomson. In his analysis, an incident electromagnetic wave exerts a Coulombic driving force on an initially stationary free electron. The incoming oscillating electric field causes the electron to experience acceleration oscillations, thus causing it to radiate electromagnetic radiation isotropically at the same frequency as the incoming EM wave. Since the incoming and outgoing EM wave are of the same frequency, no energy is lost and the interaction can be classified as an elastic interaction. For an unpolarized incident radiation, Thomson determined the electronic differential scattering cross section per unit solid angle $(d\sigma/d\Omega)_T$ to be

$$\left(\frac{d\sigma}{d\Omega}\right)_T = \frac{r_e^2}{2}(1+\cos^2\theta), \tag{B.1}$$

where r_e is the classical electron radius and θ is the photon scattering angle.

Writing equation B.1 in terms of θ gives the Thomson differential scattering cross

section per unit scattering angle $(d\sigma/d\theta)_T$:

$$\left(\frac{d\sigma}{d\theta}\right)_T = \frac{r_e^2}{2}(1+\cos^2\theta)2\pi\sin(\theta) = \pi r_e^2(1+\cos^2\theta)\sin(\theta). \tag{B.2}$$

Figure B.1 shows the two differential cross sections plotted as a function of scattering angle θ. Integrating equation B.2 over all scattering angles yields the total Thomson

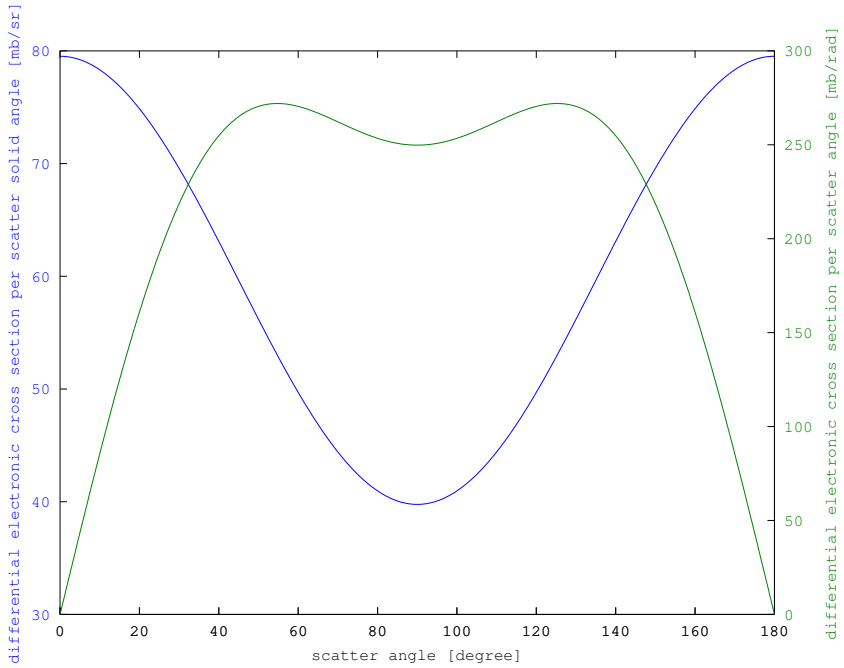

Figure B.1: Plot of the Thomson differential cross section per unit solid angle $(d\sigma/d\Omega)_T$ and the differential cross section per unit angle $(d\sigma/d\theta)_T$, as a function of photon scatter angle. Units are in milli-barns per sr and rad, respectively.

cross section for a free electron for all photon energies ($\sigma_T = 8/3\pi r_e^2 = 66.53 \times 10^{-30} m^2$). σ_T has the same value for all photon energies, however, this is only correct for very low energies where the binding energy is insignificant. As the incoming photon increases, an electron will recoil, and the amount of scattered radiation will be less.

Rayleigh Scatter and Form Factors - coherent scatter from multiple electrons

Rayleigh scattering extends the concept of elastic photon scattering by a stationary free electron to elastic scatter from a group of bound electrons in an atom through use of the atomic form factor approximation. The form factor approximation satisfactorily describes the scattering differential cross section for x-ray photons with energies greater than the ionization thresholds of the atomic shells[19]. Atomic coherent form factors $F_a^2(x, Z)$ table have been calculated by Hubbell[21] using various quantum mechanical models and approximations to atomic wave functions (e.g., Hartree–Fock, Thomas–Fermi, or Hartree models), since only form factors for the Hydrogen atom can be solved analytically[43].

The approximation allows the differential atomic cross section for Rayleigh (coherent) scatter to be written as:

$$\left(\frac{d\sigma}{d\Omega}\right)_{coh,a} = \left(\frac{d\sigma}{d\Omega}\right)_T F_a^2(x, Z), \tag{B.3}$$

where $x = \sin(\theta/2)/\lambda$ is the momentum transfer argument, which has units of inverse length. Extending the Thompson differential scattering cross section to atoms amounts to just multiplying eqn B.1 by $F_a^2(x, Z)$.

For investigating the form factors for molecules, researchers conduct scatter experiments and measure the amount of scatter per differential angle or solid angle[42, 24, 29, 30]. From these measurements, the molecular coherent form factor $F^2(x)_{coh,mol}$ is calculated from the equation

$$\left(\frac{d\sigma}{d\theta}\right)_{coh,mol} = \left(\frac{d\sigma}{d\Omega}\right)_T F_{mol}^2(x). \tag{B.4}$$

This method preserves the intra- and inter-atomic electron coherent scattering interference effects, which allows them to be used in calculations to predict a photon's

probability to undergo coherent scatter and its probable scattering angle (e.g., in Monte Carlo programs). Other researchers have calculated molecular form factors by applying an oscillatory factor s(x),which takes into account interactions between atoms[31], to the free-atom model version of the form factor calculated from the independent atomic model (IAM):

$$F_{mol}^2(x) = W \sum_i \frac{w_i}{A_i} F_a^2(x, Z_i)\mathrm{s}(x). \tag{B.5}$$

where W is the molecular weight, w_i is the mass fraction for element i, and A_i and Z_i are the atomic mass and the atomic number of element i, respectively.

The form factors modify the $d\sigma/d\theta_T$ and cause the coherent scatter photon distribution to be skewed towards lower scatter angles. Figure B.2 shows the form factor for water used in EGS5 over the momentum transfers over the range where coherent scatter effects significantly influences the scatter angle distribution.

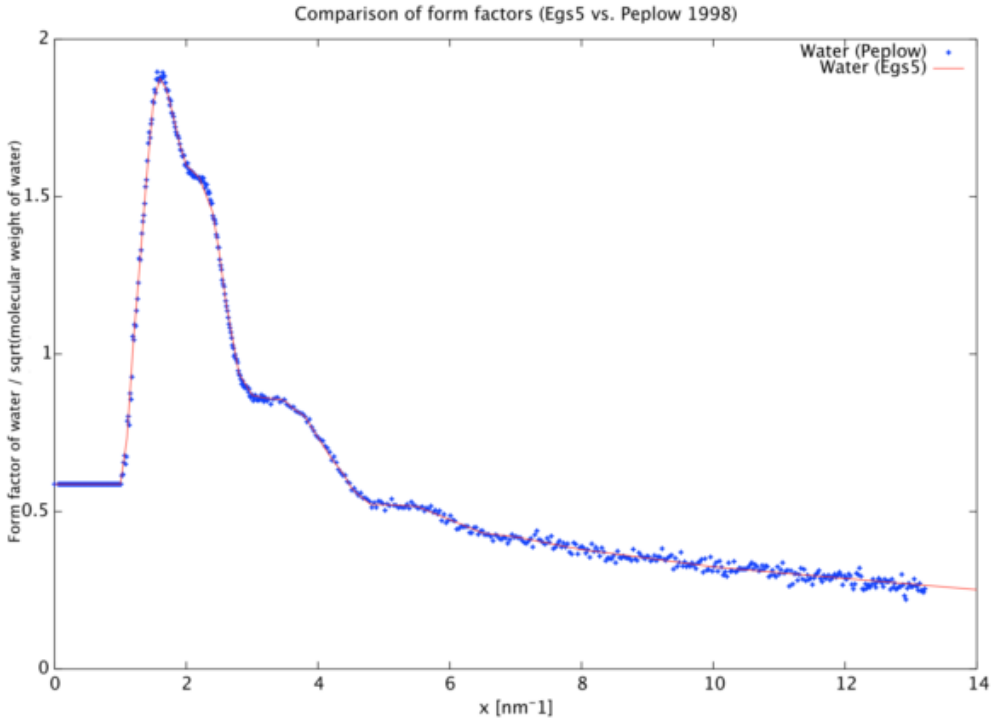

Figure B.2: Plot of the coherent form factors for water provided EGS5 and from reference [42].

Compton Scatter - incoherent scatter

In a Compton interaction energy is transferred from an incident photon to a loosely bound electron, which recoils from the collision. The equation for the differential incoherent scattering cross section is

$$\left(\frac{d\sigma}{d\Omega}\right)_{incoh,a} = \left(\frac{d\sigma}{d\Omega}\right)_{\mathrm{KN}} S_a(x), \tag{B.6}$$

$$\left(\frac{d\sigma}{d\Omega}\right)_{\mathrm{KN}} = \left(\frac{d\sigma}{d\Omega}\right)_{T} F_{\mathrm{KN}}, \tag{B.7}$$

where $(d\sigma/d\Omega)_{\mathrm{KN}}$ is the differential Klein-Nishina electronic cross section per electron per unit solid angle for the Compton effect, $S_a(x)$ is the atomic incoherent scattering function, and F_{KN} is the Klein-Nishina form factor, which is dependent on incident photon energy and the photon scattering angle. Hubbell[21] has generated an extensive table of incoherent scattering functions. References [21] and [43] contain a good description of Compton scatter and the details of the Klein-Hishina form factor.

Figure B.3 illustrates the impact that coherent scatter has at low scatter angles compared to incoherent scatter. The plots shows that incoherent scatter is relatively uniform over the scatter angles sampled and is contributes only insignificantly to the scatter signal at low scatter angles. However, as the scatter angle increases, incoherent scatter contributes a greater amount to the total scatter signal.

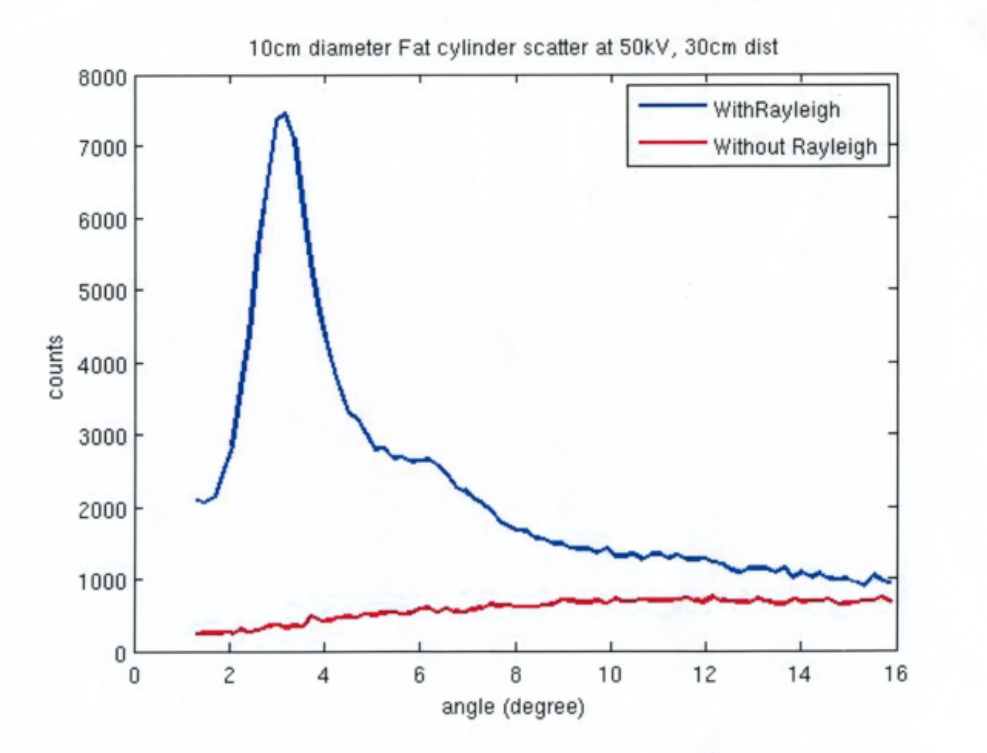

Figure B.3: Result of simulated scatter detections in EGS5 with coherent scatter modeling activated and de-activated.

APPENDIX C

$CTDI_{100}$

In computed tomography, a dose gradient exists in both the radial and z-axis direction for the object being scanned. For a 32 cm diameter cylindrical acrylic phantom, the radial component of dose is highest near the surface and lowest towards the object center. As the radius of the phantom decreases (i.e., 16 cm or lower) the radial dose distribution tend to become more uniform[20]. The variation in the z-axis direction is illustrated in figure C.1 for a hypothetical non-helical multiple slice acquisition.

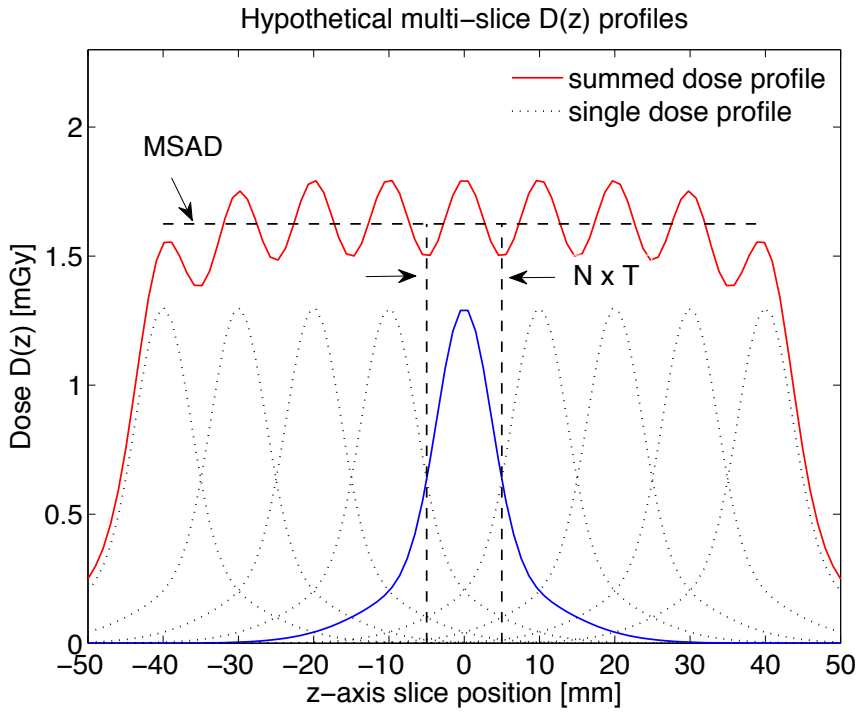

Figure C.1: Z-axis dose profile for multiple axial scans. N×T = beam width dimension. The rectangular area (MSAD×NT) is equal to the integrated dose under a single dose profile.

The multiple scan average dose (MSAD) is the average dose to the central slice from both the primary radiation and and scattered radiation from adjacent contiguous

scanned sections[36]. For axial only scans, where the table increment is equal to nominal beam width, the computed tomography dose index (CTDI) is an estimate of the MSAD[35], since CTDI is the product of the MSAD and(NT) divided by (NT). CTDI is also more convent to measure than MSAD.

The accumulated multiple scan dose at the center of a 100-mm scan is called the CTDI_{100}:

$$\mathrm{CTDI}_{100} = \frac{1}{NT}\int_{-50mm}^{50mm} D(z)dz, \tag{C.1}$$

where $D(z)$ is the dose dose deposited at location z.

Since CTDI_{100} is measured using a pencil ionization chamber for a single CT slice acquisition, the above equation can be simplified to:

$$\mathrm{CTDI}_{100} = (f * \mathrm{CF} * \mathrm{E} * \mathrm{L})/(\mathrm{N} * \mathrm{T}), \tag{C.2}$$

where:

f = conversion factor (from exposure to dose in air, use 8.7 mGy/R)

CF = calibration or correction factor for electrometer

E = average measured value (exposure or air kerma)

L = active length of pencil ion chamber (typically 100 mm)

N = actual number of data channels used during one axial acquisition

T = width of each channel (Note that N × T = nominal radiation beam width)

Because dose uniformity decreases with increasing object size, a weighted CTDI measurement is derived from CTDI_{100} measurements taken at the center and periphery of an acrylic phantom in order to provide a better estimate of the average dose deposited in a nominal slice thickness for a specific scan-technique. The equations

are:

$$\mathrm{CTDI}_{weighted} = \frac{2}{3}\mathrm{CTDI}_{\mathrm{periphery}} + \frac{1}{3}\mathrm{CTDI}_{\mathrm{center}}, \tag{C.3}$$

$$\mathrm{CTDI}_{vol} = \frac{1}{\mathrm{pitch}}\mathrm{CTDI}_{\mathrm{weighted}}, \tag{C.4}$$

where pitch = 1 for axial acquisitions, and CTDI_{vol} is a single CT dose parameter that represents the average dose within the scan volume for a standardized acrylic CTDI phantom. The American College of Radiology (ACR) recommends that $\mathrm{CTDI}_{\mathrm{vol}}$ for head techniques, which are measured using a 16 cm diameter phantom, be less than 80 mGy.

REFERENCES

[1] M. D. Abramoff. Image processing with imagej. *Biophotonics International*, 11(7):36–42, 2004.

[2] D. L. Batchelar, M. T. M. Davidson, W. Dabrowski, and I. A. Cunningham. Bone-composition imaging using coherent-scatter computed tomography: Assessing bone health beyond bone mineral density. *Med. Phys.*, 33(4):904–915, 2006.

[3] P. R. Bevington and D. K. Robinson. *Data Reduction and Error Analysis for the Physical Sciences*. McGraw-Hill, 2003.

[4] J. M. Boone, T. R. Fewell, and R. J. Jennings. Molybdenum, rhodium, and tungsten anode spectral models using interpolating polynomials with application to mammography. *Med. Phys.*, 24(12):1863–1874, 1997.

[5] J. M. Boone and J. A. Seibert. An accrate method for computer-generating tungsten anode x-ray spectra from 30 to 140 kv. *Med. Phys.*, 24(11):1661–1670, 1997.

[6] J. T. Bushberg, J. A. Seibert, E. M. Leidholdt, and J. M. Boone. *The Essential Physics of Medical Imaging*. Lippincott Williams & Wilkins, second edition, 2002.

[7] H. Chan and K. Doi. Physical characteristics of scattered radiation in diagnostic radiology: Monte carlo simulation studies. *Med. Phys.*, 12(2):152–165, 1985.

[8] S. R. Cherry, J. A. Sorenson, and M. E. Phelps. *Physics in Nuclear Medicine*. Saunders, 2003.

[9] M. T. M. Davidson, D. L. Batchelar, B. H. Chew, J. D. Denstedt, and I. A. Cunningham. Establishing composition and structure of intact urinary calculi by x-ray coherent scatter for clinical laboratory investigations. *J. Urology*, 175:2336–2340, 2006.

[10] S. D. de Magãlhaes, O. D. Gonçalves, and P. Rizzo. Scattering of 60 kev photons by biological material and influence in diagnostic radiology. *Med. Phys.*, 23(9):1635–1642, 1996.

[11] S. H. Evans, D. A. Bradley, D. R. Dance, J. E. bateman, and C. H. Jones. Measurements of small-angle photon scattering fom some breast tissues and tissue substitute materials. *Phys. Med. Biol.*, 36(1):7–18, 1991.

[12] M. Fernández, J. Keyriläinen, R. Serimaa, M. Torkkeli, M-L Karjalainen-Lindsberg, M. Tenhunen, W. Thomlinson, V. Urban, and P. Suortti. Small-angle x-ray scattering studies of human breast tissue samples. *Phys. Med. Biol.*, 47:577–592, 2002.

[13] J. D. Gibbons. *Nonparametric Statistical Inference*. Chapman and Hall/CRC, fifth edition, 2011.

[14] A. Guinier. *X-Ray Diffraction In Crystals, Imperfect Crystals, and Amorphous Bodies*. Dover Publications, INC., dover edition edition, 1994.

[15] G. Harding. X-ray scatter tomography for explosive detection. *Rad. Phys. Chem.*, 71:869–881, 2004.

[16] G. Harding, J. Kosanetzky, and U. Neitzel. X-ray diffraction computed tomography. *Med. Phys.*, 14(4):515–525, 1987.

[17] G. Harding and B. Schreiber. Coherent x-ray scatter imaging and its application in biomedical science and industry. *Rad. Phys. Chem.*, 56:229–245, 1999.

[18] H. Hirayama, Y. Namito, A. F. Bielajew, S. J. Wilderman, and W. R. Nelson. *The EGS5 Code System*. Stanford Linear Accelerator Center, Menlo Park, CA, 14 January 2009. Reference is classified under two different report numbers: SLAC Report number: SLAC-R-730; Japan High Energy Accelerator Research Organization (KEK) Report number: 2005-8.

[19] Alexey N. Hopersky and Victor A. Yavana. *Scattering of Photons by Many-Electron Systems*. Number 58 in Atomic, Optical, and Plasma Physics. Springer, 2010.

[20] Jiang Hsieh. *Computed Tomography: Principles, Design, Artifacts, and Recent Advances*. SPIE Publications, 2003.

[21] J. H. Hubbell and I. Øverbø. Relativistic atomic form factors and photon coherent scattering cross sections. *J. Phys. Chem. Ref. Data*, 8:69–105, 1979.

[22] P. C. Johns and M. P. Wismayer. Measurement of coherent x-ray scatter form factors for amorphous materials using diffractometers. *Phys. Med. Biol.*, 49:5233–5250, 2004.

[23] P. C. Johns and M. J. Yaffe. Coherent scatter in diagnostic radiology. *Med. Phys.*, 10(1):40–50, 1983.

[24] G. Kidane, R. D. Speller, G. J. Royle, and A. M. Hanby. X-ray scatter signatures for normal and neoplastic breast tissues. *Phys. Med. Biol.*, 44:1791–1802, 1999.

[25] B. W. King and P. C. Johns. An energy-dispersive technique to measure x-ray coherent scattering form factors of amorphous materials. *Phys. Med. Biol.*, 55:855–871, 2010.

[26] B. W. King, K. A. Landheer, and P. C. Johns. X-ray coherent scattering form factors of tissues, water and plastics using energy dispersion. *Phys. Med. Biol.*, 56:4377–4397, 2011.

[27] L. Kissel, R. H. Pratt, and S. C. Roy. Rayleigh scattering by neutral atoms, 100 ev to 10 mev. *Physical Review A*, 22(5):1970–2003, 1980.

[28] U. Kleuker, P. Suortti, W. Weyrich, and P. Spanne. Feasibility study of x-ray diffraction computed tomography for medical imaging. *Phys. Med. Biol.*, 43:2911–2923, 1998.

[29] J. Kosanetzky, B. Knoerr, G. Harding, and U. Neitzel. X-ray diffraction measurements of some plastic materials and body tissues. *Med. Phys.*, 14(4):526–532, 1987.

[30] R. J. Leclair and P. C. Johns. X-ray forward-scatter imaging: Experimental validation of model. *Med. Phys.*, 28(2):210–219, 2001.

[31] C. J. Leliveld, J. G. Maas, V. R. Bom, and C. W. E. van Eijk. Monte carlo modeling of coherent scattering: Influence of interference. *IEEE Transactions on Nuclear Science*, 43(6):3315–3321, 1996.

[32] C. J. Leliveld, J. G. Maas, C. W. E. van Eijk, and V. R. Bom. On the significance of scattered radiation in industrial x-ray comperterized tomographic imaging. *IEEE Transactions on Nuclear Science*, 41(1):290–294, 1994.

[33] K. Lewis, E. Donnelly, D. Pickens, and R. Price. Web201b05: Monte carlo simulation of coherent scatter computed tomography (csct). *Med. Phys.*, 37(6):3417, 2010. http://dx.doi.org/10.1118/1.3469353.

[34] MATLAB. *version 8.1.0.604 (R2013a).* The MathWorks Inc., Natick, Massachusetts, 2013.

[35] C. McCollough, D. Cody, S. Edyvean, R. Giese, B. Gould, N. Keat, W. Huda, P. Judy, W. Kalender, M. McNitt-Gray, R. Morin, T. Payne, S. Stern, L. Rothengerg P. Shrimpton, J. Timmer, and C. Wilson. *The Measurement, Reporting, and Management of radiation Dose in CT.* American Association of Physicists in Medicine, 2007.

[36] M. F. McNitt-Gray. Aapm/rsna physics tutorial for residents: Topics in ct, radiation dose in ct. *RadioGraphics*, 22(6):1541–1553, 2002.

[37] L.R.M. Morin. Molecular form factors and photon coherent scattering cross sections of water. *J. Phys. Chem. Ref. Data*, 11(1):1091–1098, 1982.

[38] B. Mueller, M. K. O'Connor, I. Blevis, D. J. Rhodes, R. Smith, D. A. Collins, and S. W. Phillips. Evaluation of a small cadmium zinc telluride detector for scintimammography. *The Jounrnal of Nuclear Medicine*, 44(4):602–609, 2003.

[39] Y. Namito, H. Hirayama, A.F. Bielajew, S.J. Wilderman, and W. R. Nelson. Outline of egs5. The Japan Taiwan Symposium on Simulation in Medicine (13 Dec 2006, Tsukuba).

[40] M. Nikl. Scintillation detectors for x-rays. *Meas. Sci. Technol.*, 17:R37–R54, 2006.

[41] J. N. O'Dwyer and J. R. Tickner. Modelling diffractive x-ray scattering using the egs monte carlo code. *Nucl. Instrum. Methods in Phys. Research, Sect. A*, 580:127–129, 2007.

[42] D. E. Peplow and K. Verghese. Measured molecular coherent scattering form factors of animal tissues, plastics and human breast tissue. *Phys. Med. Biol.*, 43:2431–2452, 1998.

[43] E. B. Podgoršak. *Radiation Physics for Medical Physicists*. Springer, New York, first edition, 2010.

[44] M. E. Poletti, O. D. Gonçalves, and I. Mazzaro. X-ray scattering from human breast tissues and breast-equivalent materials. *Phys. Med. Biol.*, 47:47–63, 2002.

[45] W. S. Rasband. Imagej, 1997-2012.

[46] A. R. Round, S. J. Wilkinson, C. J. Hall, K. D. Rogers, O. Glatter, T. Wess, and I. O. Ellis. A preliminary study of breast cancer diagnosis using laboratory based small angle x-ray scattering. *Phys. Med. Biol.*, 50:4159–4168, 2005.

[47] G. J. Royle and R. D. Speller. Low angle x-ray scattering for bone analysis. *Phys. Med. Biol.*, 36(3):383–389, 1991.

[48] RTI Electronics. Barracuda and mpd. http://www.rti.se/products/barracuda/.

[49] E. A. Ryan and M. J. Farquharson. Breast tissue classification using x-ray scattering measurements and multivariate data analysis. *Phys. Med. Biol.*, 52:6679–6696, 2007.

[50] J. P. Schlomka, J. Delfs, H. Barschdorf, A. Thran, and U. Stevendall. Experimental feasibility study of energy-resolved fan-beam coherent scatter computed tomography. *Proc. of SPIE*, 5535:410–423, 2004.

[51] J. P. Schlomka, S. M. Schneider, and G. Harding. Novel concept for coherent scatter x-ray computed tomography in medical applications. *Proc. of SPIE*, 4142:218–224, 2000.

[52] S. M. Schneider, J. P. Schlomka, and G. Harding. Coherent scatter computed tomography applying a fan-beam geometry. *Proc. of SPIE*, 4210:754–763, 2001.

[53] L. Sobotka and W. Reviol. Oak ridge presentation: Cadmium zinc telluride (czt) detectors, March 2003.

[54] R. D. Speller and J. A. Horrocks. Photon scattering - a 'new' source of information in medicine and biology? *Phys. Med. Biol.*, 36(1):1–6, 1991.

[55] U. Stevendall, J. P. Schlomka, A. Harding, and M. Grass. A reconstruction algorithm for coherent scatter computed tomography based on filtered back-projection. *Med. Phys.*, 30(9):2465–2474, 2003.

[56] E. Storm and H. I. Israel. Photon cross sections from 1 kev to 100 mev for elements z=1 to z=100. *Nucl. Data Tables A*, 7:565–681, 1970.

[57] A. Tartari, E. Casnati, C. Bonifazzi, and C. Baraldi. Molecular differential cross sections for x-ray coherent scattering in fat and polymethyl methacrylate. *Phys. Med. Biol.*, 42:2551–2560, 1997.

[58] A. Tartari, A. Taibi, C. Bonifazzi, and C. Baraldi. Updating of form factors tabulations for coherent scattering of photons in tissues. *Phys. Med. Biol.*, 47:163–175, 2002.

[59] C. Theodorakou and M. J. Farquaharson. Human soft tissue analysis using x-ray or gamma-ray techniques. *Phys. Med. Biol.*, 53:R111–R149, 2008.

[60] M. S. Westmore, A. Fenster, and I. A. Cunningham. Angular-dependent coherent scatter measured with a diagnostic x-ray image intensifier-based imaging system. *Med. Phys.*, 23(5):723–733, 1996.

[61] M. S. Westmore, A. Fenster, and I. A. Cunningham. Tomographic imaging of the angular-dependent coherent-scatter cross section. *Med. Phys.*, 24(1):3–10, 1997.

[62] M. B. Wilk. Probability plotting methods for the analysis of data. *Biometrika*, 55(1):1–17, 1968.